Ceria-Based Catalysts Studied by Near Ambient Pressure X-ray Photoelectron Spectroscopy: A Review

Xènia Garcia [1,2] , **Lluís Soler** [1] , **Núria J. Divins** [1] , **Xavier Vendrell** [1] , **Isabel Serrano** [1] , **Ilaria Lucentini** [1] , **Jordi Prat** [2] , **Eduardo Solano** [2] , **Massimo Tallarida** [2] , **Carlos Escudero** [2,*] and **Jordi Llorca** [1,*]

[1] Institute of Energy Technologies, Department of Chemical Engineering and Barcelona Research Center in Multiscale Science and Engineering, Universitat Politècnica de Catalunya, Escola d'Enginyeria de Barcelona Est (EEBE), Eduard Maristany 10-14, 08019 Barcelona, Spain; xenia.garcia.de.andres@upc.edu (X.G.); lluis.soler.turu@upc.edu (L.S.); nuria.jimenez.divins@upc.edu (N.J.D.); xavier.vendrell.villafruela@upc.edu (X.V.); isabel.serrano@upc.edu (I.S.); ilaria.lucentini@upc.edu (I.L.)

[2] ALBA Synchrotron Light Source, Carrer de la Llum 2-26, Cerdanyola del Vallès, 08290 Barcelona, Spain; jprat@cells.es (J.P.); esolano@cells.es (E.S.); mtallarida@cells.es (M.T.)

* Correspondence: cescudero@cells.es (C.E.); jordi.llorca@upc.edu (J.L.); Tel.: +34935924372 (C.E.); +34934011708 (J.L.)

Abstract: The development of better catalysts is a passionate topic at the forefront of modern science, where *operando* techniques are necessary to identify the nature of the active sites. The surface of a solid catalyst is dynamic and dependent on the reaction environment and, therefore, the catalytic active sites may only be formed under specific reaction conditions and may not be stable either in air or under high vacuum conditions. The identification of the active sites and the understanding of their behaviour are essential information towards a rational catalyst design. One of the most powerful *operando* techniques for the study of active sites is near ambient pressure X-ray photoelectron spectroscopy (NAP-XPS), which is particularly sensitive to the surface and sub-surface of solids. Here we review the use of NAP-XPS for the study of ceria-based catalysts, widely used in a large number of industrial processes due to their excellent oxygen storage capacity and well-established redox properties.

Keywords: ceria; catalysis; X-ray photoelectron spectroscopy; photoemission; NAP-XPS; AP-XPS; APPES

1. Ceria in Catalysis

Ceria-based catalysts have been widely investigated in the last decades for different applications. They include nanoshaped ceria, ceria mixed metal oxides and transition metals supported on ceria. In addition to its well-established use as an active component of catalytic converters for the treatment of exhaust gases, ceria-based catalysts have also been developed for soot abatement, VOC combustion, reforming processes, water-gas shift, methane activation, acid-base chemistry and organic chemistry reactions, among others. An excellent level of fundamental knowledge has been attained over the years, which has been compiled in a large number of seminal reviews [1–6].

Ceria displays an extraordinary oxygen storage capacity (OSC) and redox properties because it has the ability to accommodate a large number of oxygen vacancies under a slightly reducing atmosphere to give under-stoichiometric CeO_{2-x}, which can be oxidised back to CeO_2 in an oxygen-containing atmosphere. This occurs without structural modification of the fluorite ceria lattice and is not limited to the surface, but also takes place in the bulk [7,8]. Surface science studies on thin layers of ceria with controlled terminations and studies performed on nanoshaped ceria (rods, cubes, wires, tubes and spheres)

demonstrate that the formation of an oxygen vacancy on ceria is strongly surface sensitive and that the redox reactivity of ceria depends on the crystallographic planes exposed [9–12]. The {111} is the thermodynamically most stable termination, followed by the {110} and the least stable {100} [13,14]. However, surface reconstruction, surface roughening and creation of defects commonly occur to lower the surface energy [15]. Vacancies play an active role in the oxygen storage process and represent mobile reactive sites which can act as centres for oxygen activation in oxidation reactions [16]. The {111} surface is the most compact and less prone to accommodate a vacancy defect and the order of reactivity for the vacancy formation follows the trend {110} > {100} > {111} [17]. The precise control of surface atomic arrangements in ceria can modify the reactivity of Ce^{4+}/Ce^{3+} ions and change the oxygen release/uptake characteristics, which, in turn, are closely tied with its catalytic properties [18]. In particular, oxidation reactions over CeO_2 are believed to proceed through the Mars-van Krevelen mechanism, where the reactant first reacts with surface ceria oxygen leaving an oxygen vacancy, which is then filled with gas phase oxygen.

In addition to the importance of the exposed planes, the other key parameter that modifies the surface chemistry of ceria is particle size. The smaller the ceria particle size the larger the reduction of the valence of Ce from +4 to +3, which implies a correlation between oxygen vacancy concentration and ceria crystal size. This is particularly evident in ceria crystallites below 5 nm [19–22]. In this case, Ce^{3+} sites are not necessarily associated to an oxygen vacancy and can act as a centre for adsorption of oxygen to yield active oxygen species and thus boosting oxygen storage activity and low-temperature oxidation activity [23–26]. There is a consensus that the preparation of active ceria-based catalysts requires the presence of defective surface sites, either Ce^{3+} or Ce^{4+} associated with a vacancy, which can act as centres to maximize active oxygen adsorption/release under operative conditions. Nevertheless, the way to accomplish this and the associated mechanism is not yet completely known. For instance, the structure of these defects plays also an important role in catalysis, being larger oxygen vacancy clusters preferable [27,28].

Regarding the role of ceria as a support, it is remarkable how it can strongly modify the reactivity of supported metal nanoparticles [29–31] and also protect metal nanoparticles from sintering at high temperature [32], or even stabilize metals as single atoms [33]. The unique properties of ceria, such as the availability of surface oxygen species which ceria can supply to those metal atoms located at the interface perimeter [34,35], makes it an excellent support for a wide number of catalytic applications [36]. From the study of inverse structures, where ceria nanoparticles are deposited on selected metal films, the metal-CeO_2 interface has unambiguously been identified as the catalytic active site in many reactions [37]. The mechanism of oxygen transfer between ceria and the metal is responsible for the enhancement of activity and, again, it is strongly dependent on the morphology and the size of the ceria particles [38–40]. The surface terminations of CeO_2 can also influence the size, morphology and interface of the metal nanoparticles that, furthermore, can change under different reaction environments. These factors are interdependent and originate complex systems. As expected, the electronic state of the deposited metal nanoparticles strongly depends on the reduction degree of the ceria support and, in particular, by the presence of oxygen vacancies in areas underneath the metal [41,42]. Interestingly, the presence of metal nanoparticles on top of ceria crystallites in turn strongly modifies the reducibility of the underlying cerium oxide. Obviously, this synergy has an impact on the catalytic behaviour and the use of *operando* characterization techniques turns out to be invaluable and necessary to decipher the nature of the metal–ceria interface, which remains a controversial issue in most cases.

In this review, we focus on the use of near ambient pressure X-ray photoelectron spectroscopy (NAP-XPS) to study the surface and subsurface arrangements in ceria-based catalysts. In addition, their dynamic behaviour under operation conditions to ultimately obtain structure-activity relationships will also be revised.

2. Near Ambient Pressure XPS

X-ray photoelectron spectroscopy (XPS) has been widely used in heterogeneous catalysis as one of the most powerful techniques to yield information on the chemical composition and electronic

configuration of the different elements present on the surface of the materials studied. This tool, developed in the late 1950s by K. Siegbahn and co-workers [43,44], had a great impact on surface science and other related scientific fields and allowed K. Siegbahn to win the Nobel Prize in Physics in 1981. In heterogeneous catalysis, the surface of the catalysts is in direct contact with the reactants, gases or liquids. Therefore, the potential of XPS is obvious, as a surface-sensitive technique with a probing depth that can be tuned, depending on the excitation energy used, down to a few atomic layers. However, XPS has been traditionally performed under high vacuum or ultra-high vacuum environments due to the strong interaction of the photoelectrons ejected with liquid and gas phase molecules. In this way, many instruments working under this pressure regime using conventional x-ray sources or synchrotron light can be found in many laboratories and synchrotrons around the world and XPS has become a routine analysis technique in many laboratories and industries. Since this pressure regime is far from the one applied in heterogeneous catalytic reactions, the catalyst characterization by XPS is usually done before and after its exposure to the reaction conditions in a high-pressure cell. Nevertheless, it has been demonstrated that in some cases the catalysts exhibit dramatic differences when exposed to the reaction environment. This fact explains the many efforts made to minimize the so-called pressure gap in different spectroscopic techniques [45–47]. Indeed, K. Siegbahn was pioneering also the XPS operation under more realistic environments and, by the implementation of a differential pumping system, he was able to acquire the first gas phase spectra [48]. Furthermore, together with his son, H. Siegbahn, they started to apply the XPS technique to study liquids [49]. During the next decades, there were several improvements to overcome the constraints to use XPS under higher gas pressures [50] but the implementation of an electrostatic lens system that focused the photoelectrons in the apertures of the differential pumping system [51] was the key that led to the establishment of the ambient pressure photoelectron spectroscopy (APPES) technique, also called ambient pressure or near ambient pressure X-ray photoelectron spectroscopy (AP-XPS or NAP-XPS). In the beginning, the NAP-XPS technique was found only in synchrotron facilities [52] (e.g., ALS, BESSY) but during the last two decades it has become a commercially available technique and lab-based instruments with different configurations are also spreading worldwide [53].

The application of NAP-XPS in heterogeneous catalysis has opened new possibilities and a large number of reviews and book chapters have appeared in the last years [50,52–65]. NAP-XPS has been used within this field to study from single crystals and model metal-oxide systems [35,55,58,60,66] to more realistic mono- and bimetallic unsupported nanocatalysts and metal-oxide complex systems [57]. For the particular case of bimetallic catalysts, the combination of NAP-XPS with synchrotron radiation allows following the segregation of the different metals under reaction conditions [67], i.e., the excitation energy can be tuned and therefore it is possible to detect photoelectrons ejected from different depths of the sample without destroying it. Furthermore, this technique has clarified that these changes on the metals distribution in bimetallic particles not only depend on the reaction environment, but also on the oxide support [68] and even its shape [69]. NAP-XPS, due to its capabilities, is one of the most demanded tools for heterogeneous catalytic studies; however, there are of course other issues to be considered when applying this technique, e.g., beam damage or contamination issues among others. The first one can be assessed to some extent by minimizing the sample exposure to the X-rays (by moving to fresh sample spot, decreasing the acquisition time or decreasing in another way the photon flux) and the second one constitutes one of the main drawbacks related to this powerful tool and sometimes requires the use of plasma cleaning procedures.

On the other hand, the potential of NAP-XPS to study electrocatalytic systems under *operando* conditions has experienced a big step in the last few years with the development of new instrumentation for both solid–liquid and solid–gas interfaces [70–74]. Indeed, the first experiments related to solid-oxide fuel cells (SOFC) studied by means of NAP-XPS were performed on ceria based systems [75].

As stated before, the applications and potential of the NAP-XPS technique have increased substantially in the last years and, as a consequence, the number of related publications has evolved exponentially, including different reviews. However, in this particular case and for the first time,

all the literature related to heterogeneous catalysis and electrocatalysis research focused on ceria-based systems and studied by means of NAP-XPS has been summarized up-to-date. This contribution aims to be a reference to guide future studies in these fields using this powerful technique for a better understanding of the properties of ceria, which will allow designing better catalysts.

3. Examples for the Application of NAP-XPS to Ceria Catalysts

As explained above, the application of NAP-XPS in catalysis science has recently received great interest since it allows the study of real and model catalytic systems, as well as electrochemical devices, during the reaction. This surface-sensitive technique can provide information on catalysts' chemical state and surface composition under a wide range of environmental conditions, including reactant and product gas phase molecules in the vicinity of the surface. Additionally, depth profiling studies are viable by tuning the photon energy in synchrotron sources, which can be used to examine migration of species into the catalyst surface/subsurface and to relate them with changes on reactivity.

In this review, we have gathered to the best of our knowledge all the peer-reviewed reports on cerium oxide performed using the NAP-XPS technique. All the examples included, performed under a wide range of experimental conditions (e.g., temperature, pressure, gas composition, electrical bias), are studies of gas-solid interfaces and have been classified into three well distinctive blocks: a first block of reports based on studies of the properties of cerium oxide itself, a second block which includes all the investigations of ceria-based catalysts for gas-solid reactions and a third and last block of studies of gas-solid electrocatalytic reactions, most of them based on solid oxide fuel cell systems with ceria as a component.

3.1. Fundamental Studies

As discussed in the introduction, one of the properties that makes cerium oxide such an excellent catalyst is its well-known OSC [36,76]. Therefore, in order to improve the activity of ceria-based catalysts, many scientific studies seek the maximization of surface oxygen vacancies on ceria catalysts by optimizing their design, as oxygen vacancies are generally known to be the active sites in multiple catalytic reactions. These investigations include exhaustive studies focused on the alteration of ceria redox properties with particle size, morphology and metal doping, as well as studies of surface oxygen mobility, oxygen storage capacity and the strong metal–support interaction (SMSI) effect. With this aim, ceria-based samples have been mainly studied under reducing (H_2) and oxidising (O_2) atmospheres and high temperatures, although the CO oxidation reaction has often been used as a probe reaction to evaluate redox properties as well.

The SMSI effect strongly alters the physicochemical properties of metal particles dispersed over reducible oxides after exposure to high-temperature reduction treatments. It has been found that the SMSI effect completely inhibits H_2 and CO chemisorption capacity and, consequently, modifies adsorption and catalytic properties of metal/oxide systems [77]. Due to the unique redox behaviour of ceria, the SMSI effect occurs on ceria-supported metal catalysts when they are subjected to a reduction treatment, as several reports already demonstrated [78,79]. However, since the OSC of CeO_{2-x} (0 < x < 0.5) strongly depends on the temperature and oxygen pressure [80], the use of *operando* measurements is decisive to completely understand this effect. Several groups studied such phenomenon with the NAP-XPS technique. This is the case of Caballero et al., who demonstrated the appearance of the SMSI effect after exposing a Ni/CeO_2 system to a reduction treatment at 1.3 mbar of H_2 pressure at 773 K [81]. The catalyst of the study consisted on nickel nanoparticles deposited on a cerium oxide thin film using the Langmuir-Blodgett (LB) method. The huge decrease of the Ni 3p XPS signal during the reduction treatment (which was accompanied by CeO_{2-x} reduction) constituted a proof of the geometrical factor of the SMSI effect, which can be described as the migration of the support covering the metallic nanoparticles and thus blocking catalytic active sites. Nevertheless, this migration was reversible by removing the H_2 gas phase at the same temperature, suggesting that the ceria phase preferentially migrated onto the Ni nanoparticles so as to absorb H_2 through the formation of hydride-like species. Similar results were obtained by

Bernardi et al., who exposed $Rh_{0.5}Pd_{0.5}/CeO_2$ to consecutive processes of reduction and oxidation at different temperatures [82]. They observed not only the geometrical factor of the SMSI effect at 753 K during the reduction treatment at 0.13 mbar H_2 pressure, that is, the coverage of bimetallic nanoparticles with a thin CeO_{2-x} capping layer, but they also identified it as the cause of a change of the atomic Rh/Pd surface segregation behaviour, which led to nanoparticles with a Pd-rich surface configuration. Therefore, besides the described influence of the SMSI effect on the catalytic properties, the SMSI effect on ceria-based systems may also affect the atomic arrangement of bimetallic nanoparticles [68]. Another attempt to elucidate the nature of the SMSI effect was recently made by Figueiredo and co-workers through the study of Cu_xNi_{1-x}/CeO_2 catalysts with different Cu/Ni concentrations [83]. The samples were exposed to a reduction treatment at 773 K in a H_2 atmosphere followed by an oxidation treatment with CO_2 at the same temperature. The SMSI effect was only observed on those catalysts with high concentration of Cu, and it was reversed upon oxidation with CO_2. As a consequence of the SMSI effect, the reduction of Cu atoms of these nanoparticles occurs at lower temperatures than similar nanoparticles that do not display such effect. Finally, Carrasco et al. also reported the significance of the SMSI effect with the investigation of water adsorption on bare $CeO_2(111)$ and on a $Ni/CeO_2(111)$ surface with a small coverage of Ni ($\Theta_{Ni} \sim 0.15$ ML, monolayer) [84]. Water dissociation is a critical step in many catalytic reactions over oxide-supported transition-metal catalysts. By combining ambient pressure XPS and density-functional theory (DFT) studies, researchers found a substantially larger amount of $-$OH groups adsorbed on the Ni-loaded-ceria surface than on the bare support. Water adsorption was not observed under ultra-high vacuum (UHV) conditions ($p_{H_2O} < 10^{-7}$ mbar), but adsorption occurred under water pressures above 10^{-3} mbar (0.13 and 0.26 mbar) at 300 K, and part of the chemisorbed water molecules dissociated to generate hydroxyl groups on the surface. Adsorbed water and consequently $-$OH groups disappeared upon heating the systems at 500 and 700 K under 0.26 mbar background pressure. Therefore, the type and amount of species adsorbed on both systems were strongly affected by the water pressure and the temperature of the surfaces. The rapid water dissociation on Ni/CeO_2 catalyst has a severe effect on the activity and stability of this system for the water-gas shift and steam reforming of ethanol reactions, since $-$OH groups can easily react with CO and CH_x groups to produce CO_2 and H_2.

It is commonly accepted that the incorporation of a metallic active phase on a cerium oxide support alters its redox properties and, consequently, its catalytic activity. Therefore, ceria is usually combined with noble metals, such as Ru [85], Pt [30,86,87], Pd [86–88], Rh [86,87] and Au [89–94] or with first-row non-noble transition metals, such as Fe [88], Co [88,95], Cu [96,97] or Ni [88,98], among others. A great deal of investigations about these systems is at present available due to its importance as a component of three-way catalysts (TWCs) exhaust gas purification systems, but only a few of them have been investigated by means of NAP-XPS. In 2013, Alayoglu et al. demonstrated the reversible reduction of mesoporous CeO_2 under H_2 atmospheres mediated by platinum nanoparticles using NAP-XPS [99]. The measurements, performed under 0.13 mbar of H_2, revealed that cerium oxide was reduced at lower temperatures for Pt/CeO_2 catalyst than for pure mesoporous CeO_2. This phenomenon was attributed to the spillover of atomic hydrogen from Pt to ceria surface: platinum nanoparticles dissociate H_2 to H, which spills onto CeO_2 at the gas-solid interface and reduces the oxide through the formation of OH^- or oxygen vacancies. Particularly, in hydrogen environments, Pt decreases the activation barrier for ceria reduction. These results were verified by near-edge X-ray absorption fine structure (NEXAFS) and combined with X-ray diffraction (XRD) and extended X-ray absorption fine structure (EXAFS) measurements, which showed a reversible expansion and contraction of the CeO_2 unit cell under H_2 and O_2 atmospheres, respectively, in accordance to the size of Ce^{3+} and Ce^{4+}. Similar results were presented by Kato and co-workers [100], who also studied the reduction behaviour of nanostructured ceria-supported Pt catalyst, specifically platinum nanoparticles deposited on ceria nanocubes. They obtained a depth profile of the cerium oxidation state in the CeO_2 nanocubes as a function of the gas environment and the loaded metal. To achieve so, NAP-XPS analyses were performed in a synchrotron by varying the energy of the X-rays and, thus, the probing depth. Under an atmosphere of 1 mbar H_2 at 403 K, oxygen vacancies were created only in the uppermost layers of

the ceria nanocubes impregnated with Pt. The study of Sohn et al. was also focused on the surface oxygen mobility and oxygen vacancy formation of ceria nanoparticles, in this case depending on the particle dimensions as well as on the presence of an active metallic phase [101]. Nevertheless, ethanol steam reforming reaction conditions were used for their study instead of H_2. Briefly, oxidation states of small ceria nanoparticles (NPs, ~ 4 nm) and larger particles (MPs, ~ 120 nm) were compared to those of cobalt-loaded NPs and MPs during a reductive pre-treatment at 673 K under 0.26 mbar H_2 and the successive ethanol steam reforming under 0.13 mbar of ethanol and 1.3 mbar of water at 623, 673 and 723 K. Although both bare ceria NPs and MPs supports were active for the ethanol steam reforming, Co/CeO_2-NP was found to be the most active one and the one with the highest extent of reduced CeO_2.

A well-known method to notably enhance cerium oxide redox activity is the addition of 3d transition metals to its unit cell to form solid solutions with an ordered atomic arrangement [3,102]. For instance, it has been demonstrated that $Ce_{1-x}M_xO_{2-y}$ mixed oxides (where M = Cr [103,104], Mn [104–106], Fe [104,106], Co [104–106], Ni [105,106], Cu [107,108], Zr [109–111], La [112–114]) exhibit lower reduction temperatures than pure ceria. The incorporation of noble metals to ceria to generate $Ce_{1-x}M'_xO_{2-y}$ mixed oxides (M' = Ru [115], Rh [116,117], Pd [117,118]) has also demonstrated to efficiently promote reducibility of cerium ions and greatly decrease the reduction temperatures too [119]. Ikemoto et al. investigated the reversible redox activity of $Cr_{0.19}Rh_{0.06}CeO_x$ by means of NAP-XPS, while its catalytic properties were tested with CO and 1-octanol oxidation reactions [120]. NAP-XPS measurements were performed under an atmosphere of 1.3 mbar H_2, heating the sample from room temperature to 385 K and then cooling it again. Reduction was followed by an oxidation treatment at 573 K under 2 mbar O_2. Combined with in situ XAFS analysis, the results revealed the transformation of dispersed $Rh^{\delta+}$ species and small CrO_x nanoparticles supported on CeO_2 to Rh nanoclusters, $Cr(OH)_3$ species and CeO_{2-x} when treated with H_2. Thus, they demonstrated a remarkable and reversible low-temperature redox activity of $Cr_{0.19}Rh_{0.06}CeO_x$ due to the combined contribution of the three metal species, which do not reduce below 373 K when they exist separately.

Della Mea et al. studied the redox properties of differently prepared ceria nanoparticles exposed to 1 mbar CO reducing atmosphere and high temperature [121]. Their aim was to tune the oxygen vacancy population in order to design a rational and optimal ceria catalyst for CO oxidation. More than ten different CeO_2 nanoparticle types were prepared by modifying synthesis parameters and two of them were studied with NAP-XPS, as well as standard CeO_2. They found that small size, high initial Ce^{3+} content, high surface area and low pore volume decreased the ceria reduction temperature. Similar investigations were performed by Pereira-Hernández and co-workers [122], who compared the low-temperature (< 423 K) CO oxidation performance of Pt/CeO_2-based catalysts prepared via conventional wet chemical synthesis (strong electrostatic adsorption) or high-temperature gas phase synthesis (atom trapping). The samples prepared by atom trapping caused Pt to covalently bond with the surface oxygen atoms as well as ceria restructuration. As synthesised, both catalysts were inactive for low-temperature CO oxidation, but their reactivity improved after a treatment under 2 mbar CO at 548 K. The combination of NAP-XPS and CO temperature-programmed reduction (CO-TPR) showed that the catalyst prepared by atom trapping achieved higher activity for CO oxidation after reduction in CO at 548 K, step that led to the partial transformation of Pt single atoms into Pt clusters.

Sayle et al. claimed on the basis of non-equilibrium Molecular Dynamics simulations that the catalytic activity of cerium oxide in the catalytic CO oxidation reaction could be predicted by knowing the oxygen vacancy population at its surface [123]. A catalytic activity map for ceria was presented in their report, calculated as a function of size, shape, architecture and defect content. Their simulations were supported by NAP-XPS analyses of two samples of ceria nanoparticles with different initial surface Ce^{3+}/Ce^{4+} ratios.

Another approach for the study of ceria catalytic properties by NAP-XPS was reported by Gopal et al., who quantified the effect that large biaxial strain generated on ultrathin ceria films had on the surface redox behaviour of CeO_{2-x} [124]. They prepared ultrathin cerium oxide films under biaxial compression on single-crystalline (001) yttria-stabilized zirconia (YSZ) and under biaxial tension on

(001) SrTiO$_3$ $_($STO), taking advantage of the high lattice mismatch between ceria and both substrates, which modifies the interatomic distances of ceria lattice and causes significant changes in its electronic structure and redox capacity. Samples were studied by different characterization techniques, but surface Ce^{3+} and oxygen vacancy concentrations were directly quantified by means of NAP-XPS at 723 and 823 K in both O$_2$ and H$_2$/H$_2$O atmospheres and compared with those of fully relaxed ceria films. The results revealed a significant enhancement of Ce^{3+} and oxygen vacancy concentrations near the surface for both compressive and tensile strained oxide films.

3.2. Gas-Solid Catalysis

Since NAP-XPS was first developed, investigations of gas-solid interfaces have been the frontrunner of the technique due to the many relevant applications they have in the fields of catalysis, corrosion, energy materials and atmospheric science [62,125]. Additionally, the preparation and measurement of gas-solid interfaces with NAP-XPS are relatively simple compared to, e.g., measurements of liquid interfaces. In particular, there has been recently great interest and success in the study of real and model catalytic systems, as well as electrochemical devices, with one or multiple reactant gases. These studies included adsorption, reaction induced restructuring and catalytic performance of systems ranging from highly-ordered single crystals to supported nanoparticles. Therefore, in this second block we have collected and organised all the reports of gas-solid catalytic reactions with ceria-based systems found in the literature, which emphasize the advantages and deficiencies of the NAP-XPS technique in these gas-solid interfaces. Table 1 provides a list of reports of NAP-XPS studies of ceria-based catalysts in the presence of gases published so far, which are described in the following paragraphs.

Table 1. Published near ambient pressure X-ray photoelectron spectroscopy (NAP-XPS) investigations of ceria-based catalysts in gas-solid reactions.

Reaction	Catalyst	P$_{max}$ (mbar)	T (K)	X-ray Source	Year	Ref.
CO oxidation and preferential CO oxidation (PROX)	5% Pt/CeO$_2$	~ 0.5	358−523	Synchrotron	2006	[126]
	5% Pd/CeO$_2$	~ 0.5	358−523	Synchrotron	2006	[127]
	5% Pt/CeO$_2$	~ 1	393	Synchrotron	2007	[128]
	Au-Ni/CeO$_2$	~ 1	523	Synchrotron	2013	[129]
	1% Cu/CeO$_2$ nanospheres 1% Cu/CeO$_2$ nanocubes	~ 1	300−553	Synchrotron	2015	[130]
	10% CeO$_2$/Co$_3$O$_4$	0.5	300−573	Synchrotron	2016	[131]
	3% Pt/CeO$_2$	1	373	Synchrotron	2017	[132]
	CeO$_2$ nanoparticles	~ 1	373−773	Lab-based	2017	[121]
	1% Pt/CeO$_2$	~ 2	323−373	Lab-based	2019	[122]
Water-gas shift reaction (WGS)	2.5% M@*mesoporous*-CeO$_2$2.5% M/rod-CeO$_2$ (M = Au, Pt, Pd, Cu)	1.95	403−543	Lab-based	2012	[133]
	CeO$_2$/CuO	0.5	473−523	Synchrotron	2012	[134]
	CeO$_x$/Cu(111) CeO$_x$/Au(111)	~ 0.5	300−573	Synchrotron	2013	[39]
Soot oxidation	CeO$_2$ and Ce$_{0.8}$Zr$_{0.2}$O$_2$ nanoparticles	1	300−823	Synchrotron	2016	[135]
CO$_2$ hydrogenation	CeO$_x$/Cu(111)	0.39	473	Synchrotron	2014	[136]
	CeO$_x$/Cu(111)	~ 0.4	300−500	Synchrotron	2016	[137]
	5% Cu/CeO$_2$ nanospheres 5% Cu/CeO$_2$ nanorods	0.06	300−723	Lab-based	2018	[97]
	0.5, 1.5 and 5% Ni/CeO$_2$	~ 0.06	300−623	Lab-based	2019	[138]

Table 1. *Cont.*

Reaction		Catalyst	P_{max} (mbar)	T (K)	X-ray Source	Year	Ref.
Hydrocarbons	Oxidation and partial oxidation	5% M/CeO$_2$ (M = Pd, Pt, Rh)	3.9	300−873	Lab-based	2013	[139]
		Co$_3$O$_4$/CeO$_2$ nanorods	1.56	423−773	Lab-based	2018	[140]
		15% NiO/CeO$_2$ nanorods	1.56	423−773	Lab-based	2018	[141]
	Dry reforming	26% Ni/CeO$_2$	1.3	773−923	Synchrotron	2008	[142]
		Ni/CeO$_2$(111)	0.26	300−700	Synchrotron	2016	[143]
		Ni/CeO$_2$(111)	0.26	700	Synchrotron	2016	[144]
		1.5% Ni, 1.7% Pt and PtNi/CeO$_2$/TiO$_2$(110)	0.39	303−723	Synchrotron	2016	[145]
		M/CeO$_2$(111)/Ru(0001) (M = Co, Ni, Cu)	0.13	300−700	Lab-based	2017	[146]
		10% Co/CeO$_2$	~ 0.2	300−773	Lab-based	2018	[147]
		PtCo/CeO$_2$(Pt = 1.67%, Co = 1.51%)	0.052	823	Lab-based	2018	[148]
		0.5% Ru (NC)/CeO$_2$	0.13	300−773	Lab-based	2019	[149]
Alcohols	Steam reforming (SR)	CeO$_2$(111)/Cu(111) Co/CeO$_2$(111)/Cu(111)	1	320−600	Lab-based	2013	[150]
		3% Rh$_{0.5}$Pd$_{0.5}$/CeO$_2$	0.05	823	Synchrotron	2014	[68]
		8% Co/CeO$_2$	0.2	523−693	Synchrotron	2016	[151]
		23% Co/CeO$_2$	0.3	693	Synchrotron	2016	[152]
		10% Co/CeO$_2$-NP [a] 10% Co/CeO$_2$-MP [b]	1.43	623−723	Lab-based	2016	[153]
		Ni/CeO$_2$(111)/Ru(0001)	~ 0.3	300−700	Synchrotron	2016	[154]
		Co/CeO$_2$-NP Co/CeO$_2$-MP	1.43	623−723	Lab-based	2017	[101]
		Ni/CeO$_2$ Ni/CeO$_{2-x}$/Ru(0001)	2 L *	300−700	Synchrotron	2018	[155]
		3% Rh$_{0.5}$Pd$_{0.5}$/CeO$_2$ nanocubes 3% Rh$_{0.5}$Pd$_{0.5}$/CeO$_2$ nanorods	0.05	823	Synchrotron	2019	[69]
	Oxidation	CeO$_2$(100)/STO(100)	0.39	523−723	Synchrotron	2018	[156]
Hydrogenation reactions		CeO$_2$ nanorods	0.65	533−673	Lab-based	2017	[157]
		CeO$_2$/Pt	0.39	300−473	Lab-based	2017	[158]

[a] NP = nanoparticles; [b] MP = microparticles; * L = Langmuir.

### 3.2.1. CO Oxidation and Preferential CO Oxidation (PROX)

The preferential oxidation of carbon monoxide (PROX) is considered an essential reaction to produce high-pure hydrogen for proton-exchange membrane fuel cells (PEMFCs), which must be CO-free for their proper operation [159]. In fact, the concentration of CO in the hydrogen feed must be kept as low as possible (below 1–100 ppm as a rule) [160]. This can be achieved by using sequential water-gas shift (WGS) and PROX units; the former one reduces the amount of CO to 0.5%−1% [159] and then PROX reaction reduces this concentration to < 100 ppm by selectively oxidising CO, avoiding the oxidation of hydrogen. An appropriate catalyst for PROX reaction should not only adsorb carbon monoxide but also supply activated oxygen, as long as hydrogen adsorption is suppressed. Many catalytic formulations have already been applied for PROX reaction, among them supported noble metals such as Au [161–164], Pt [162,164–167], Rh [165] and Ru [165,168], which are responsible for CO adsorption. However, oxygen does not adsorb on these metals because their surface is fully covered by CO molecules, so different activation sites are required for O$_2$. Here is where cerium oxide becomes important as a component of these catalysts, because of its role as a reducible support for metallic nanoparticles, able to promote oxidation even under oxygen-poor conditions [76]. In order to gain further insight into the reaction mechanism of the PROX reaction on ceria-based catalysts, several research groups examined changes in the oxidation state of ceria and the supported metal, as well as the surface adsorbed species, under PROX conditions by means of the NAP-XPS technique. Pozdnyakova et al. examined the Pt/ceria [126] and Pd/ceria [127] catalytic systems in separate papers using the same techniques, so as to obtain a better understanding of the PROX reaction mechanism when comparing

both systems, although it is well-known that palladium is far less active in this reaction. Both systems were performed with 5 wt % metal loading and studied under approximately 0.5 mbar PROX mixture ($CO + O_2 + H_2$) after being first activated in an oxygen environment (0.5 mbar, 573 K), but also were studied under a CO and O_2 mixture, pumping the hydrogen pressure out of the analysis chamber. The combination of in situ diffuse reflectance infrared Fourier transform spectroscopy (DRIFTS), which aided the identification of surface species, and NAP-XPS allowed the clarification of the main question of the work: why both Pt and Pd catalysts are active in CO oxidation but Pd is not active and selective in the presence of H_2 (PROX reaction). Researchers concluded that at PROX conditions and low temperatures (T = 350−380 K) CO oxidation was suppressed due to the easy formation of Pd β-hydride, identified by NAP-XPS. Adsorbed H rapidly reacted with oxygen from both gas-phase and support sites (also from PdO_x phase) and formed water, which desorbed easily. However, CO adsorption was not completely inhibited, and instead of being oxidised it partially became surface formate and formyl (–CHO) species. The hydride phase decomposed at higher temperatures, which led to an increase of the selectivity toward CO oxidation. Nevertheless, it was still lower on Pd/CeO_2 than on Pt/CeO_2, likely due to the preference of metallic Pd for H adsorption rather than CO, and also because PdO_2 surface preferentially oxidises H with respect to CO. Teschner and co-workers [128] also examined Pt/CeO_2 catalysts (with nominal platinum loading of 5 wt %) with *operando* XPS but under different PROX mixtures, by varying oxygen pressure in the reactant feed of a first set of measurements and CO pressure in a second set, always maintaining the same H_2 pressure value for both series so that the total chamber pressure was approximately 1 mbar. The prepared catalyst removed 99 % of CO from a model feed, and the authors suggested the "classic" non-competitive mechanism of low-temperature CO oxidation on ceria-supported Pt [169] (e.g., CO adsorption on platinum and oxygen activation on the ceria support), and CO oxidation on the metal/oxide interface. Additionally, they found that oxygen vacancy formation, detected by *operando* XPS, was directly related to an enhancement of CO oxidation activity, because higher vacancy densities hindered water desorption, so that water molecules blocked H_{ads} oxidation sites and, therefore, more oxygen atoms were freely available for the oxidation of carbon monoxide. Ceria-supported Pt [170], Rh [171] and Pd [172] are also notably active in the low-temperature CO oxidation, a catalytic reaction important to lower automotive emissions [34,173]. For instance, Artiglia et al. [132] characterised the surface of a 3 wt % Pt/CeO_2 powder catalyst under 1 mbar of a reacting mixture of CO and O_2, employing time-resolved techniques to study the short-lived Ce^{3+} species, difficult to detect under steady-state conditions [174]. This new approach, based on NAP-XPS, consisted on the acquisition of a Ce 3d core level fast scan while switching the oxygen on and off (and replacing it with nitrogen) in a carbon monoxide/oxygen reaction mixture. The results obtained with the combination of these pulsed experiments and analyses of the depth profile, achieved by modifying the excitation energy, indicated that active Ce^{3+} sites were formed transiently at the most superficial layers of ceria and at the Pt/CeO_2 interface when oxygen was switched off [175]. Active sites were immediately reoxidised to Ce^{4+} upon dosing oxygen. Furthermore, when performing the same experiment on bare ceria they found insignificant reduction, which revealed the role of platinum as a promoter of the formation of Ce^{3+} at the interface. Recently, Pereira and co-workers have also investigated the performance of Pt/CeO_2-based catalysts for the low-temperature (< 423 K) CO oxidation [122], as mentioned earlier. The use of copper for ceria based catalyst is an interesting and promising alternative to noble metals for processes involving also CO oxidation, such as the water-gas shift reaction or the PROX [176,177]. Precisely, the work presented by Monte et al. consisted of the comparison of two morphologically different ceria supports (nanospheres and nanocubes) impregnated with a copper metallic phase subjected to interaction with carbon monoxide at different temperatures [130]. Their results provided direct evidence of interfacial Cu^+ sites, which are suggested to be the most active ones for CO oxidation [177,178], observed during near-ambient XPS experiments performed over both catalysts subjected to thermal reduction under a flow of diluted CO. These experimental results were supported by density functional theoretical calculations, supplemented with a Coulombic interaction parameter (DFT+U), and they demonstrated lower reducibility of the CuO

nanoparticles supported on ceria nanocubes, which led to a higher barrier to oxidise H_2 and thus to an enhancement of the CO PROX selectivity, as observed in previous investigations for ceria support with (100) faces [179]. Another type of design that has been used for CO oxidation reaction, and it has also been studied with *operando* spectroscopic techniques such as NAP-XPS, consists of bimetallic ceria-based catalysts. The work of Holgado et al. is focused on Au-Ni/CeO_2 bimetallic catalysts and their analogous monometallic samples [129]. In particular, they studied the effect of Ni incorporation into gold nanoparticles on their catalytic activity, as well as the distribution of Ni and Au atoms in bimetallic nanoparticles using various techniques. The development of gold bimetallic catalysts receives economic interest if the second metal is cheaper than Au, such as copper or nickel. Their investigation demonstrated that Au-Ni/CeO_2 bimetallic catalysts presented higher reactivity towards CO oxidation than monometallic Au/CeO_2 and Ni/CeO_2. The different *operando* characterization techniques used, including NAP-XPS, allowed them to establish a core-shell Au@NiO distribution, in which Ni surface atoms experienced an electronic effect on the local density of Ni d states from Au atoms in the core, modifying, in turn, their chemical and reactivity properties. It is worth mentioning that the bimetallic catalyst was studied by NAP-XPS under 1 mbar H_2 reducing atmosphere instead of CO (also a reducing agent) due to the possible formation of volatile Ni carbonyl species that could contaminate the analysis chamber. As already mentioned above, Della Mea and co-workers [121] also studied differently prepared ceria catalysts, altering their oxygen vacancy population, in order to design a rational ceria catalyst for CO oxidation. In this case, NAP-XPS conditions were 1 mbar of CO gas phase and temperatures from 373 to 773 K. Finally, another alternative to non-noble metals for PROX catalysts is the use of transition metal oxides, such as copper and cobalt-based catalysts, which show potential for this reaction [179–184]. Cobalt oxide catalysts have been extensively studied and, in order to improve their catalytic performance, reducible metal oxides (e.g., MnO_2, CeO_2) have been incorporated [183,184]. Although Co_3O_4 is a promising candidate as a CO-PROX catalyst, detailed knowledge of its active sites under reaction conditions is still missing. Therefore, in order to improve the understanding of PROX over cobalt oxide-based catalysts, Lukashuk et al. studied them employing advanced *operando* methods such as NAP-XPS at low photon energies, which allowed higher surface sensitivity to monitor changes in the surface composition [131]. In this case, the cerium oxide role was not as a support for Co nanoparticles but was instead loaded (10 wt %) on as received Co_3O_4 nanoparticles via wet impregnation. Both bare Co_3O_4 and CeO_2/Co_3O_4 catalysts were studied under pure CO (0.15 mbar), pure H_2 (0.4 mbar) or under PROX mixture (CO/O_2/H_2 ratio of 1/1/12, at 0.5 mbar), and the ability of Co_3O_4 to reduce in pure CO and easily reoxidise in O_2 suggested that adsorbed CO molecules react with lattice oxygen, which is refilled upon dosing O_2. Moreover, the addition of CeO_2 to Co_3O_4 promoted the PROX activity and increased the reduction temperatures under CO and H_2, although being a less active material.

3.2.2. Water-Gas Shift Reaction (WGS)

The water-gas shift (WGS) reaction (see Equation (1)) is widely used in industry to tune the CO/H_2 ratio in several chemical processes and to increase the yield of hydrogen in reforming processes. Again, ceria-based catalysts are promising candidates for such application [86,185], and their combination with noble metals (Au, Pt, Pd, Ni, Co) have received widespread attention due to the enhancement of their activity [76,86,169,186].

$$CO + H_2O \rightarrow CO_2 + H_2; \Delta H = -41.2 \text{ kJ/mol}, \tag{1}$$
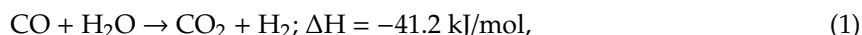
Wen and colleagues [133] used NAP-XPS to track the surface chemistry of two types of prepared ceria-based catalysts under WGS reaction conditions. They synthesised metal nanoclusters (Au, Pt, Pd, Cu) and supported them in channels of mesoporous ceria (abbreviated M@*mp*-CeO_2), as well as on ceria nanorods, and compared their performance for the WGS reaction. NAP-XPS measurements allowed the identification of the metallic state for Au, Pt, Pd and Cu nanoclusters, and revealed a higher concentration of oxygen vacancies under WGS reaction conditions on the internal concave surface of

mp-CeO$_2$ pores than on ceria nanorods surface. They associated the lower density of oxygen vacancies in ceria nanorods with stronger adsorption of OH$^-$ groups because the limited space of the concave internal surface of *mp*-CeO$_2$ increases repulsion between neighbouring hydroxyl groups. These results correlated well with the low calculated activation energy of WGS reaction on M@*mp*-CeO$_2$ catalysts in contrast to those of M/CeO$_2$ nanorods.

Ceria-based catalysts, most of them composed by ceria nanoparticles loaded with a metallic phase by incipient wet impregnation, have been widely used so far. Some cerium oxide films have also been assessed and quoted, yet few inverse configurations of catalysts (i.e., those in which ceria is supported on a metallic phase, exchanging its role as catalyst support) have been studied albeit in some cases they could apparently display enhanced activity compared to the conventional direct configuration [187,188]. From an economical point of view, catalysts formulations that combine copper and cerium oxide become more interesting than those based on noble metals. Copper-ceria catalysts have been proposed to operate at a relatively high temperatures above 573 K for WGS reaction, where CO and H$_2$O act as a reducing and oxidising agent of ceria, respectively, in the presence of active metallic Cu [188]. In this context, López Cámara et al. prepared an inverse CeO$_2$/CuO catalyst by a microemulsion-based method and examined it separately by *operando* XPS and DRIFTS spectroscopies under reactant mixtures relevant to the low temperature WGS reaction [134]. Their experiments demonstrated that water adsorption promoted the reduction of the catalyst to achieve its most active state since H$_2$O molecules favoured the decomposition of surface carbonate species which hamper the reduction process. Another attempt to shed light on the role of metal–oxide interfaces for the WGS reaction mechanism is the work of Mudiyanselage et al., who combined NAP-XPS, infrared reflection absorption spectroscopy (IRRAS) and DFT calculations to investigate the WGS reaction on CeO$_x$ nanoparticles deposited on Cu(111) and Au(111) substrates [39]. Cu(111) constitutes a typical benchmark for water-gas shift reaction studies, whereas Au(111) is inactive for such reaction. Nevertheless, it can be activated in the presence of ceria nanoparticles [187,189]. Under mild WGS conditions, adsorbed CO$_2$$^{\delta-}$ species were detected over both CeO$_x$/Cu(111) and CeO$_x$/Au(111) systems, as well as a high degree of reduction of ceria. Both NAP-XPS and DFT analyses showed that CO$_2$$^{\delta-}$ species, originated from a carboxy (HOCO) intermediate, are stabilized at the metal–oxide interface of the catalysts, and the simultaneous contribution of atoms present on the metal and the oxide allow the formation of such species, favouring a hydrogen production reaction mechanism which is not efficient on bare copper or bare ceria.

3.2.3. Soot Oxidation

Soot particles consist of an amorphous carbon core of few nanometers surrounded by a graphitic shell, often carrying many toxic compounds [190–192], and are one of the main pollutants emitted by diesel engines. Since thermal combustion of soot requires temperatures above 873 K with oxygen, and the temperature of diesel exhaust gases typically lies between 473 and 673 K, a suitable catalyst is needed to decrease the ignition temperature [193,194]. Among all the reported catalysts, ceria-based ones appear to be exceptional candidates for soot oxidation [195–197]. Concerning this reaction, it is generally assumed that it conforms to the Mars-van Krevelen mechanism, in which lattice oxygen atoms of the outmost layers of ceria are transferred onto soot, and exposure to gaseous O$_2$ subsequently fills up the vacancies created on the oxide [198,199]. Therefore, it is claimed that the formation of paramagnetic O$_2$$^-$ superoxide and diamagnetic O$_2$$^{2-}$ peroxide species takes place when reduced CeO$_{2-x}$ is exposed to molecular O$_2$ [26,200,201], which spillover onto soot surface [202], and that these active species are actually the main cause of soot oxidation [203,204]. By means of ambient pressure XPS, Soler et al. provided direct evidence of the redox chemistry and the influence of the reaction conditions in the oxidation of carbon soot over ceria-based catalysts [135]. With this aim, they investigated a sample of conventional ceria and a sample of Ce$_{0.8}$Zr$_{0.2}$O$_2$ mixed with soot, which were subjected to increasing temperatures (from 300 to 823 K) under 1 mbar argon atmosphere in a first set of experiments (with a final replacement of Ar with O$_2$ at 823 K), and under 1 mbar oxygen atmosphere in a second set of measurements. It is well-known that heating ceria under an inert atmosphere such as Ar results in the formation of oxygen vacancies and

the concurrent reduction of Ce^{4+} to Ce^{3+} [205], and the results showed indeed a Ce^{3+} increase with the temperature. However, when samples were treated with O_2, the amount of Ce^{3+} species remained low over the entire temperature range, since molecular oxygen rapidly reacted with the oxygen vacancies created at the ceria–soot interface. Interesting results were obtained when comparing the behaviour of CeO_2-soot and $Ce_{0.8}Zr_{0.2}O_2$-soot systems, since the amount of Ce^{3+} species upon heating under an Ar atmosphere was higher for the Zr-doped sample in all cases. Figure 1 shows Ce 3d (a, b) and O 1s spectra (c, d) of the $Ce_{0.8}Zr_{0.2}O_2$-soot sample recorded at 823 K under an argon environment (a, c) and after replacing Ar with O_2 at the same temperature (b, d). As expected, the replacement of the atmosphere caused an immediate and huge decrease of the Ce^{3+} amount (Figure 1a,b), but this phenomenon was also detected through O 1s spectra, which showed three different components.
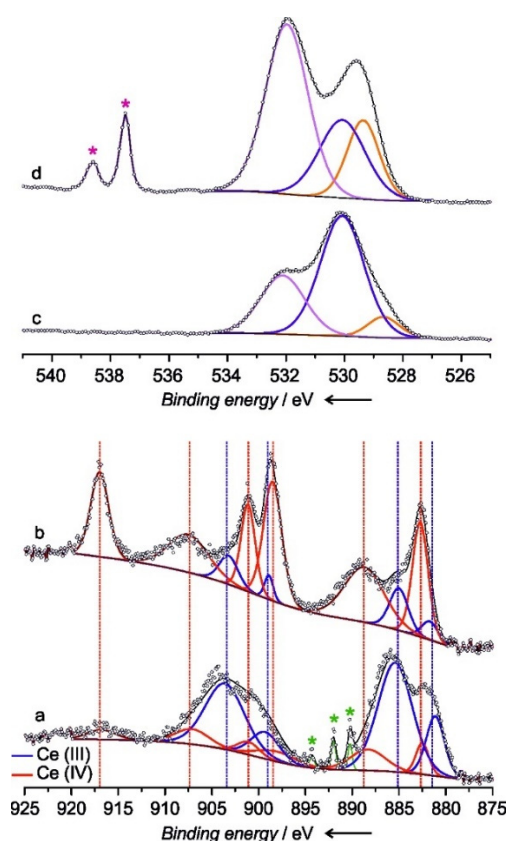

Figure 1. Ce 3d (**a**,**b**) and O 1s spectra (**c**,**d**) recorded over $Ce_{0.8}Zr_{0.2}O_2$-soot at 823 K under an argon atmosphere (**a**,**c**) and by replacing Ar with O_2 (**b**,**d**). Reprinted with permission from [135], copyright 2016, Wiley Online Library.

The bands at 528.7 and 530.2 eV of binding energy (Figure 1c,d) were attributed to ceria lattice oxygen and surface oxygen atoms with low coordination due to vacancy formation, respectively, and the peak at higher binding energy (532.2 eV) corresponded to superoxide species. When the argon gas phase was replaced by O_2, cerium oxide reoxidised and the O 1s band of the surface oxygen associated to Ce^{3+}, located at 530.2 eV, decreased its intensity (Figure 1d). Concurrently, the signal at 532.2 eV attributed to superoxide species appeared noticeably intense, demonstrating that these active oxygen species resulted from the reaction between molecular O_2 and oxygen vacancies. Therefore, the NAP-XPS technique allowed Soler and co-workers to demonstrate that soot oxidation over ceria-based materials involved a two-way cooperative mechanism: on one side, the formation of oxygen vacancies and Ce^{3+} species at the ceria–soot interface and, on the other side, the oxidation of the surface of soot by active superoxide species, generated from the reaction between the oxygen vacancies and gaseous O_2. Both routes occurred simultaneously and mutually strengthen each other.

3.2.4. CO_2 Hydrogenation

Nowadays, the synthesis of methanol from CO_2 is receiving strong attention [206–210] not only as a strategy to abate this greenhouse pollutant but also due to the potential use of CO_2 as an alternative source of carbon. The conversion of CO_2 to a valuable commodity such as synthesis gas (CO + H_2), hydrocarbon compounds (CH_4, olefins) and oxygenates (alcohols, ethers, acids) is, thus, highly desirable and numerous reports have appeared recently [206,211–215]. However, the activation of CO_2 is a challenging task due to the inconveniences related to the chemical inertness of CO_2. [207–210]. Currently, there is a particular resurgence in the study of CO_2 hydrogenation to C1 and higher alcohols ($xCO_2 + yH_2 \rightarrow C_xH_3OH + xH_2O$) [216–219], a process which is mainly associated with supported Cu-based catalysts with a Cu/ZnO/Al$_2$O$_3$ formulation [217,220,221]. Many research groups have investigated the optimization of the configuration of metal–oxide catalysts to activate CO_2 and convert it into valuable chemicals, and they found an improvement in the catalytic activity of Cu (which interacts very poorly with CO_2 on its own) [207,209,222] upon dispersing this metal on a ZnO substrate. Moreover, recent studies have identified the presence of ZnO$_x$ aggregates on top of Cu particles of a conventional Cu/ZnO catalyst active for methanol synthesis [220,223,224]. Graciani and co-workers presented a completely different catalyst formulation for CO_2 activation: a copper-ceria interface, which was highly active for methanol synthesis [136]. Approximately 0.2 ML of CeO$_x$ nanoparticles were deposited onto Cu(111), and the combination of NAP-XPS and ambient pressure infrared reflection absorption spectroscopy (AP-IRRAS) allowed the identification of adsorbed $CO_2^{\delta-}$ species on the surface of the CeO$_x$/Cu(111) catalyst under a CO_2/H_2 mixture (0.39 total mbar). C 1s spectrum presented a weak feature at ~ 284 eV, corresponding to a very small amount of C deposited on the surface of the catalyst because of the complete decomposition of CO_2. However, the spectrum was dominated by a main feature, which could be fitted with two bands at 289.2 and 288.4 eV, attributed to formate and carboxylate species, respectively. The former band was more intense than the band associated to $CO_2^{\delta-}$ species, denoting the high stability of formates, which may not be efficient as intermediate species in the CO_2 to CH_3OH conversion. With this work, Graciani et al. demonstrated that the metal–oxide interface generated by combining CeO$_x$ nanoparticles with Cu(111) provided adsorption/reaction sites for the synthesis of methanol, which would be very difficult to create on a pure metal or alloy surface. Following this work, Senanayake and colleagues compared the catalytic activity of ZnO/Cu(111) and CeO$_x$/Cu(111) systems when modifying the coverage of the oxides on the metallic substrate [137]. Their results indicated that the catalytic activity was strongly influenced not only by the oxide coverage, but also by the nature of the oxide. Specifically, CeO$_x$/Cu(111) was the most active catalyst among the inverse catalysts with an oxide/metal configuration, which have higher catalytic properties than conventional Cu/ZnO and Cu/CeO$_2$ catalytic systems. Again, by combining NAP-XPS and AP-IRRAS techniques, researchers found that Ce^{3+} oxidation state prevailed at low coverages and provided an efficient reaction pathway to adsorb and hydrogenate CO_2 through a $CO_2^{\delta-}$ intermediate, clearly indicating that the ceria-copper interface was essential for a high catalytic activity in the methanol synthesis.

A completely different catalyst configuration was investigated during CO_2 hydrogenation by Lin et al. [97], who prepared copper-ceria catalysts using different nanostructured ceria supports: nanorods (Cu/CeO$_2$-NR) and nanospheres (Cu/CeO$_2$-NS). By means of NAP-XPS and other techniques, they found that copper-ceria catalysts produced primarily CO at atmospheric pressures through the reverse water-gas shift (RWGS) reaction and a negligible amount of methanol. Cu/CeO$_2$-NR catalyst displayed a higher activity, which provides direct evidence of the morphological effect of ceria support on catalytic performance. Time-resolved X-ray diffraction (TR-XRD) and NAP-XPS measurements showed important oxidation state changes of the catalysts under reaction conditions, being metallic Cu and partially reduced ceria the active phase for the reaction. Studies with NAP-XPS also revealed a more effective CO_2 dissociative activation at high temperature and a preferential formation of bidentate carbonate and formate intermediates over ceria nanorods, which mainly expose (110) terminations. Finally, Winter and colleagues [138] reported a study of CO_2 hydrogenation over CeO$_2$-supported Ni catalysts with different metal loading. Their NAP-XPS measurements revealed that the oxidation state

of Ni remained metallic under reaction conditions for all metal loadings (0.5–5 wt % Ni), which implies that the Ni chemical state at the surface of the catalysts does not explain the selectivity differences. For all tested catalysts, ceria support appeared partially reduced under reducing conditions and also upon exposure to CO_2 and H_2 mixture, suggesting that oxygen from carbon dioxide did not reoxidise the CeO_x and consistent with the assumption that a mixture of Ce^{3+} and Ce^{4+} oxidation states plays a role in CO_2 activation.

3.2.5. Hydrocarbons

Natural gas, mainly composed of methane, is abundantly found in many large deposits around the word. However, most of it is located in remote zones and needs to be transported across wide distances before engaging in trade. Methane conversion to more useful and readily transferable chemicals has therefore become a primary issue for the chemistry society and has been extensively investigated during the last 30 years, and synthesis gas is the most economically available route known to date [225,226]. Depending on the purpose of industrial application, several syngas production routes from methane are available, some of them described below.
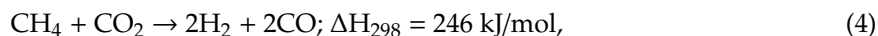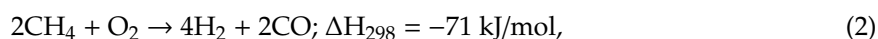
Methane Partial and Complete Oxidation

The catalytic partial oxidation of methane (MPO) to syngas ($CO + H_2$) is a slightly exothermic reaction first suggested in 1929 by Liander [227], who investigated it for the ammonia process. As high methane conversion and syngas selectivity are achieved at short contact times, this reaction can be used to transform methane, the main constituent of natural gas, into syngas in small-medium scale plants, e.g., to produce it for distribution [228–233]. In the past decades, many groups have studied the production of syngas via MPO using Ni, Co and noble metals supported on reducible oxides such as Al_2O_3, $MgAl_2O_4$, CeO_2 and ZrO_2 [234–238]. Focusing on ceria-based catalysts, Zhu et al. [139] examined the surface chemistries of CeO_2 doped with Pd, Pt and Rh during methane partial oxidation at different temperatures by means of NAP-XPS. Under the same catalytic conditions (2.6 and 1.3 mbar of CH_4 and O_2, respectively) Pt and Rh appeared completely oxidised on the ceria surface, whereas metallic Pd nanoparticles were detected, which induced quite different catalytic activities in MPO. Among all catalysts, Rh-doped ceria exhibited the highest catalytic performance and selectivity for methane partial oxidation.

The catalytic complete oxidation of methane constitutes a decisive process to remove the unburned methane emitted from natural gas power plants or engines of vehicles using natural gas or liquefied petroleum gas as fuels. Unlike gasoline-fuelled engines, engines using natural gas or liquefied petroleum gas combust at relatively low temperatures, typically lower than 873 K [239]. Therefore, a catalyst which is highly active below 873 K for complete transformation of methane into CO_2 is required to remove the unburned methane or short-chain hydrocarbons in the exhaust line before releasing it into the environment, since CH_4 is a much stronger greenhouse pollutant than CO_2 [240–243]. Noble metal-based catalysts such as supported Pd and Pt have been extensively investigated, owing to their high catalytic activity for complete oxidation of methane at relatively low temperature [244–247]. However, they are limited to any use at large scale due to their restrictively high cost, extremely low abundance in earth and prompt deactivation of catalysts caused by sintering of supported noble metal nanoparticles. To improve the lifetime of noble metal-based catalysts and decrease their price, dispersion of nanoparticles on high surface-area oxide is used. In this sense, ceria is an important support in oxidative catalysis owing to its high activity in molecular O_2 activation [3]. With this aim, Dou et al. [140] prepared a Co_3O_4/CeO_2 nanocomposite catalyst that consisted of Co_3O_4 nanoparticles supported on ceria nanorods, and investigated its surface during complete oxidation of CH_4 (flowing mixture of 0.26 mbar CH_4 and 1.33 mbar O_2) in the temperature range of 423–773 K with near-ambient XPS. Kinetic studies of pure CeO_2, pure Co_3O_4 and Co_3O_4/CeO_2 catalysts were first performed to calculate the different activation energies for complete oxidation of methane, and the results suggested a synergetic effect between both oxides since the nanocomposite catalyst exhibited lower activation

energy than that of pure ceria and cobalt oxide. As for NAP-XPS studies, C 1s spectra allowed the identification of a stable intermediate methyl species formed on the surface of Co_3O_4/CeO_2 during catalysis, which could be generated through dissociation of C−H of methane on Ce^{4+}, Co^{3+} or Co^{2+} sites, since no oxygen vacancies were formed and detected on the cerium oxide support. Very similar results were obtained by Zhang and co-workers [141], who prepared CeO_2 nanorods with supported NiO nanoclusters of 10–12 nm average size and studied them under the same methane complete oxidation conditions as the work of Dou and colleagues [140]. Tracking the evolution of C 1s NAP-XPS features with increasing temperature under reaction conditions, they deduced the formation of a stable CH_3-like intermediate bound to the Ni cation at 423–473 K. The generated surface CH_3 could be further activated to form CH_2 or even CH species, which in turn could combine with surface lattice oxygen atoms to form CO_2 and H_2.

Dry Reforming of Hydrocarbons

Natural gas and biogas, composed mainly of methane, have become cheap and abundant alternatives to traditional fossil fuels such as petroleum and coal [248]. They can be combusted with oxygen for the production of electricity or heat, but they can also be used as a carbon source in the manufacture of commodity chemicals [249]. This can be achieved by means of reforming methane to synthesis gas (CO/H_2) and subsequently using syngas in industrial processes such as methanol synthesis, ammonia synthesis, hydrogenations or Fischer-Tropsch (FT) reactions [250,251]. There are three oxidative routes to generate syngas from methane: partial oxidation (Equation (2)), steam reforming (Equation (3)) and dry reforming (Equation (4)).

$$2CH_4 + O_2 \rightarrow 4H_2 + 2CO; \Delta H_{298} = -71 \text{ kJ/mol}, \tag{2}$$

$$CH_4 + H_2O \rightarrow 3H_2 + CO; \Delta H_{298} = 206 \text{ kJ/mol}, \tag{3}$$

$$CH_4 + CO_2 \rightarrow 2H_2 + 2CO; \Delta H_{298} = 246 \text{ kJ/mol}, \tag{4}$$

Although dry reforming of methane (DRM) is the most difficult of these processes, it is attractive as an initial step in the Fischer-Tropsch reaction and methanol synthesis, due to its CO:H_2 = 1:1 production ratio [252,253]. Additionally, dry reforming of methane is a desirable process since it converts two active greenhouse gases (CO_2 and methane) into syngas, representing a promising approach to mitigate problems caused by global emissions [254,255]. The high stability of C−H bonds of methane makes its activation difficult [256], and the extraction of oxygen from CO_2 entails a large activation barrier [249]. Therefore, enabling low-temperature activation of methane is a major technological goal, and a detailed investigation of the DRM through in situ techniques will help to obtain a better understanding of the reaction mechanism for the selective CH_4 activation by evading pathways to complete oxidation. Typically, pure noble metals (e.g., Pt, Pd, Rh, Ru, and Ir) are highly active for this reaction, but at elevated temperatures suffer from rapid deactivation by particle sintering and chemical poisoning (carbon deposition) [257–259]. Late transition metals such as Ni, Co and Fe represent an alternative option owing to its low cost and higher abundance [260,261]. Again, the dispersion of nanoparticles of these metals on oxide surfaces is an attractive option as a catalyst for the DRM process.

Among all the formulations, the inexpensive Ni/Al_2O_3 is the most widely used catalyst for this reaction, although research is still required in order to diminish its deactivation by carbon formation and improve the whole process. Ceria is also an excellent candidate as a support to improve the catalytic performance of nickel in these reforming reactions, particularly due to the SMSI between the oxide and the deposited metals [262]. Precisely, Gonzalez-Delacruz et al. prepared a Ni/CeO_2 catalyst in order to study its behaviour in the dry reforming of methane with the use of various in situ techniques, such as X-ray absorption spectroscopy (XAS) and NAP-XPS [142]. The sample was subjected to different treatments at 923 K, the highest achievable temperature with their near-ambient XPS apparatus. Under

1.33 mbar DRM conditions (CH_4/CO_2 mixture), Ce 4d spectra of the catalyst presented no changes with respect to the fresh sample, but when it was submitted to a pure methane treatment at the same temperature, important changes appeared in the profile of Ce 4d spectra, revealing an almost complete reduction of the ceria surface to Ce^{3+} species. The original signal was not entirely recovered after subsequent treatment with pure CO_2, indicating the presence of a Ce^{3+} and Ce^{4+} mixture on the surface of the support. This opposition to be reoxidised was most probably caused by the deposition of carbon on the catalyst, which could be observed by scanning electron microscopy (SEM) after the DRM reaction. The same catalyst formulation was studied by Liu and co-workers [143], although they prepared a model Ni/CeO_2 catalyst which contained ~ 2 nm size NiO nanoparticles dispersed on a CeO_{2-x}(111) substrate. After annealing the sample at 500 K, some Ni particles sintered and a large fraction of Ni migrated into the ceria support, forming a $Ce_{1-x}Ni_xO_{2-y}$ solid solution. In this case, they investigated the interaction of CH_4, CO_2 and a CH_4/CO_2 mixture with model CeO_2(111) and Ni/CeO_2(111) surfaces (in a temperature range of 300−700 K) with NAP-XPS to better understand the chemistry of the DRM process on this type of catalyst. Under a pressure of 0.13 mbar of methane, the bands that appeared in the C 1s region at 300 K indicate that methane dissociates on the Ni/CeO_2 surface at room temperature. When the first hydrogen atom is removed from methane molecules, they quickly dissociate and a $CH_3 \rightarrow CH_2 \rightarrow CH \rightarrow C$ transformation occurs on the catalyst surface, generating C atoms that ultimately react with ceria lattice oxygen atoms to result in gaseous CO and adsorbed CO_x species, the latter ones were evidenced by a strong band near 290.2 eV [39]. Weak features at 285–286 eV were probably originated by CH_x species on the surface. However, at higher temperatures, CO_x and CH_x features no longer appeared in the C 1s region. The corresponding spectrum for the Ce 4d and Ni 3p regions did not show evident signs of modifications of Ce^{4+} and Ni^{2+} oxidation states between 300−500 K, but at 700 K their line shape clearly changed, denoting the reduction of both phases to Ce^{3+} and Ni^0. The amount of Ce^{3+} species formed on a plain CeO_2(111) surface at temperatures above 600 K was much smaller than that on a Ni/CeO_2(111) surface under similar conditions. Under 0.13 mbar of CO_2, a strong feature for adsorbed CO_x species at 290.2 eV dominated the C 1s XPS spectrum for both CeO_2(111) and Ni/CeO_2(111) surfaces, but disappeared upon heating the samples to 500 or 700 K. Additionally, no change in the oxidation state of Ce^{4+} and Ni^{2+} species was observed at any temperature. Therefore, the reactivity of the system towards CO_2 was not affected by the addition of nickel to CeO_2(111).

Under an atmosphere of 0.26 mbar CH_4 and CO_2 at 300 K, the C 1s region of the Ni/CeO_2(111) catalyst exhibited a CO_x band near 290.2 eV with enhanced intensity, due to the presence of both gaseous reactants, as well as peaks of adsorbed CH_x species (285−286 eV) and CH_4 and CO_2 gas phases (see Figure 2). The signals for adsorbed CO_x and CH_x species disappeared when the sample was heated from 300 to 500 K. When heating to 700 K, the spectrum showed features for gaseous CO and surface CO_x species in addition to the signals for the reactants, as illustrated in Figure 2. Below 700 K, the surface of the catalyst was mainly composed of Ni^{2+} and Ce^{4+} species, and no catalytic activity was observed. Nevertheless, at 700 K the system became catalytically active when the decomposition products of methane generated Ni^0 and partially reduced Ce^{4+} to Ce^{3+}. Under a CH_4/CO_2 mixture, the Ce^{3+} fraction generated was again much smaller than under pure methane due to the presence of CO_2 in the gas phase, which reacts with the ceria surface and recovers a significant amount of the oxygen vacancies, $CO_2(g) + Vac \rightarrow CO(a) + O–Vac$. Moreover, the C formed by total dissociation of methane did not react with ceria lattice oxygen atoms but with the O adatoms generated by the decomposition of CO_2 instead.

Following this work, Lustemberg et al. published an investigation related to the effect of Ni coverage on the performance of the same Ni/CeO_2(111) catalyst for dry reforming of methane [144]. Although they only performed NAP-XPS experiments for a system with low Ni content (Θ_{Ni} ~ 0.1 ML) to avoid the formation of NiC_x, Ni/CeO_2(111) surfaces with Ni coverages from 0.15 ML to 0.5 ML were studied by multiple characterization techniques. The obtained results revealed that ceria surfaces with a small coverage of Ni are able to activate methane at room temperature, generating adsorbed CO_x and CH_x

species. In other words, Ni coverage on ceria substrate extremely determines metal–support interactions, which are in turn responsible for the low barrier for C−H bond cleavage of methane on this metal/oxide system. To complete the investigation, Liu and co-workers studied the metal–oxide interactions of a series of metal/CeO_2(111) (metal = Co, Ni and Cu) under DRM conditions at relatively low temperatures (600−700 K) [146]. The behaviour of Co, Ni and Cu on a CeO_2(111) substrate (with a coverage of 0.2 ML) was first compared using conventional XPS and kinetic testing, as well as theoretical calculations based on DFT. Among the systems examined in a temperature range of 300–700 K, Co/CeO_2(111) exhibited the best catalytic performance for dry reforming of methane, whereas Cu/CeO_2(111) had negligible activity. Catalytic tests were in agreement with in situ XPS measurements performed to study their ability to activate pure CH_4, which showed that the surface with cobalt reduced the most and, consequently, reacted better with methane than Ni/CeO_2(111) or Cu/CeO_2(111) catalysts. Indeed, the partial reduction of ceria support is essential for the activation of both reactants. *Operando* XPS was then employed to study the chemical changes in the best Co/CeO_2(111) catalyst under reaction conditions (CH_4/CO_2 mixture), and experiments indicated that methane dissociates on the ceria support with 0.2 ML of Co at temperatures as low as 300 K, generating CH_x and CO_x species on the surface. Both ceria and Co^{2+} appeared partially reduced at 500–700 K, but at 700 K and under DRM conditions, CO_2 dissociates on the oxide surface and slightly reoxidises Co and Ce^{3+}, establishing a catalytic cycle without coke deposition. Additionally, catalytic activity for C2 production was also observed at 650 K, since a significant part of the adsorbed CH_x species recombined to yield ethane and ethylene. Catalytic activity of the Co/CeO_2(111) catalyst for DRM and ethane/ethylene production was also examined as a function of cobalt coverage, and they observed a maximum at a coverage of approximately 0.15 ML and 0.1 ML for syngas and ethane/ethylene production, respectively. Therefore, not only the nature of the metal is crucial for the catalyst DRM activity and stability, but also the preservation of a low metal loading (below 0.2 ML), since at higher loadings carbon is formed on the surface leading to catalyst deactivation.
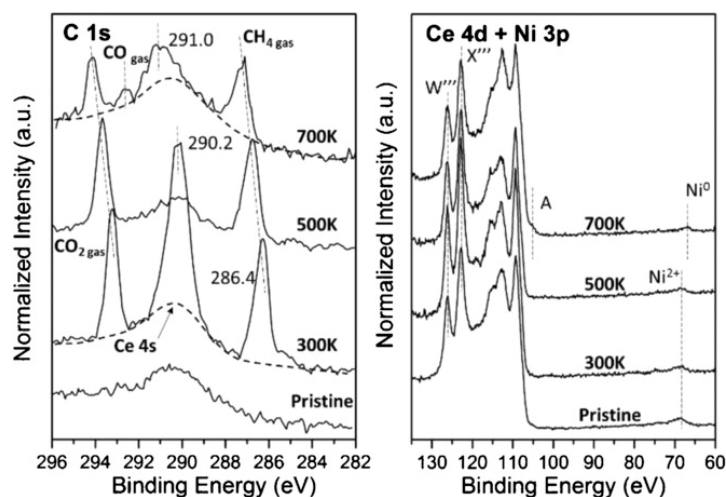

Figure 2. C 1s and Ce 4d + Ni 3p spectra of the Ni/CeO_2(111) catalyst (Θ_{Ni} ~ 0.1 ML) surface under 0.13 mbar CH_4 and 0.13 mbar CO_2 at different temperatures. Reprinted with permission from [143], copyright 2016, Wiley Online Library.

In another report, Zhang et al. also investigated the dry reforming of methane over a series of ceria-supported powder catalysts with different cobalt loadings (2−30 wt %) in order to elucidate the interaction between Co and CeO_2 during the catalytic process, and thus optimise the design of a catalyst with improved activity [147]. Various in situ techniques were used to achieve so, such as in situ time-resolved XRD (TR-XRD). Their results showed a huge reduction of the CoO_x-CeO_2 system at temperatures between 473 and 623 K as a consequence of the hydrogen produced by the dissociation of C−H bonds in methane, which fully converted the Co_3O_4 oxide to metallic Co and partially reduced Ce^{4+} to Ce^{3+}. A catalytic cycle for DRM was achieved on the catalysts upon dosing CO_2, at temperatures

below 773 K. Among the different Co loaded catalysts, the 10 wt % Co/CeO$_2$ catalyst appeared to have the highest catalytic performance, exhibiting desirable stability for the DRM process with the lowest effect of coke accumulation. For this reason, and since TR-XRD is a primarily bulk-sensitive technique, the surface of the 10 wt % Co/CeO$_2$ sample was also examined under reaction conditions with NAP-XPS. As depicted in Figure 3, results showed a dynamic evolution in the oxidation state of the catalyst under reaction conditions. The partial reoxidation of ceria upon switching the H$_2$ reducing atmosphere to a CH$_4$/CO$_2$ mixture is evident at room temperature since Ce^{3+} features at the Ce 3d region attenuate and the bands of Ce^{4+} species become more intense. A temperature increase led to a further reduction of ceria, as seen in Figure 3, although CO$_2$ weakened the reducing effects of methane. As expected, the initial Co$_3$O$_4$ phase was completely reduced to metallic Co after the H$_2$ pretreatment. When the atmosphere was changed to DRM conditions, a small amount of cobalt reoxidised, but it remained mainly Co^0 as the reaction advanced to 773 K. Analyses of the O 1s region allowed the detection of CO$_x$ species (e.g., carbonate, carboxyl, bicarbonate) adsorbed on the catalyst surface, ascribing CO$_x$ as a possible reaction intermediate.
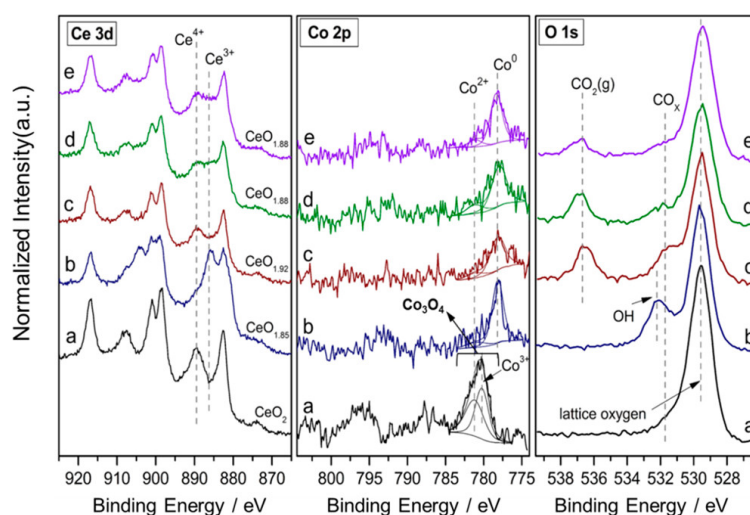

Figure 3. NAP-XPS spectra of the Ce 3d, Co 2p and O 1s regions of 10 wt % Co/CeO$_2$ catalyst (**a**) as prepared at 300 K, (**b**) cooled to 300 K after 1 h of H$_2$ pretreatment at 823 K and during the dry reforming of methane (DRM) reaction (~ 0.1 mbar of CH$_4$ + ~ 0.1 mbar of CO$_2$): (**c**) at 300 K, (**d**) 673 K and (**e**) 773 K. Reprinted with permission from [147], copyright 2018, American Chemical Society.

Xie and colleagues [148] also investigated the activity for DRM of a cobalt-based catalyst; they prepared a PtCo/CeO$_2$ bimetallic catalyst and compared it with the corresponding monometallic ones to explore the Pt-Co synergy for DRM. As in situ XRD, DRIFTS and XAFS analyses provided bulk-averaged structural information, NAP-XPS experiments were performed for the bimetallic sample to obtain surface information during reaction conditions. Again, the results revealed a dynamic evolution in the chemical composition of the catalyst surface: upon exposure to the reactant stream, both Pt and ceria slightly oxidised due to the presence of CO$_2$ in the environment. With the combination of multiple techniques such as in situ XRD, TPR, in situ XAFS and DRIFTS, PtCo/CeO$_2$ sample was found to have the highest catalytic activity, and both Pt-Co alloy and isolated Co particles co-existed in its structure. Nevertheless, the Pt-Co alloy is the dominant active structure, which remained nearly metallic during the reaction.

Very recently, Liu and co-workers proposed another ceria-based catalyst formulation for dry reforming of methane by changing the nature of the supported metal, a key component in such catalytic process [149]. In their work, they reported a highly active and stable ceria-supported Ru-nanocluster (< 1 nm) catalyst (denoted as Ru(NC)−CeO$_2$) for the DRM, since Ru-based catalysts have exhibited high activity and stability against the deactivation by carbon accumulation [257,263]. In situ XRD

and XAFS were used to elucidate the structure-reactivity relationship that caused the remarkable catalytic performance, whereas the surface chemistry and possible surface-active intermediates were monitored by NAP-XPS and DRIFTS. As the activation of methane is a crucial step in the DRM process, the catalyst was subjected to an atmosphere of pure methane before studying it under DRM conditions with *operando* XPS. Ce 3d NAP-XPS spectra evidenced a gradual reduction of ceria surface, that is, the formation of oxygen vacancies and Ce^{3+} species, after exposing the sample to pure CH_4. Ceria reduction, which occurred at temperatures as low as 423 K, was accompanied by reduction of RuO_2, as expected. Under a mixture of CH_4/CO_2 at 423 K, the ceria surface underwent an initial reduction, comparable to the case of methane alone, suggesting an effective activation of methane. Figure 4 illustrates the NAP-XPS spectra for the Ce 3d and C 1s + Ru 3d regions of the 0.5 wt % Ru(NC)–CeO_2 catalyst under DRM conditions. At temperatures greater than 573 K, a relevant degree of ceria reoxidation was observed, which involved a significant dissociation of CO_2 on either ceria or Ru sites, generating O adatoms and subsequently refilling the oxygen vacancies of the surface. This dual-site mechanism not only allows the direct activation of CO_2 on the metal sites, but also allows the O adsorbed on ceria sites to assist the oxidation of surface carbon on Ru sites.
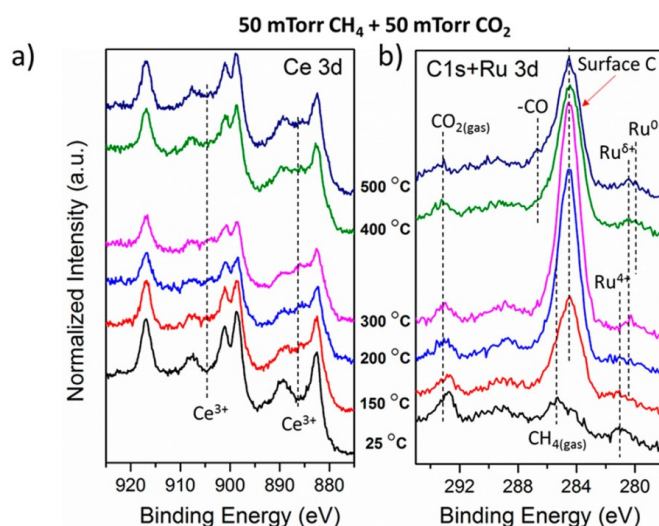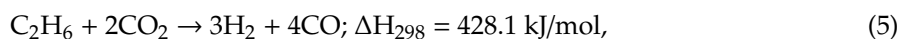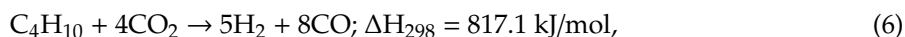

Figure 4. (**a**) Ce 3d and (**b**) C 1s + Ru 3d NAP-XPS spectra of the 0.5 wt % Ru(NC)–CeO_2 catalyst under ~ 0.13 mbar CH_4/CO_2 (1:1). Reprinted with permission from [149], copyright 2019, American Chemical Society.

As depicted in Figure 4b, carbon deposited on the catalyst surface as the reaction developed. At 573 K or below, methane activation led to the formation of surface carbon on the catalyst, and at temperatures higher than 573 K, the O adatoms generated from CO_2 dissociation reoxidise the surface carbon due to the intimate Ru−O−Ce interaction, completing the catalytic cycle. This evolution is evidenced by a clear drop of surface carbon peak intensity, at ~ 284.6 eV. Figure 4b also revealed that under reaction conditions, the active structure of the Ru(NC)–CeO_2 catalyst was partially oxidised Ru clusters stabilized by reduced ceria ($Ru^{\delta+}$–CeO_{2-x}).

We have seen that DRM is an attractive process since it transforms two greenhouse gases (CO_2 and methane) into syngas, which can be subsequently used to produce value-added chemicals and fuels. Nevertheless, DRM is a highly endothermic reaction and demands high temperatures to achieve significant conversion. Therefore, an alternative approach to convert CO_2 to syngas is the use of ethane and other light alkanes (e.g., butane) present in shale gas [264,265]. Dry reforming of ethane (DRE, Equation (5)) and dry reforming of butane (DRB, Equation (6)) generate synthesis gas through:

$$C_2H_6 + 2CO_2 \rightarrow 3H_2 + 4CO; \Delta H_{298} = 428.1 \text{ kJ/mol,} \tag{5}$$

$$C_4H_{10} + 4CO_2 \rightarrow 5H_2 + 8CO; \Delta H_{298} = 817.1 \text{ kJ/mol}, \tag{6}$$

Temperatures of approximately 760 and 720 K are required to attain the 50% conversion of CO_2 in DRE and DRB, respectively, under equilibrium conditions of stoichiometric ratio. Due to the decrease of the reaction temperatures with respect to the DRM process, catalyst deactivation occurs to a lower extent and, consequently, there are more options in the design of a stable catalyst.

Yan et al. prepared model and conventional $PtNi/CeO_2$ catalysts, as well as their corresponding monometallic catalysts, and compared their catalytic performance for DRE and DRB [145]. In spite of the elevated cost of noble metal loaded catalysts (such as Pt) for large-scale processes, they commonly show higher resistance to coke accumulation and can be used to promote Ni-based catalysts so as to reduce C deposition and, hence, increase its lifetime. Results from both model thin films and supported powder catalysts revealed that the $PtNi/CeO_2$ bimetallic catalyst shows higher activity than the corresponding monometallic samples. In their study, multiple spectroscopic techniques, including NAP-XPS, in situ XRD, in situ XAFS and DRIFTS were employed to probe catalyst structures and surface intermediate species under reaction conditions. NAP-XPS measurements were performed only on model catalysts and, due to the stronger interaction of butane in comparison to ethane, only DRB was investigated with this technique. Model catalysts were prepared by depositing small coverages of PtNi, Pt or Ni (0.1 ML) onto a CeO_2 film (3 ML) over a TiO_2 (110) substrate, while supported catalysts were loaded with 1.7 wt % of Pt and 1.5 wt % of Ni, corresponding to an atomic ratio Pt:Ni of 1:3. Under reaction conditions (0.13 mbar CO_2 and 0.26 mbar butane), ceria substrate and metals, except for the Ni of Ni/CeO_2, were partially reduced. Interestingly, Ni of $PtNi/CeO_2$ catalyst was reduced to metallic nickel, which indicates that the presence of Pt enhances Ni reduction. In the C 1s region, a band attributed to carbonate and carboxyl ($CO_2^{\delta-}$) was observed for all catalysts, indicating the effective activation of CO_2 for all three surfaces. Additionally, two more peaks appeared at 284.5 and 289.8 eV, which were assigned to the adsorbed $O-C_xH_y$ species (generated from butane decomposition) and adsorbed formate, respectively. The latter was generated upon hydrogenation of adsorbed carbonate/carboxylate species. It is worth noting that each surface presented different band intensity of the adsorbed $O-C_xH_y$ species, following the trend $PtNi/CeO_2 > Ni/CeO_2 > Pt/CeO_2$, which denoted that Ni is more active than Pt, although PtNi bimetallic surface further improves butane activation.

3.2.6. Alcohols

The high environmental impact of fossil fuels has urged the need for alternative energy sources over the last decades. Hydrogen is being considered as the future clean and affordable fuel to be used in fuel cells or in large-scale processes such as ammonia synthesis, considering the abundant availability of H_2-containing substances in nature, its high energy content (120.7 kJ/g) and its non-polluting combustion. For this reason, fuel cell research and development have received a huge amount of funding in the last years. Among the multiple chemical carriers of hydrogen, light alcohol methanol and ethanol constitute important candidates to produce H_2 via different catalytic pathways.

Steam Reforming of Alcohols

Hydrogen production from ethanol has been extensively studied, since ethanol can be obtained by the fermentation of agricultural wastes (biomass) and, therefore, constitutes a carbon-neutral renewable precursor [266,267]. Currently, catalytic research is focusing on steam reforming of ethanol (SRE), partial oxidation of ethanol (POX) and the oxidative steam reforming (OSR) as potential process candidates to produce H_2 [267,268]. SRE (see Equation (7)) is the most efficient pathway of renewable hydrogen production, but it is an endothermic reaction that requires an active catalyst and a sufficient energy input to obtain a high H_2 yield and ethanol conversion with a reasonable reaction rate.

$$C_2H_5OH + 3H_2O \rightarrow 6H_2 + 2CO_2; \Delta H_{298} = 173.3 \text{ kJ/mol}, \tag{7}$$
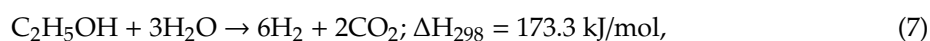
Generally, noble metals supported on inorganic oxides have proved to exhibit higher catalytic activity for SRE than non-noble metal-based ones [269–274]. As an alternative to expensive metals such as Rh, Ru, Pd and Pt, non-noble metal-based catalysts (Ni, Co and Cu) have also been investigated at higher metal loadings, and they have become promising catalysts for the reaction [275–280]. The catalytic performance can also be influenced by the oxide support. Among the various metal oxides studied, ceria has exhibited a key role in reducing coke accumulation on the surface of the catalyst as well as modifying the reaction kinetics [281,282]. As already stated, the excellent performance of ceria as a support or even as a catalyst is associated to its high OSC and its rapid change between Ce^{4+} and Ce^{3+} oxidation states. Carbon deposition is mitigated on account of the transportation of oxygen species from ceria to the supported metal, which confers significantly improved catalytic activities under SRE conditions.

Bimetallic catalysts have also been studied in the SRE reaction. Divins et al. used the NAP-XPS technique to demonstrate that the presence of a reducible CeO_2 support greatly influenced the surface rearrangement of bimetallic Rh-Pd nanoparticles under SRE conditions on real catalysts [68].

They performed the reaction between ethanol and water ($EtOH:H_2O = 1:6$) at 823 K and a sample pressure of 0.05 mbar over (a) unsupported model $Rh_{0.5}Pd_{0.5}$ nanoparticles (NPs) and (b) $Rh_{0.5}Pd_{0.5}$ NPs supported on ceria powder. Among noble metals, Rh is highly active for both C–C and C–H bond cleavage, induces hydrogenation reaction and causes very low carbon deposition [283]. Both systems were subjected to reducing, oxidising and SRE conditions to produce H_2, and three different photon energies (670, 875 and 1150 eV) were used to obtain a depth-profile study of both samples and deduce the rearrangement and the development of a core-shell structure induced by the environment. Results showed that unsupported model NPs were more strongly reduced for all the atmospheres tested. Upon reduction with H_2 at 573 K, Pd segregated towards the surface for both unsupported and supported NPs. Nevertheless, under SRE conditions at 823 K, unsupported NPs suffered from a restructuration as Rh atoms migrated toward the surface and became reduced due to the reducing effect of the hydrogen produced during the ethanol steam reforming reaction. No migration of Rh or Pd was found for ceria supported NPs under ESR and, most importantly, both metals became more oxidised, as illustrated in Figure 5. Moreover, palladium developed a core-shell structure of oxidation states: as seen in Figure 5, the outer shell (670 eV photon energy spectrum) of the $Rh_{0.5}Pd_{0.5}/CeO_2$ catalyst exhibited a high amount of oxidised Pd species. This oxidation of the outermost layers of the supported NPs is likely due to the creation of –OH groups at the catalyst surface upon activation of water by ceria. Therefore, the interaction of the metal NPs with the support plays a crucial role in reactions catalysed by the RhPd NPs since it limits the dynamic reorganization of the metals under operating conditions ("quenching effect") and supplies active oxygen atoms to the metals at the surface of the NPs. In a deeper analysis of the same $Rh_{0.5}Pd_{0.5}/CeO_2$ system, Soler et al. reported the influence of the support morphology in the reorganization of bimetallic nanoparticles, which has important consequences for catalytic performance, also by means of NAP-XPS [69]. With this aim, they monitored the surface composition and chemical states of preformed $Rh_{0.5}Pd_{0.5}$ model NPs of 4 nm size supported on two different types of nanoshaped ceria: nanocubes (CeO_2-c) and nanorods (CeO_2-r), during the catalytic SRE at 823 K. Both systems were also exposed to reducing, SRE and final reducing conditions, and again three different photon energies were used to acquire the corresponding spectra and perform a depth-profile study of the bimetallic NPs under *operando* experiments, as previously described [68]. Under initial H_2 conditions at 573 K, both catalysts exhibited the same amount of oxidised and reduced Rh, whereas $Rh_{0.5}Pd_{0.5}/CeO_2$-c contained a larger fraction of metallic Pd than $Rh_{0.5}Pd_{0.5}/CeO_2$-r, which also exhibited a minor fraction of Pd^{IV} species, almost inexistent in CeO_2-c. Furthermore, a core-shell structure of oxidation states of Pd was observed for the bimetallic NPs supported on CeO_2-r, Pd being more reduced in the inner region of the bimetallic NPs. However, the two catalysts showed completely different behaviours under SRE conditions at 823 K: bimetallic NPs supported on CeO_2-c appeared dramatically oxidised, with predominant Pd^{4+} and Rh^+/Rh^{3+} species, whereas Pd of bimetallic NPs supported on nanorods became more reduced with respect to

the activation treatment under H_2, with minor fractions of Pd^{2+} and Pd^{4+} species. This difference in the catalytic performance between both systems can be explained by the ability of the different exposed crystallographic planes to release oxygen atoms: indeed, oxygen vacancy formation on {100} planes of ceria nanocubes is thermodynamically more favourable than on {110} and {111} planes usually found in CeO_2-r and polycrystalline ceria [4]. For this reason, ceria nanocubes easily transferred oxygen atoms to the supported NPs, which resulted in their oxidation. Moreover, SRE reaction did not progress on $Rh_{0.5}Pd_{0.5}/CeO_2$-c because, although ethanol can be effectively dehydrogenated into acetaldehyde and H_2 over metal oxides [284], the metallic function is required for methane steam reforming, which constitutes the last step in the SRE. Additionally, NPs of both catalysts rearranged under SRE conditions at 823 K: Pd segregated toward the surface of the NPs supported on CeO_2-r, while the exact opposite (Rh segregation to the surface) was observed for the $Rh_{0.5}Pd_{0.5}/CeO_2$-c system. Finally, the reduction step at 823 K caused the reduction of the metals for both systems, but did not result in a modification of the relative distribution of Pd and Rh. As for Ce 3d spectra, illustrated in Figure 6, they indicated a sharp increase of Ce^{3+} species for both catalysts upon exposure to H_2 at 823 K, as expected. Although the Ce^{3+}/Ce^{4+} ratio of the $Rh_{0.5}Pd_{0.5}/CeO_2$-c catalyst exceeded that of $Rh_{0.5}Pd_{0.5}/CeO_2$-r during the last reduction step, the latter exhibited higher Ce^{3+}/Ce^{4+} ratio under SRE conditions with respect to $Rh_{0.5}Pd_{0.5}/CeO_2$-c, which was attributed to its higher hydrogen production.
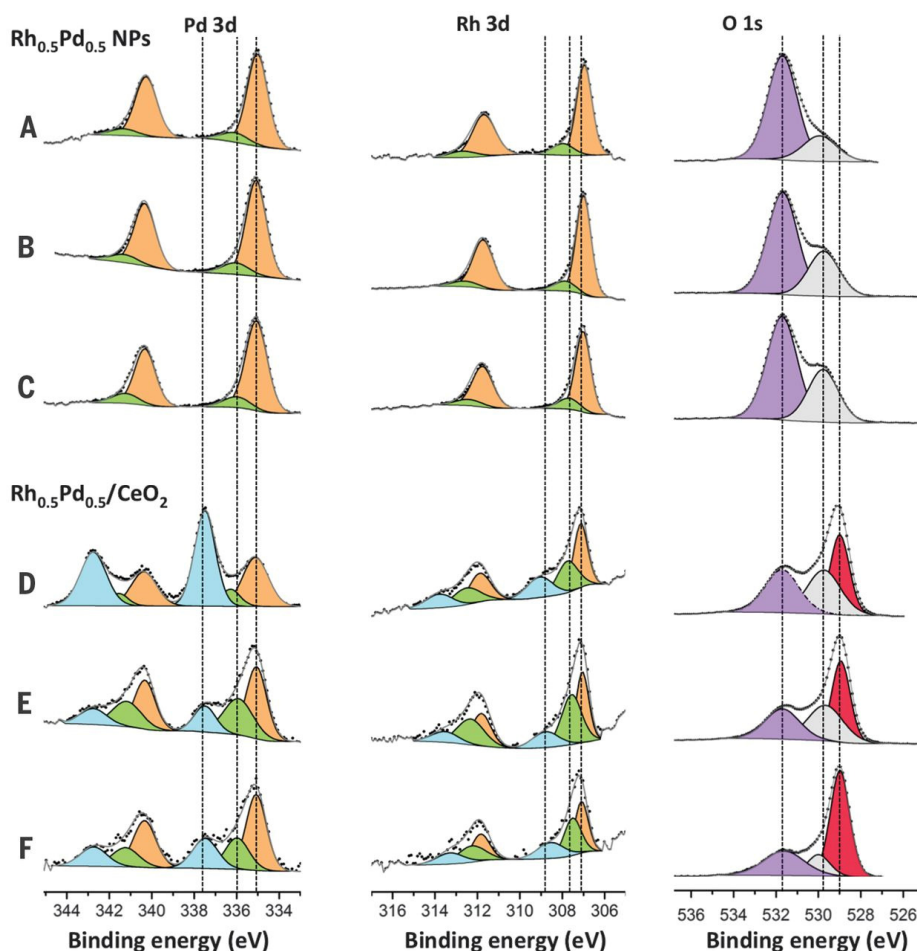

Figure 5. NAP-XPS spectra of Pd 3d, Rh 3d and O 1s recorded over model $Rh_{0.5}Pd_{0.5}$ NPs (**A** to **C**) and $Rh_{0.5}Pd_{0.5}/CeO_2$ catalyst (**D** to **F**) under steam reforming of ethanol (SRE) conditions at 823 K. The photon energies used were 670 eV (**A** and **D**), 875 eV (**B** and **E**) and 1150 eV (**C** and **F**). Reprinted with permission from [68], copyright 2014, Science.
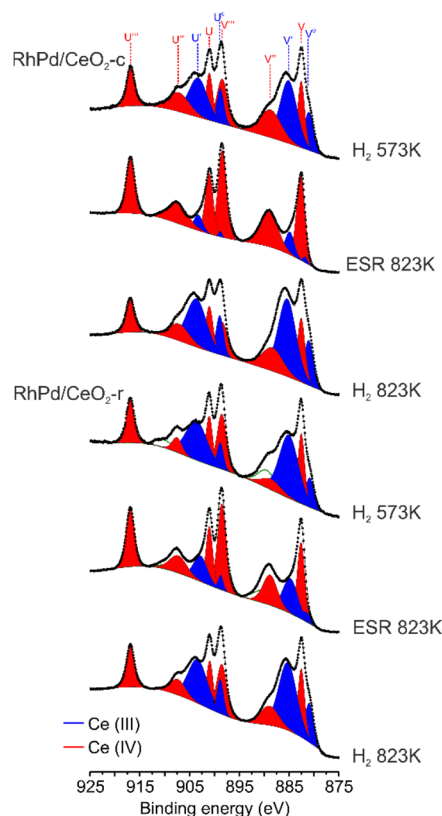
Figure 6. NAP-XPS spectra of Ce 3d corresponding to $Rh_{0.5}Pd_{0.5}/CeO_2$-c and $Rh_{0.5}Pd_{0.5}/CeO_2$-r catalysts under different gaseous atmospheres using 1150 eV of photon energy. Reprinted with permission from Ref [69], copyright 2019, American Chemical Society.

Among the alternatives to noble metal-based catalysts for SRE, cobalt supported catalysts are considered promising candidates for the reaction, since they have comparable activity with noble metals for C–C bond scission in adsorbed ethanol at moderate temperatures, but considerably low prices [276,279,284]. Óvári et al. used NAP-XPS to study the interaction of ethanol with a well-ordered $CeO_2(111)$ film evaporated over Cu(111) and with $Co/CeO_2(111)/Cu(111)$ model catalyst [150]. In this case, researchers did not investigate their systems under ethanol steam reforming conditions, but simply studied the interaction of ethanol with their catalysts to determine not only the chemical nature of transient intermediates but also the oxidation states of the surface-active components. After characterizing the evaporated $CeO_2(111)$ film on the Cu(111) surface, Óvári et al. investigated the adsorption and decomposition of ethanol on the oxide at 300 K and different pressures (10^{-6}, 10^{-4}, 0.01, 0.1 and 1 mbar). At this temperature, an increase in ethanol pressure resulted in a gradual reduction of ceria, probably via H_2O desorption involving lattice oxygen atoms. However, the reduction was hindered at pressures of 10^{-4} mbar or higher due to a reduced mobility of either oxygen or Ce^{3+} centres. Ethanol adsorption at 300 K was also detected through the recorded O 1s spectra, which at low pressures showed a shoulder at 531.5 eV usually assigned to formation of –OH groups, but also possibly originated by ethoxide and acetaldehyde surface species, expected at this binding energy too [267,285]. At higher pressures, an additional and weak contribution at 534.3 eV was detected, attributed to weakly held, molecularly adsorbed ethanol. Researchers also investigated the reaction of 0.1 mbar ethanol on bare $CeO_2(111)$ film at different temperatures (from 320 up to 600 K) before cobalt deposition. During this temperature increase, the reduction of Ce^{4+} to Ce^{3+} species raised significantly, observable through Ce 3d and O 1s spectra. The primary intermediate, ethoxide, was again detected at all temperatures (285.7 eV) and formed by dissociative adsorption of ethanol, and no coke deposition was observed up to 600 K on ceria. Upon deposition of 0.7 ML of cobalt at 300 K, partial reduction of ceria was observed, which also led to the formation of Co^{2+} sites but still leaving metallic Co in metal particles, suggested by the large

width of the main peak at Co 2p region. Since the reaction of cobalt and ceria is expected to develop mainly at the support/metal interface, the small amounts of unreacted Co^0 species are likely to be found primarily on top of Co clusters, available for interaction with ethanol. When exposing the $Co/CeO_2(111)$ model catalyst to 0.1 mbar of ethanol, Co^{2+} species decreased drastically with increasing temperature, and Co was mostly metallic at 600 K. This process was accompanied by further reduction of ceria and the formation of surface carbon deposits, which was not observed on pure ceria and contributed to the severe intensity loss in the Co 2p spectra, together with Co nanoparticles sintering.

Different cobalt-based catalyst configurations were reported by Turczyniak and co-workers [152], who investigated the effect of SRE conditions over various forms of Co (single crystal, nanoparticles, and supported on CeO_2 and ZnO) by means of ambient pressure XP and absorption spectroscopies. Systems were exposed to oxidising, reducing and SRE atmospheres, and results showed that under 0.2 mbar O_2 at 523 K, Co $2p_{3/2}$ signal and the Co L_3-edge spectra were characteristic for the Co_3O_4 spinel oxide for each cobalt configuration, while Ce 3d XP spectra exhibited typical features for bulk CeO_2. Nevertheless, under 0.2 mbar H_2 at 693 K, ceria-supported Co_3O_4 was not entirely reduced to metallic Co compared to the single crystal (Co-sc) and the nanopowdered sample, but in fact a significant amount of unreduced CoO remained on the surface. As expected, ceria partially reduced under H_2 environment, but it is worth noting that Co presence promoted the reduction of the ceria support, as compared to pure ceria. Interestingly, a gaseous mixture of ethanol and H_2O ($C_2H_5OH:H_2O$ ratio of 1:3) caused a higher reducing effect for cobalt oxides than molecular H_2, since supported Co got fully reduced to the metallic state under 0.3 mbar SRE conditions. Thus, the milder reduction conditions for Co-sc and Co nanoparticles suggested that the ceria support had a stabilization effect over supported CoO. As for the CeO_2 support, both NAP-XPS and NEXAFS results indicated slight oxidation of the oxide. Apart from the features related to the contribution of gaseous H_2O and C_2H_5OH, O 1s spectra of the systems under SRE showed additional components: the band at 531.5 eV was attributed to adsorbed –OH groups, whereas the peak located at 533.4 was correlated with molecularly adsorbed H_2O species and/or oxygenated carbon impurities. Finally, an asymmetric peak at 284.4 eV prevailed in all C 1s XP spectra, characteristic of hydrocarbon or graphitic carbon species. However, a severe difference in the amount of deposited C under SRE conditions was detected between unsupported and supported cobalt-based samples, revealing the role of mobile ceria lattice oxygen atoms in the prevention of catalyst coking. Following their work, Turczyniak et al. examined the impact of the Co/CeO_2 catalyst composition and surface oxidation state on the SRE reaction performance by combining *operando* and ex situ XPS in a wide pressure range (0.2–20 mbar) [151]. The catalyst was subjected to oxidative (O_2) or reductive (H_2 or ethanol vapour) gaseous environments before exposing it to SRE conditions. Under 0.2 mbar O_2 and 523 K, Co 2p and Ce 3d signals indicated the presence of Co_3O_4 spinel phase and bulk CeO_2, respectively. Contrarily, reducing pretreatment conditions (0.2 mbar H_2 or gaseous ethanol at 693 K) induced the complete reduction of Co to the metallic state and a partial reduction of ceria, leading to a mixture of Ce^{3+} and Ce^{4+} species with a higher Ce^{3+}/Ce^{4+} ratio under ethanol atmosphere than under hydrogen. Independent of the prior surface oxidation state under the pretreatment atmospheres, metallic Co^0 bands dominated the Co $2p_{3/2}$ photoemission spectrum during SRE conditions ($EtOH:H_2O = 1:3$ at 693 K), while the mixture of Ce^{3+} and Ce^{4+} species present under reaction conditions was influenced by the pretreatment, as indicated by the small but notable differences in the Ce 3d spectra. CO and H_2 production were favoured with this surface state, indicating that C–C bond scission is the key route in this pressure regime. The population of adsorbed hydroxyl groups increased with the degree of ceria reduction, but they surprisingly inhibited the SRE activity and the C–C bond yield. Therefore, oxidised ceria supports promoted the cleavage of C–C ethanol bond with Co keeping its metallic state.

Another example of a cobalt-based catalyst for SRE reaction is reported in the work of Sohn et al. [153], who investigated the effect of supported cobalt nanoparticles on the catalytic performance of nano-ceria (CeO_2-NP) and micro-ceria (CeO_2-MP) under ethanol steam reforming conditions, by using NAP-XPS and X-ray absorption near edge structure (XANES) techniques. Those characterization methods allowed the study of both surface and bulk properties of the samples, respectively. CeO_2-NP size varied from

2 to 10 nm, with an average size of 4 nm, while CeO_2-MP exhibited much larger particle sizes, which varied significantly from 40 to 200 nm with a mean particle size of 120 nm. Cobalt particle sizes were also different between the two Co/CeO_2 samples, with bigger Co particles observed over CeO_2-MP. Researchers found that surface reducibility was altered by the particle size of bare ceria particles, smaller ones leading to a higher surface reduction degree. The presence of completely oxidised Co nanoparticles on CeO_2-NP and CeO_2-MP hindered surface reducibility of ceria. This effect could be explained since reducing agents (such as ethanol and produced hydrogen) may be principally consumed to reduce the cobalt oxide species (Co_3O_4 and CoO), which are fully oxidised at the initial steps (He, 300 K). It could also be caused by the dissociation of H_2O molecules on the Co surface, which may spillover to the ceria support and subsequently partially oxidise its surface. Under SRE conditions and increasing temperature (623–723 K with 0.13 and 1.33 mbar of C_2H_5OH and H_2O, respectively, so as to achieve an ethanol and water mixture of 1:10 molar ratio), researchers observed an increasing degree of ceria reduction. NAP-XPS measurements indicated the presence of both metallic Co and CoO_x at the surface of cobalt nanoparticles, which actually consisted of a metallic Co-based shell and CoO_x-based core. Eventually, they found much larger differences between Co/CeO_2-NP and Co/CeO_2-MP than between bare ceria supports, which reflected the importance of metallic Co in SRE catalysis. In another work, Sohn et al. [101] examined the same catalysts (Co loaded CeO_2-NP and MP) and the focus of their study was the surface oxygen mobility and oxygen vacancy formation on their samples, which has been already reviewed in Section 3.1.

Ni-oxide based materials have also emerged as promising catalysts for the SRE reaction owing to their ability to activate C–C and C–H bonds in hydrocarbon oxygenates [280] and their activity comparable to that of expensive noble metals such as Rh, Pt and Pd [269,271]. The combination of Ni and ceria in a catalyst confers the ability to activate both ethanol (C–C and C–H bonds) and H_2O (O–H), and selectively extract hydrogen avoiding the production of CH_4 or other C–O by-products (aldehydes or olefins). Liu and colleagues [154] combined NAP-XPS and AP-IRRAS techniques to elucidate the catalytic chemistry (active phases and surface species) and the elementary steps related to the SRE reaction over Ni/CeO_2(111) model catalysts. Ceria was evaporated onto a Ru single crystal (0001) and was estimated to be ca. 4 nm thick. Ni was then deposited on the as-prepared ceria film by physical evaporation, and its coverage was estimated to be 0.15 ML. Although ceria alone is not catalytically active for the SRE process, researchers studied the chemistry of ethanol and H_2O at elevated pressures over bare CeO_2(111) before investigating the SRE reaction over Ni/CeO_2(111) catalyst. The exposure of ~ 0.05 mbar of ethanol at 300 K led to the formation of ethoxy species ($CH_3CH_2O–$) on the ceria surface, as reflected in both C 1s and O 1s regions, formed upon binding of deprotonated H to ceria lattice oxygen due to the dissociative adsorption of ethanol. After adding ~ 0.26 mbar of water into the reaction to achieve a ~ 5:1 (H_2O:EtOH) vapour mixture, an additional band appeared in the C 1s region, indicating the formation of small amounts of dioxyethylene species ($CH_3CHO_2–$). In this atmosphere, the sample was then heated from 300 to 700 K and, according to the recorded C 1s and O 1s spectra, most of the ethoxy species recombined with surface hydroxyls and gradually desorbed from the surface up to 700 K. Two additional features appeared, attributed to dioxyethylene ($CH_3CHO_2–$) and acetate ($C_2H_3OO–$) species, generated through the oxidation of ethoxy species, but no evidence of C–C bond scission was observed. As expected, bare ceria is not likely to perform the key step of the SRE reaction. Nevertheless, ceria strongly became reduced by ethanol from 500 to 700 K generating Ce^{3+} species, as well as oxygen vacancies, which in turn dissociated H_2O into hydroxyl groups and even led to the formation of cerium hydroxide compounds. The same experimental procedure was followed for the Ni/CeO_2(111) catalyst, and NAP-XPS results (see Figure 7) revealed that under SRE conditions small supported Ni nanoparticles were present as Ni^0/Ni_xC, the active phase that leads to both C–C and C–H scission of ethanol and also carbon accumulation. Concurrently, the ceria surface appeared highly reduced and hydroxylated and played an important role in the deprotonation of ethanol and water with subsequent generation of hydroxyls, which are essential intermediates to react

and remove CH_x or surface carbon. Indeed, the active phase of CeO_x was a $Ce^{3+}(OH)_x$ compound resulted from the reduction by ethanol and the efficient dissociation of H_2O.
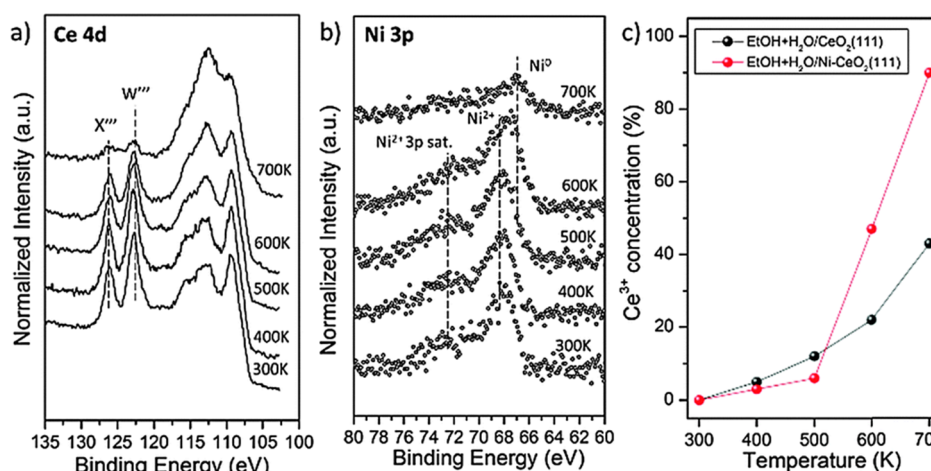

Figure 7. (**a**) Ce 4d and (**b**) Ni 3p spectra of Ni/CeO$_2$(111) surface under SRE conditions, and (**c**) surface Ce^{3+} concentration comparison between CeO$_2$(111) and Ni/CeO$_2$(111) catalysts. Reprinted with permission from [154], copyright 2016, Royal Society of Chemistry.

Despite the multiple advantages of bio-derived ethanol, as its low sulphur content and low toxicity as compared to methanol, steam reforming of methanol (SRM) has a lower activation temperature and better selectivity (less CO or coke formation) than other heavier alcohols owing to the absence of a C–C bond [286]. The most common studied catalysts for SRM are Cu-based metal-oxides because of copper's well-known capability of catalysing methanol synthesis in the industry [287–289]. Nevertheless, Cu-based catalysts possess multiple drawbacks such as their pyrophoricity and catalytic deactivation due to metal sintering. Nickel has recently been reported as a non-expensive alternative metal with favourable catalytic activity and selectivity for the SRM reaction [290,291]. In spite of being prone to deactivation due to the coke formation, Liu et al. showed that the combination of Ni with Ce is able to significantly mitigate the accumulation of surface carbon. [154]. For this reason, they recently investigated both powder (Ni/CeO$_2$) and model (Ni/CeO$_2$(111)) catalysts for SRM reaction in order to elucidate structure-reactivity correlations under reaction conditions [155]. In situ XRD and DRIFTS were used to study the active phase evolution and surface species transformation on powder catalysts, and they observed phase transitions of NiO $\rightarrow$ NiC $\rightarrow$ Ni and CeO$_2$ $\rightarrow$ CeO$_{2-x}$ during the reaction. By means of NAP-XPS, researchers first examined the interaction of methanol with an oxidised Ni/CeO$_2$(111) surface in the temperature range of 300–700 K. The formation of methoxy and hydroxyls groups at room temperature, as a result of dissociative adsorption of methanol, was detected through both O 1s and C 1s spectra. However, these contributions disappeared upon heating the surface up to 700 K, likely due to methanol desorption. With a moderate dose of methanol (2 L, L = Langmuir), no Ni reduction was detected and only a minor reduction of ceria was observed. These results indicated that a fully oxidised Ni/CeO$_2$(111) surface is catalytically inert for methanol reaction. The same measurements were performed over a reduced Ni/CeO$_{1.8}$(111) surface, which was found to behave differently. O 1s spectra showed an enhancement in the relative intensity of hydroxyl/methoxy peak (–OH/CH$_3$O–) at 300 K, resulting from the higher amount of oxygen vacancies on the oxide substrate for dissociative adsorption of methanol, but again it attenuated and finally disappeared as temperature increased to 700 K. Nevertheless, at 500 K they detected a new contribution, which was attributed to a Ni carbide (Ni$_3$C) species. Finally, another experiment was performed by heating the pre-dosed methoxy covered surface in a background of 2.66×10^{-5} bar of water, so as to check the effect of surface hydroxyl and H$_2$O. Similarly, surface C/Ni$_3$C species were formed at 500 K, but no carbon was detected on the surface upon heating to 700 K, fact that emphasized the significance of hydroxyls/water on the selectivity of SRM

and the role of metal–support interactions, that links the metal and the oxide to complete the reaction cycle and contributes to the high selectivity of the catalysts.

Methanol Oxidation

The oxidation of methanol has been proposed as a probe reaction to characterise the catalytic performance of metal oxides [292]. Depending on the products generated, catalysts have been classified as acidic, basic or redox. Acidic materials yield coupling products such as dimethyl ether, basic materials cause dehydrogenation with CO and CO_2 as products, and redox catalysts produce formaldehyde. Very recently, Mullins [156] reported the reaction of methanol with and without O_2 on a flat and highly crystalline $CeO_2(100)$ surface as a function of temperature and pressure, via ambient pressure XPS. The results indicated that, in the absence of O_2, methoxy (CH_3O–) is the prevailing surface species in both low-pressure ($\leq 1.3 \times 10^{-5}$ mbar) and high-pressure regimes (≥ 0.13 mbar). Moreover, methanol decomposition considerably reduced the ceria thin film and C_x accumulated on its surface. Upon dosing oxygen, C_x surface depositions were not observed, and the nature of the dominant surface species was dependent on the pressure. Methoxy still prevailed in the low-pressure regime, and its coverage decreased with temperature and was smaller than the coverage in the absence of O_2, which evidences the reaction between methoxy groups and the gaseous oxygen. In the high-pressure regime, surface formate $(HCOO)^-$ dominated. Therefore, the nature of surface species appeared to be related to the oxygen ability to maintain a completely oxidised ceria surface during the methanol reaction.

3.2.7. Hydrogenation Reactions

Recently, ceria has received intense interest in reactions such as hydrogenation of alkynes to alkenes [293,294]. Indeed, the interactions of H_2 with CeO_2 have long been experimentally and theoretically studied to understand the redox properties of ceria-based catalysts, as ceria oxygen vacancies are commonly formed through hydrogen reduction [295,296]. Nevertheless, there is still no direct experimental evidence for the presence of cerium hydride (Ce−H) upon hydrogen dissociation over ceria, and the mechanism of the hydrogenation reaction still remains elusive. In their work, Wu et al. [157] reported for the first time direct experimental evidence for the formation of both surface and bulk Ce−H species upon H_2 interaction with ceria nanorods by using in situ inelastic neutron scattering spectroscopy (INS). Combined with other in situ spectroscopic techniques such as IR, Raman and NAP-XPS, as well as DFT calculations, their results confirmed that hydrogen dissociates over ceria creating homolytic products (OHs) on a close-to-stoichiometric ceria surface, while heterolytic products (Ce−H and OH) result with the presence of induced oxygen vacancies in the oxide surface. NAP-XPS measurements were performed over ceria nanorods during an H_2 treatment (0.65 mbar) at different temperatures (533, 623 and 673 K) in order to monitor ceria oxidation states upon hydrogen interaction. Another investigation of ceria's hydrogenation ability, specifically C=O bond hydrogenation, was carried out on a series of CeO_2/Pt catalysts by Mueanngern and co-workers [158]. The goal of their work was to examine the scaling of catalytic activity for a support-mediated reaction pathway with respect to distance from the active metal–support interface. With this aim, researchers prepared an inverse catalyst system based on CeO_2 nanocubes supported on a Pt thin film. Langmuir-Blodgett deposition was employed to deposit the ceria nanocubes at well-controlled coverages onto the metallic film, and surface pressure was followed as a function of film compression during nanoparticle deposition. They showed that deposition of CeO_2 nanoparticles leads to two types of Pt/CeO_2 interfaces that extend over multiple length scales: firstly, a nanoscale interface defined by the contact of individual ceria nanoparticles with the Pt surface and, secondly, a larger, mesoscale interface defined by the limit between domains of self-assembled nanoparticles and the surrounding Pt support. Results indicated that almost no C=O bond hydrogenation occurred within a domain of closely spaced ceria nanoparticles. Instead, the rate of C=O bond hydrogenation was quite high at the boundary between a domain of ceria nanoparticles and the surrounding Pt substrate. Three different catalysts with CeO_2 nanoparticles at 450, 150 and 75 cm^2 compression areas were analysed by

means of NAP-XPS under approximately 0.4 mbar H_2 and a temperature range of 300−473 K, and measurements confirmed that the observed kinetics are not caused by variations in the ceria oxidation state due to H spillover or Pt decoration by the migration of reduced Ce atoms during reaction. Alternatively, they assumed that reaction kinetics were rate-limited by the surface displacement of crotyl-oxy intermediates as they form on ceria nanoparticles and consequently diffuse and react on Pt.

3.3. Gas-Solid Electrocatalysis

Nowadays, research and development of electrochemical devices such as batteries, fuel cells and supercapacitors have surged due to the demand for clean, secure and sustainable energy sources. Solid oxide electrochemical cells (SOCs) are among the most promising technologies for efficient fuel generation and electric power production. SOCs are a general class of solid-state electrochemical devices that comprise solid oxide fuel cells (SOFCs), which convert fuels and oxygen to electric power, and solid oxide electrolysis cells (SOECs) for fuel generation from electricity. Although SOCs have enormous potential for future mass H_2 production [297] and offer several attractive advantages, including high efficiency and tolerance to catalyst poisoning, reformation of hydrocarbon fuels and the possibility of burning hydrocarbon fuels directly, these devices have not yet found extensive use in quotidian applications [298]. The understanding of fundamental processes in the bulk and at the interfaces of electrochemical devices is decisive in order to develop new technologies with improved efficiency and performance.

Common electrochemical evaluations of electrode overpotential usually employ voltammetry and electrochemical impedance spectroscopy. Nevertheless, there is still a lack of direct knowledge regarding the surface chemistry and electrochemical processes that guide these systems, owing to the inherently convoluted nature of electrochemical processes and the need for suitable in situ techniques that explore these issues at relevant pressures and temperatures. Surface analytical techniques such as atomic force microscopy (AFM), scanning tunnelling microscopy (STM) and conventional UHV XPS cannot be used due to the gaseous reactant environment, high operating temperatures (> 873 K) and far-from-equilibrium conditions related with the operating devices. For this reason, new in situ and *operando* tools are being developed and already began to provide fundamental insight into SOC processes. Among them, NAP-XPS allows the resolution of local surface potentials, electrochemically active regions and shifts in surface oxidation states in operating SOCs [299–302].

Solid oxide electrochemical cells are complex devices composed of three basic components: a porous anode, an electrolyte membrane and a porous cathode. Figure 8 shows a schematic representation of the most common design of an electrolyte supported SOFC [303], in which the dense electrolyte membrane supports both electrodes. The materials typically employed in SOECs are basically similar to those used for SOFCs [304–306]. The electrolyte, usually a dense oxide-ion conductor such as yttria-stabilized zirconia (YSZ), electronically isolates the air and fuel compartments and enhances pure oxygen ion transport between the anode and the cathode. Other materials, including scandia-stabilized zirconia (ScSZ), ceria-based electrolytes (fluorite structure) or the lanthanum gallate (LSGM, perovskite structure) are also considered [298], but the high temperatures (> 923 K) required to transport oxide through the solid-state electrolyte restrict the materials that can be used as SOC components [307]. Electrodes must combine oxide-ion conduction with catalytically active electronically conducting materials, that is, exhibit mixed ionic-electronic conductivity (MIEC). For this reason, the most commonly used MIEC material for the cathode (which catalyses the oxidation of fuel in electrolysis mode) is a metal–oxide composite composed of YSZ and metallic nickel (Ni/YSZ), but alternative materials include samaria doped ceria (SDC) with dispersed Ni nanoparticles, titanate/ceria composites or the perovskite material lanthanum strontium chromium manganite (LSCM). As for the anode, lanthanum strontium manganite (LSM)/YSZ composite is the most habitually used material to date, although different materials have also been proposed.

Doped cerium oxide, $Ce_{1−x}M_xO_{2−\delta}$ (M: rare-earth or alkaline-earth cations), has received considerable interest for potential use in SOCs because of its higher ionic conductivity with respect to yttria-stabilized

zirconia and a lower cost compared with lanthanum gallate-based phases. Solid electrolytes based on doped ceria materials allow a decrease in the SOFC operation temperature due to its high oxide ion conduction, which consequently simplifies various technological issues. SOFC anode can also be based on doped ceria materials, and $Ce_{1-x}M_xO_{2-\delta}$ solid solutions (where M = Gd or Sm, and x = 0.10–0.20) exhibit the highest level of oxide ion conductivity among ceria-based ionic conductors [80,308]. Nevertheless, relatively few studies have used doped ceria materials as solid electrolyte under electrolysis mode, likely due to the partial reduction of Ce^{4+} to Ce^{3+} under operation caused by the high voltages applied, which results in electronic conduction and thus a short-circuit of the cell [298].
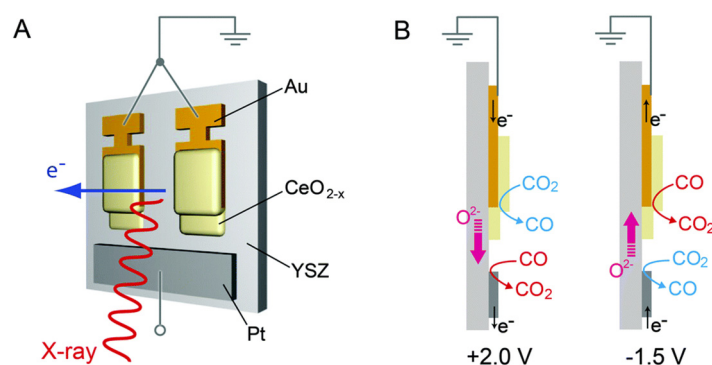

Figure 8. (**A**) Schematic setup of an electrochemical cell comprising a 300 nm Pt counter electrode (CE), a 300 nm Au current collector on top of a 50 nm alumina film (not shown) and a 350 or 1000 nm ceria working electrode (WE) patterned onto a polycrystalline yttria-stabilized zirconia (YSZ) substrate. (**B**) Schematic illustration of electrochemical reactions under positive and negative biases. Reprinted with permission from [303], copyright 2014, Royal Society of Chemistry.

Thus, in this third and last block we have gathered all reported gas-solid electrocatalytic reactions examined with the NAP-XPS technique, based on both SOFC and SOEC systems with cerium oxide as a component. Four different types of electrocatalytic reactions performed through these systems are found in literature, and Table 2 provides the list of the reports published so far.

Table 2. Published NAP-XPS investigations of ceria-based catalysts in electrocatalytic reactions.

Reaction	Catalyst	P_{max} (mbar)	T (K)	X-ray Source	Year	Ref.
H₂O electrolysis/ H₂ electro-oxidation	WE = CeO_{2-x} CE = Pt	0.66	973	Synchrotron	2009	[75]
	WE = CeO_{2-x} CE = Pt	1.06	923–1013	Synchrotron	2010	[300]
	WE = CeO_{2-x} CE = Pt	1	1023	Synchrotron	2010	[309]
	WE = CeO_2 CE = Pt	0.65	973–1023	Synchrotron	2012	[310]
	SDC [a]	1.06	739–923	Synchrotron	2012	[311]
	WE=CeO_{2-x} CE=Pt	0.65	973	Synchrotron	2013	[312]
	CeO_{2-x} and SDC	0.37	763–923	Synchrotron	2016	[313]
	Ni/GDC [b]	0.2	773–973	Synchrotron	2017	[314]
	WE = NiO/GDC CE = Pt	0.2	973	Synchrotron	2017	[315]
	WE = Ni/GDC CE = LSC [c]	0.1	923	Synchrotron	2018	[316]

<div align="center">Table 2. Cont.</div>

Reaction	Catalyst	P_{max} (mbar)	T (K)	X-ray Source	Year	Ref.
CO$_2$ electrolysis/ CO electro-oxidation	WE = CeO$_{2-x}$ CE = Pt	0.65	873	Synchrotron	2014	[303]
	WE = Ni/GDC CE = Pt	0.53	893	Synchrotron	2015	[317]
CH$_4$ electro-oxidation	WE = Ni/GDC CE = Pt	0.1	973	Synchrotron	2013	[318]

WE = working electrode, CE = counter electrode; [a] SDC = Sm$_{0.2}$Ce$_{0.8}$O$_{1.9-\delta}$; [b] GDC = Gd$_{0.1}$Ce$_{0.9}$O$_2$; [c] LSC = La$_{0.6}$Sr$_{0.4}$CoO$_{3-\delta}$.

3.3.1. H$_2$O Electrolysis/H$_2$ Electro-Oxidation

The first experiments performed with NAP-XPS in order to probe oxidation states of all exposed surfaces and local electric potentials of ceria thin film electrodes operating in SOCs are associated to DeCaluwe and co-workers [75]. The SOC cell design consisted on a 300 nm thick CeO$_{2-x}$ thin film with a patterned Au current collector as working electrode (WE) and a porous Pt counter electrode (CE), both supported on the same side of a 1 mm thick single-crystal YSZ electrolyte to enable NAP-XPS to access the electrode-electrolyte interfaces. XPS measurements were performed during electrochemical oxidation of H$_2$ and electrolysis of H$_2$O (see Equations (8) and (9), respectively) at 973 K, and results showed the extent of near-surface Ce^{4+} reduction to Ce^{3+} upon increasing cell voltage. Large negative biases caused an increase of Ce^{4+} species with respect to equilibrium values, as well as a resistance drop due to H$_2$ oxidation activity. Contrarily, the application of positive voltages drove H$_2$O electrolysis on ceria and a further increase of Ce^{3+} species. Similar findings were reported by DeCaluwe et al. [300] in another study of the same SOC cell geometry. Additional tests indicated that highly reduced ceria surface, caused by an increased H$_2$-to-H$_2$O ratio, was more active for electrolysis.

$$H_2 + O_2 \rightarrow H_2O + 2e^-, \tag{8}$$

$$H_2O + 2e^- \rightarrow H_2 + O^{2-}, \tag{9}$$

Further studies of the same SOC system (with variable ceria electrode thickness) were performed by Zhang and researchers [309,310,312] by using NAP-XPS, among other characterization tools. *Operando* spectroscopic analyses, carried out under a ~1 mbar pressure gaseous mixture of H$_2$ and H$_2$O (1:1) and at temperatures above 973 K, allowed the measurement of local surface ceria oxidation states and the detection of electrochemically active regions of ceria thin films. Results revealed that the electrochemically active regions extend 150−200 μm away from the current collectors on ceria electrodes, and the persistence of the Ce^{3+}/Ce^{4+} shifts in these regions suggested that the surface reaction kinetics and lateral electron transport on the ceria electrodes are co-limiting processes. Using a different experimental setup, Chueh and co-workers [311,313] combined ambient pressure XPS and electrochemical impedance spectroscopy to simultaneously quantify the concentration of active Ce^{3+} species on the surface and in the bulk of a Sm-doped CeO$_2$(111) film under catalytically relevant temperatures and H$_2$-H$_2$O gas mixtures. On both works, SDC thin films were grown on YSZ single crystal substrates and interdigitated Pt electrical contacts were deposited and patterned on top of the thin films. The results revealed a highly reduced and stable surface even under relatively oxidising conditions, whereas the bulk doped ceria was almost entirely Ce^{4+}. Measurements of the chemical potential of surface oxygen indicated a large deviation from the bulk values, and this entropic difference played a key role in surface Ce^{3+} stabilization. Upon comparing the surface chemical capacitance of CeO$_{2-x}$ and SDC, researchers found that Sm leads to a slight decrease of surface Ce^{3+} concentration, but a 10-fold increase of the surface capacitance. Therefore, cation substitution represents an approach to tune the surface capacitance of MIECs. Finally, Papaefthimiou et al. investigated the surface

composition and oxidation state of a Ni/GDC electrode in a SOEC cell during water electrolysis by means of ambient pressure XPS and NEXAFS spectroscopies [315]. Papaefthimiou and colleagues [314] had previously reported on the effect of a steam environment on the oxidation state and composition of Ni/GDC cermets and found that, in the mbar pressure regime and at intermediate temperature conditions, water acted as an oxidant for Ni but had a dual oxidant/reducing function for doped ceria. In their succeeding work, they showed that the oxidation state and composition of the electrode during steam electrolysis are dynamic and determined by a complex interplay between the thermo-chemical oxidation caused by water vapour and the electrochemical reduction of Ni.

Finally, Nurk et al. [316] monitored changes in the surface chemistry of a Ni/GDC WE by combining NAP-XPS and impedance spectroscopy (IS). Researchers used a dual chamber NAP-XPS measurement cell with a three-electrode configuration, which provided the possibility of measuring the WE potential against a reference Pt electrode in a well-known atmosphere and monitoring the oxygen partial pressure on the studied electrode. Changes in the surface chemistry of the Ni/GDC electrode (i.e., the evolution of Ni 3p, Ce 4d and O 1s regions) during its reduction at 923 K were monitored simultaneously with the electrochemical impedance properties of the electrode and results indicated that reduction of Ce^{4+} to Ce^{3+} species and NiO to metallic Ni occurred concurrently.

3.3.2. CH_4 Electro-Oxidation

Direct feeding of the SOFCs anode with light hydrocarbons from fossil or renewable sources appears more attractive than the use of hydrogen as a fuel. Moreover, there is a significant interest in methane-fuelled SOFCs because H_2 is mainly generated by the reforming of natural gas, mostly composed of CH_4. It is known that direct feeding with methane can lead to the accumulation of carbon onto YSZ, but incorporation of ceria (in the form of GDC) limits this deposition and also improves the cell performance. Employing the same cell configuration, which consisted on an 80 µm thick NiO/GDC thin film anode on a YSZ electrolyte and a platinum film on the reverse side that acted as the cathode electrode, Papaefthimiou et al. [318] provided experimental evidence of the active surface oxidation state and composition of the anode during methane electro-oxidation (0.1 mbar pressure) at intermediate working temperatures (973 K). A mixture of reduced Ni^0 and Ce^{3+} species in the anode, with an optimum Ni/Ce surface ratio close to 0.4, was found to be the most favourable design to achieve maximum cell currents.

3.3.3. CO_2 Electrolysis/CO Electro-Oxidation

Carbon dioxide can be used as a chemical feedstock in electrochemical systems, and this approach has become an interesting methodology for the production of hydrocarbon compounds, e.g., methane, methanol and carbon monoxide. Nevertheless, it is well-known that the activation and reduction of CO_2 to CO and oxygen is a demanding task owing to the large positive enthalpy ($\Delta H = 283.0$ kJ/mol) [319]. Recent investigations suggest that high-temperature electrolysis of CO_2 using molten carbonates and solid oxide electrolysers of CO_2 is one of the most promising and practical ways of CO_2 reduction, exhibiting faster kinetics and higher selectivity. This approach was first pursued by NASA to generate O_2 from the Martian atmosphere, rich in CO_2 [320]. Two reports of ceria-based solid oxide CO_2 electrolysis cells found in the literature study the carbon oxide chemistry (CO_2 electrolysis and CO electro-oxidation reactions) by means of ambient pressure XPS. On one hand, Yu et al. [303] designed a planar architecture SOC with both the ceria film WE and the 300 nm Pt CE patterned on the same side of the electrolyte, a polycrystalline YSZ substrate, and exposed to 0.65 mbar CO–CO_2 gas mixture at 873 K (see Figure 8). Researchers identified carbonate species (CO_3^{2-}) on the ceria surface as reaction intermediates. When CO_2 electrolysis is promoted on ceria electrodes at positively applied biases, a higher carbonate concentration over a 400 mm-wide active region on the ceria surface is observed, while CO_3^{2-} concentration appeared to decrease during CO electro-oxidation (see Figure 9).
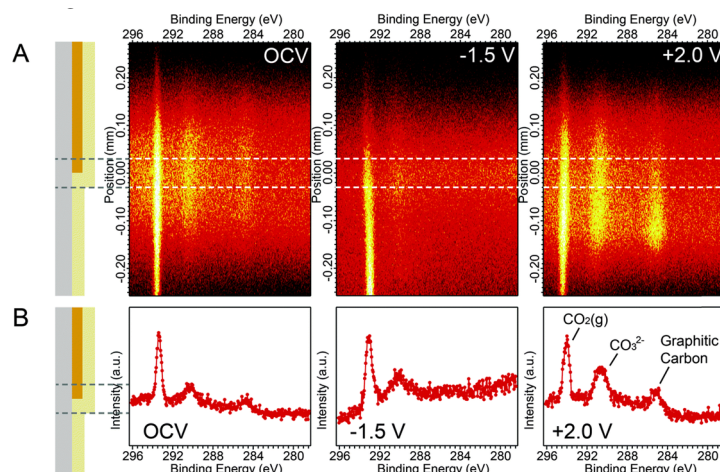
Figure 9. (**A**) Spatially-resolved NAP-XPS measurements of the C 1s obtained with a two-dimensional area detector at 0, −1.5 and +2.0 V applied potentials with 490 eV photon energy. A corresponding schematic cell drawing is given on the left. (**B**) Integrated XPS spectra obtained by slicing a 60 μm-wide segment from the corresponding photoelectron signal in (**A**) at a position of 0.0 mm. Intensities are normalised to the CO_2 gas-phase peak. Reprinted with permission from [303], copyright 2014, Royal Society of Chemistry.

These results suggest that CO_2 electrolysis reaction requires a pre-coordination of CO_2 to the ceria surface to form a CO_3^{2-} intermediate, and this reaction step precedes a rate-limiting electron transfer process involving carbonate reduction to give CO and oxide ions. This electron transfer step is also rate-limiting in the reverse direction.

On the other hand, Wang and Jackson [317] designed a two-sided electrochemical cell, with 300 nm thick Ni/GDC WE deposited onto 1 mm-thick polycrystalline YSZ substrate and a porous Pt CE on the opposing side of the support. NAP-XPS measurements of CO/CO_2 surface electrochemistry on Ni/GDC were performed on the cell at 893 K and maintaining the total pressure around 0.5 mbar, with P_{CO}/P_{CO_2} ratios at 1:1 and 1:9. Analysis demonstrated that dry CO oxidation and carbon dioxide dissociation are substantially slower than their H_2 and H_2O analogs on Ni/GDC with current densities for CO/CO_2 roughly one order of magnitude lower than H_2/H_2O. *Operando* XPS studies allowed obtaining local overpotentials and surface species factions across the Ni/GDC interface.

4. Summary and Outlook

Near ambient pressure X-ray photoelectron spectroscopy (NAP-XPS) has been demonstrated to be a powerful tool to study the surface and subsurface of ceria-based catalysts under working conditions. The excellent oxygen storage capacity and redox properties of ceria due to the ability to accommodate a large number of oxygen vacancies in its structure can be studied in detail to ultimately obtain structure-activity relationships. As a support, ceria can strongly modify the reactivity of metal nanoparticles. The unique properties of ceria to provide surface oxygen species to the metal nanoparticles and their dynamic behaviour under reaction can be conveniently studied by NAP-XPS using different photon energies in synchrotron facilities to obtain information from different depths. This is particularly attractive for following segregation phenomena under reaction conditions in bimetallic catalysts. In turn, the presence of metal nanoparticles on ceria strongly modifies the reducibility of the support. This synergy originates complex systems and the use of NAP-XPS turns to be invaluable and necessary to get information about the nature of the metal–ceria interface. Due to its capabilities, NAP-XPS is one of the most demanded tools for the study of ceria-based catalysts, both for solid–liquid and solid–gas interfaces. NAP-XPS can provide not only information on the electronic state and surface composition of ceria and metal nanoparticles supported on it under a wide range of

environmental conditions, but also information about adsorbed/desorbed molecules in the vicinity of the surface.

Abbreviations

AFM	atomic force microscopy	POX	partial oxidation
AP-IRRAS	ambient pressure IRRAS	PROX	preferential CO oxidation
CE	counter electrode	RWGS	reverse water-gas shift
CO-TPR	CO temperature-programmed reduction	ScSZ	scandia-stabilized zirconia
DFT	density-functional theory	SDC	samaria-doped ceria
DRB	dry reforming of butane	SEM	scanning electron microscopy
DRE	dry reforming of ethane	SMSI	strong metal-support interaction
DRIFTS	diffuse reflectance infrared Fourier transform spectroscopy	SOC	solid oxide electrochemical cell
DRM	dry reforming of methane	SOEC	solid oxide electrolysis cell
EXAFS	extended X-ray absorption fine structure	SOFC	solid oxide fuel cell
FT	Fischer-Tropsch	SRE	steam reforming of ethanol
GDC	gadolinium-doped ceria	SRM	steam reforming of methanol
INS	inelastic neutron scattering	STM	scanning tunnelling microscopy
IRRAS	infrared reflection absorption spectroscopy	STO	strontium titanate ($SrTiO_3$)
LB	Langmuir-Blodgett	TR-XRD	time-resolved XRD
LSCM	lanthanum strontium chromium manganite	TWC	three-way catalyst
MIEC	mixed ionic-electronic conductor	UHV	ultra-high vacuum
ML	monolayer	VOC	volatile organic compounds
MPO	methane partial oxidation	WE	working electrode
MPs	microparticles	WGS	water-gas shift
NAP-XPS	near ambient pressure XPS	XANES	X-ray absorption near edge structure
NEXAFS	near-edge X-ray absorption fine structure	XAS	X-ray absorption spectroscopy
NPs	nanoparticles	XPS	X-ray photoelectron spectroscopy
OSC	oxygen storage capacity	XRD	X-ray diffraction
OSR	oxidative steam reforming	YSZ	yttria-stabilized zirconia
PEMFC	proton-exchange membrane fuel cell	Θ	coverage

References

1. Vivier, L.; Duprez, D. Ceria-Based Solid Catalysts for Organic Chemistry. *ChemSusChem* **2010**, *3*, 654–678. [CrossRef]

2. Gorte, R.J. Ceria in Catalysis: From Automotive Applications to the Water-Gas Shift Reaction. *AICHE J.* **2010**, *56*, 1126–1135. [CrossRef]

3. Montini, T.; Melchionna, M.; Monai, M.; Fornasiero, P. Fundamentals and Catalytic Applications of CeO_2-Based Materials. *Chem. Rev.* **2016**, *116*, 5987–6041. [CrossRef] [PubMed]

4. Trovarelli, A.; Llorca, J. Ceria Catalysts at Nanoscale: How Do Crystal Shapes Shape Catalysis? *ACS Catal.* **2017**, *7*, 4716–4735. [CrossRef]

5. Wang, Q.; Yeung, K.L.; Bañares, M.A. Ceria and its related materials for VOC catalytic combustion: A review. *Catal. Today* **2019**. [CrossRef]

6. Liu, S.; Wu, X.; Weng, D.; Ran, R. Ceria-based catalysts for soot oxidation: A review. *J. Rare Earths* **2015**, *33*, 567–590. [CrossRef]

7. Aneggi, E.; Wiater, D.; De Leitenburg, C.; Llorca, J.; Trovarelli, A. Shape-Dependent Activity of Ceria in Soot Combustion. *ACS Catal.* **2014**, *4*, 172–181. [CrossRef]

8.   Mai, H.; Sun, L.; Zhang, Y.; Si, R.; Feng, W.; Zhang, H.; Liu, H.-C.; Yan, C.-H. Shape-Selective Synthesis and Oxygen Storage Behavior of Ceria Nanopolyhedra, Nanorods, and Nanocubes. *J. Phys. Chem. B* **2005**, *109*, 24380–24385. [CrossRef]

9.   Conesa, J.C. Computer modeling of surfaces and defects on cerium dioxide. *Surf. Sci.* **1995**, *339*, 337–352. [CrossRef]

10.   Huang, W.; Gao, Y. Morphology-dependent surface chemistry and catalysis of CeO_2 nanocrystals. *Catal. Sci. Technol.* **2014**, *4*, 3772–3784. [CrossRef]

11.   Wu, K.; Sun, L.; Yan, C. Recent Progress in Well-Controlled Synthesis of Ceria-Based Nanocatalysts towards Enhanced Catalytic Performance. *Adv. Energy Mater.* **2016**, *6*, 1600501. [CrossRef]

12.   Wang, Y.; Wöll, C. IR spectroscopic investigations of chemical and photochemical reactions on metal oxides: Bridging the materials gap. *Chem. Soc. Rev.* **2017**, *46*, 1875–1932. [CrossRef] [PubMed]

13.   Nolan, M.; Grigoleit, S.; Sayle, D.C.; Parker, S.C.; Watson, G.W. Density functional theory studies of the structure and electronic structure of pure and defective low index surfaces of ceria. *Surf. Sci.* **2005**, *576*, 217–229. [CrossRef]

14.   Branda, M.M.; Ferullo, R.M.; Caus, M.; Illas, F. Relative Stabilities of Low Index and Stepped CeO_2 Surfaces from Hybrid and GGA+U Implementations of Density Functional Theory. *J. Phys. Chem. C* **2011**, *115*, 3716–3721. [CrossRef]

15.   Yang, C.; Yu, X.; Heißler, S.; Nefedov, A.; Colussi, S.; Llorca, J.; Trovarelli, A.; Wang, Y.; Wöll, C. Surface Faceting and Reconstruction of Ceria Nanoparticles. *Angew. Chem. Int. Ed.* **2017**, *56*, 375–379. [CrossRef]

16.   Aneggi, E.; Rico-Perez, V.; De Leitenburg, C.; Maschio, S.; Soler, L.; Llorca, J.; Trovarelli, A. Ceria-Zirconia Particles Wrapped in a 2D Carbon Envelope: Improved Low-Temperature Oxygen Transfer and Oxidation Activity. *Angew. Chem. Int. Ed.* **2015**, *54*, 14040–14043. [CrossRef]

17.   Paier, J.; Penschke, C.; Sauer, J. Oxygen Defects and Surface Chemistry of Ceria: Quantum Chemical Studies Compared to Experiment. *Chem. Rev.* **2013**, *113*, 3949–3985. [CrossRef]

18.   Aneggi, E.; Llorca, J.; Boaro, M.; Trovarelli, A. Surface-structure sensitivity of CO oxidation over polycrystalline ceria powders. *J. Catal.* **2005**, *234*, 88–95. [CrossRef]

19.   Zhou, X.; Huebner, W. Size-induced lattice relaxation in CeO_2 nanoparticles. *Appl. Phys. Lett.* **2001**, *79*, 3512–3514. [CrossRef]

20.   Migani, A.; Vayssilov, G.N.; Bromley, S.T.; Illas, F.; Neyman, K.M. Dramatic reduction of the oxygen vacancy formation energy in ceria particles: A possible key to their remarkable reactivity at the nanoscale. *J. Mater. Chem.* **2010**, *20*, 10535–10546. [CrossRef]

21.   Bruix, A.; Neyman, K.M. Modeling Ceria-Based Nanomaterials for Catalysis and Related Applications. *Catal. Lett.* **2016**, *146*, 2053–2080. [CrossRef]

22.   Gatica, J.M.; Gómez, D.M.; Hernández-Garrido, J.C.; Calvino, J.J.; Cifredo, G.A.; Vidal, H. Experimental evidences of the relationship between reducibility and micro- and nanostructure in commercial high surface area ceria. *Appl. Catal. A Gen.* **2014**, *479*, 35–44. [CrossRef]

23.   Aneggi, E.; Llorca, J.; Trovarelli, A.; Aouine, M.; Vernoux, P. In situ environmental HRTEM discloses low temperature carbon soot oxidation by ceria-zirconia at the nanoscale. *Chem. Commun.* **2019**, *55*, 3876–3878. [CrossRef] [PubMed]

24.   Kullgren, J.; Hermansson, K.; Broqvist, P. Supercharged low-temperature oxygen storage capacity of ceria at the nanoscale. *J. Phys. Chem. Lett.* **2013**, *4*, 604–608. [CrossRef] [PubMed]

25.   Guzman, J.; Carrettin, S.; Corma, A. Spectroscopic evidence for the supply of reactive oxygen during CO oxidation catalyzed by gold supported on nanocrystalline CeO_2. *J. Am. Chem. Soc.* **2005**, *127*, 3286–3287. [CrossRef] [PubMed]

26.   Xu, J.; Harmer, J.; Li, G.; Chapman, T.; Collier, P.; Longworth, S.; Tsang, S.C. Size dependent oxygen buffering capacity of ceria nanocrystals. *Chem. Commun.* **2010**, *46*, 1887–1889. [CrossRef]

27.   Liu, X.; Zhou, K.; Wang, L.; Wang, B.; Li, Y. Oxygen Vacancy Clusters Promoting Reducibility and Activity of Ceria Nanorods. *J. Am. Chem. Soc.* **2009**, *131*, 3140–3141. [CrossRef]

28.   Wang, L.; Wang, Y.; Zhang, Y.; Yu, Y.; He, H.; Qin, X.; Wang, B. Shape dependence of nanoceria on complete catalytic oxidation of o-xylene. *Catal. Sci. Technol.* **2016**, *6*, 4840–4848. [CrossRef]

29.   Carrettin, S.; Concepción, P.; Corma, A.; López Nieto, J.M.; Puntes, V.F. Nanocrystalline CeO_2 increases the activity of Au for CO oxidation by two orders of magnitude. *Angew. Chem. Int. Ed.* **2004**, *43*, 2538–2540. [CrossRef]

30. Fu, Q.; Saltsburg, H.; Flytzani-stephanopoulos, M. Active Nonmetallic Au and Pt Species on Ceria-Based Water-Gas Shift Catalysts. *Science* **2003**, *301*, 935–939. [CrossRef] [PubMed]

31. Danielis, M.; Colussi, S.; De Leitenburg, C.; Soler, L.; Llorca, J.; Trovarelli, A. Outstanding Methane Oxidation Performance of Palladium-Embedded Ceria Catalysts Prepared by a One-Step Dry Ball-Milling Method. *Angew. Chem. Int. Ed.* **2018**, *57*, 10212–10216. [CrossRef]

32. Farmer, J.A.; Campbell, C.T. Ceria Maintains Smaller Metal Catalyst Particles by Strong Metal-Support Bonding. *Science* **2010**, *329*, 933–936. [CrossRef]

33. Jones, J.; Xiong, H.; DeLaRiva, A.T.; Peterson, E.J.; Pham, H.; Challa, S.R.; Qi, G.; Oh, S.; Wiebenga, M.H.; Hernández, X.I.P.; et al. Thermally stable single-atom platinum-on-ceria catalysts via atom trapping. *Science* **2016**, *353*, 150–154. [CrossRef] [PubMed]

34. Cargnello, M.; Doan-nguyen, V.V.T.; Gordon, T.R.; Diaz, R.E.; Stach, E.A.; Gorte, R.J.; Fornasiero, P.; Murray, C.B. Control of Metal Nanocrystal Size Reveals Metal-Support Interface Role for Ceria Catalysts. *Science* **2013**, *341*, 771–774. [CrossRef] [PubMed]

35. Rodriguez, J.A.; Grinter, D.C.; Liu, Z.; Palomino, R.M.; Senananayake, S.D. Ceria-based model catalysts: Fundamental studies on the importance of the metal-ceria interface in CO oxidation, the water-gas shift, CO_2 hydrogenation, and methane and alcohol reforming. *Chem. Soc. Rev.* **2017**, *46*, 1824–1841. [CrossRef] [PubMed]

36. Trovarelli, A. *Catalysis by Ceria and Related Materials*; Imperial College Press: London, UK, 2002.

37. Rodriguez, J.A.; Senanayake, S.D.; Stacchiola, D.; Liu, P.; Hrbek, J. The activation of gold and the water-gas shift reaction: Insights from studies with model catalysts. *Acc. Chem. Res.* **2014**, *47*, 773–782. [CrossRef]

38. Vayssilov, G.N.; Lykhach, Y.; Migani, A.; Staudt, T.; Petrova, G.P.; Tsud, N.; Skála, T.; Bruix, A.; Illas, F.; Prince, K.C.; et al. Support nanostructure boosts oxygen transfer to catalytically active platinum nanoparticles. *Nat. Mater.* **2011**, *10*, 310–315. [CrossRef]

39. Mudiyanselage, K.; Senanayake, S.D.; Feria, L.; Kundu, S.; Baber, A.E.; Graciani, J.; Vidal, A.B.; Agnoli, S.; Evans, J.; Chang, R.; et al. Importance of the metal-oxide interface in catalysis: In situ studies of the water-gas shift reaction by ambient-pressure X-ray photoelectron spectroscopy. *Angew. Chem. Int. Ed.* **2013**, *52*, 5101–5105. [CrossRef]

40. Soler, L.; Casanovas, A.; Urrich, A.; Angurell, I.; Llorca, J. CO oxidation and COPrOx over preformed Au nanoparticles supported over nanoshaped CeO_2. *Appl. Catal. B Environ.* **2016**, *197*, 47–55. [CrossRef]

41. Kim, H.Y.; Lee, H.M.; Henkelman, G. CO Oxidation Mechanism on CeO_2-Supported Au Nanoparticles. *J. Am. Chem. Soc.* **2012**, *134*, 1560–1570. [CrossRef]

42. Patarroyo, J.; Delgado, J.A.; Merkoçi, F.; Genç, A.; Sauthier, G.; Llorca, J.; Arbiol, J.; Bastus, N.G.; Godard, C.; Claver, C.; et al. Hollow PdAg-CeO_2 heterodimer nanocrystals as highly structured heterogeneous catalysts. *Sci. Rep.* **2019**, *9*, 18776. [CrossRef] [PubMed]

43. Nordling, C.; Sokolowski, E.; Siegbahn, K. Precision Method for Obtaining Absolute Values of Atomic Binding Energies. *Phys. Rev.* **1957**, *105*, 1676–1677. [CrossRef]

44. Siegbahn, K. *ESCA: Atomic, Molecular and Solid State Structure Studied by Means of Electron Spectroscopy*; Kunglia Vetenskap-Societeten Uppsala: Nova acta Regiae Societate's Uppsaliensis; Almqvist & Wiksells: Uppsala, Sweden, 1967.

45. Rupprechter, G.; Weilach, C. Spectroscopic studies of surface-gas interactions and catalyst restructuring at ambient pressure: Mind the gap! *J. Phys. Condens. Matter* **2008**, *20*, 184019. [CrossRef]

46. Somorjai, G.A.; Frei, H.; Park, J.Y. Advancing the frontiers in nanocatalysis, biointerfaces, and renewable energy conversion by innovations of surface techniques. *J. Am. Chem. Soc.* **2009**, *131*, 16589–16605. [CrossRef] [PubMed]

47. Escudero, C.; Salmeron, M. From solid-vacuum to solid-gas and solid-liquid interfaces: In situ studies of structure and dynamics under relevant conditions. *Surf. Sci.* **2013**, *607*, 2–9. [CrossRef]

48. Siegbahn, K.; Nordling, C.; Johansson, G.; Hedman, J.; Hedén, P.F.; Hamrin, K.; Gelius, U.; Bergmark, T.; Werme, L.O.; Manne, R.; et al. *ESCA Applied to Free Molecules*; North-Holland Publishing Company: Amsterdam, The Netherlands, 1969.

49. Siegbahn, H.; Siegbahn, K. ESCA applied to liquids. *J. Electron Spectros. Relat. Phenom.* **1973**, *2*, 319–325. [CrossRef]

50. Salmeron, M.; Schlögl, R. Ambient pressure photoelectron spectroscopy: A new tool for surface science and nanotechnology. *Surf. Sci. Rep.* **2008**, *63*, 169–199. [CrossRef]

51. Ogletree, D.F.; Bluhm, H.; Lebedev, G.; Fadley, C.S.; Hussain, Z.; Salmeron, M. A differentially pumped electrostatic lens system for photoemission studies in the millibar range. *Rev. Sci. Instrum.* **2002**, *73*, 3872. [CrossRef]

52. Shavorskiy, A.; Karslioglu, O.; Zegkinoglou, I.; Bluhm, H. Synchrotron-based Ambient Pressure X-ray Photoelectron Spectroscopy. *Synchrotron Radiat. News* **2014**, *27*, 14–23. [CrossRef]

53. Arble, C.; Jia, M.; Newberg, J.T. Lab-based ambient pressure X-ray photoelectron spectroscopy from past to present. *Surf. Sci. Rep.* **2018**, *73*, 37–57. [CrossRef]

54. Trotochaud, L.; Head, A.R.; Karslioğlu, O.; Kyhl, L.; Bluhm, H. Ambient pressure photoelectron spectroscopy: Practical considerations and experimental frontiers. *J. Phys. Condens. Matter* **2017**, *29*, 053002. [CrossRef]

55. Lundgren, E.; Zhang, C.; Merte, L.R.; Shipilin, M.; Blomberg, S.; Hejral, U.; Zhou, J.; Zetterberg, J.; Gustafson, J. Novel in Situ Techniques for Studies of Model Catalysts. *Acc. Chem. Res.* **2017**, *50*, 2326–2333. [CrossRef] [PubMed]

56. Dou, J.; Sun, Z.; Opalade, A.A.; Wang, N.; Fu, W.; Tao, F. Operando chemistry of catalyst surfaces during catalysis. *Chem. Soc. Rev.* **2017**, *46*, 2001–2027. [CrossRef] [PubMed]

57. Alayoglu, S.; Somorjai, G.A. Ambient Pressure X-ray Photoelectron Spectroscopy for Probing Monometallic, Bimetallic and Oxide-Metal Catalysts under Reactive Atmospheres and Catalytic Reaction Conditions. *Top. Catal.* **2016**, *59*, 420–438. [CrossRef]

58. Wu, C.H.; Eren, B.; Salmeron, M.B. Structure and Dynamics of Reactant Coadsorption on Single Crystal Model Catalysts by HP-STM and AP-XPS: A Mini Review. *Top. Catal.* **2016**, *59*, 405–419. [CrossRef]

59. Toyoshima, R.; Kondoh, H. In-situ observations of catalytic surface reactions with soft x-rays under working conditions. *J. Phys. Condens. Matter* **2015**, *27*, 83003. [CrossRef]

60. Yoshida, M.; Kondoh, H. In Situ Observation of Model Catalysts under Reaction Conditions Using X-ray Core-Level Spectroscopy. *Chem. Rec.* **2014**, *14*, 806–818. [CrossRef] [PubMed]

61. Starr, D.E.; Bluhm, H.; Liu, Z.; Knop-Gericke, A.; Hävecker, M. Application of Ambient-Pressure X-ray Photoelectron Spectroscopy for the In-situ Investigation of Heterogeneous Catalytic Reactions. In *In-situ Characterization of Heterogeneous Catalysts*; John Wiley & Sons, Inc.: Hoboken, NJ, USA, 2013; pp. 315–343.

62. Starr, D.E.; Liu, Z.; Hävecker, M.; Knop-Gericke, A.; Bluhm, H. Investigation of solid/vapor interfaces using ambient pressure X-ray photoelectron spectroscopy. *Chem. Soc. Rev.* **2013**, *42*, 5833–5857. [CrossRef]

63. Palomino, R.M.; Hamlyn, R.; Liu, Z.; Grinter, D.C.; Waluyo, I.; Rodriguez, J.A.; Senanayake, S.D. Interfaces in heterogeneous catalytic reactions: Ambient pressure XPS as a tool to unravel surface chemistry. *J. Electron. Spectros. Relat. Phenom.* **2017**, *221*, 28–43. [CrossRef]

64. Nguyen, L.; Tao, F.F.; Tang, Y.; Dou, J.; Bao, X. Understanding Catalyst Surfaces during Catalysis through Near Ambient Pressure X-ray Photoelectron Spectroscopy. *Chem. Rev.* **2019**, *119*, 6822–6905. [CrossRef]

65. Zhong, L.; Chen, D.; Zafeiratos, S. A mini review of in situ near-ambient pressure XPS studies on non-noble, late transition metal catalysts. *Catal. Sci. Technol.* **2019**, *9*, 3851–3867. [CrossRef]

66. Van Spronsen, M.A.; Frenken, J.W.; Groot, I.M. Surface science under reaction conditions: CO oxidation on Pt and Pd model catalysts. *Chem. Soc. Rev.* **2017**, *46*, 4347–4374. [CrossRef] [PubMed]

67. Tao, F.; Grass, M.E.; Zhang, Y.; Butcher, D.R.; Renzas, J.R.; Liu, Z.; Chung, J.Y.; Mun, B.S.; Salmeron, M.; Somorjai, G.A. Reaction-driven restructuring of Rh-Pd and Pt-Pd core-shell nanoparticles. *Science* **2008**, *322*, 932–934. [CrossRef]

68. Divins, N.J.; Angurell, I.; Escudero, C.; Pérez-Dieste, V.; Llorca, J. Influence of the support on surface rearrangements of bimetallic nanoparticles in real catalysts. *Science* **2014**, *346*, 620–623. [CrossRef] [PubMed]

69. Soler, L.; Casanovas, A.; Ryan, J.; Angurell, I.; Escudero, C.; Pérez-Dieste, V.; Llorca, J. Dynamic Reorganization of Bimetallic Nanoparticles under Reaction Depending on the Support Nanoshape: The Case of RhPd over Ceria Nanocubes and Nanorods under Ethanol Steam Reforming. *ACS Catal.* **2019**, *9*, 3641–3647. [CrossRef]

70. Crumlin, E.J.; Mutoro, E.; Hong, W.T.; Biegalski, M.D.; Christen, H.M.; Liu, Z.; Bluhm, H.; Shao-Horn, Y. In situ Ambient Pressure X-ray Photoelectron Spectroscopy of Cobalt Perovskite Surfaces under Cathodic Polarization at High Temperatures. *J. Phys. Chem. C* **2013**, *117*, 16087–16094. [CrossRef]

71. Knop-gericke, A.A.; Pfeifer, V.; Jones, T.; Arrigo, R.; Michael, H. In situ X-ray Photoelectron Spectroscopy of Electrochemically Active Solid-Gas and Solid-Liquid Interfaces. *J. Electron Spectros. Relat. Phenom.* **2017**, *221*, 10–17. [CrossRef]

72. Saveleva, V.A.; Savinova, E.R. Insights into electrocatalysis from ambient pressure photoelectron spectroscopy. *Curr. Opin. Electrochem.* **2019**, *17*, 79–89. [CrossRef]

73. Friebel, D.; Ogasawara, H.; Nilsson, A. X-ray Spectroscopy at Electro-catalytic Interfaces. In *Surface and Interface Science*; John Wiley & Sons, Ltd.: Hoboken, NJ, USA, 2020; pp. 733–772.

74. Starr, D.E.; Favaro, M.; Abdi, F.F.; Bluhm, H.; Crumlin, E.J.; Van de Krol, R. Combined soft and hard X-ray ambient pressure photoelectron spectroscopy studies of semiconductor/electrolyte interfaces. *J. Electron. Spectros. Relat. Phenom.* **2017**, *221*, 106–115. [CrossRef]

75. DeCaluwe, S.C.; Jackson, G.S.; Farrow, R.; McDaniel, A.; El Gabaly, F.; McCarty, K.; Nie, S.; Linne, M.; Bluhm, H.; Newberg, J.; et al. In Situ XPS for Evaluating Ceria Oxidation States in SOFC Anodes. *ECS Trans.* **2009**, *16*, 253–263.

76. Trovarelli, A. Catalytic properties of ceria and CeO_2-containing materials. *Catal. Rev.* **1996**, *38*, 439–520. [CrossRef]

77. Tauster, S.J. Strong Metal-Support Interaction. *Acc. Chem. Res.* **1987**, *20*, 389–394. [CrossRef]

78. Datye, A.K.; Kalakkad, D.S.; Yao, M.H.; Smith, D.J. Comparison of metal-support interactions in Pt/TiO_2 and Pt/CeO_2. *J. Catal.* **1995**, *155*, 148–153. [CrossRef]

79. De Leitenburg, C.; Trovarelli, A. Metal-support interactions in Rh/CeO_2, Rh/TiO_2, and Rh/Nb_2O_5 catalysts as inferred from CO_2 methanation activity. *J. Catal.* **1995**, *156*, 171–174. [CrossRef]

80. Mogensen, M.; Sammes, N.M.; Tompsett, G.A. Physical, chemical and electrochemical properties of pure and doped ceria. *Solid State Ion.* **2000**, *129*, 63–94. [CrossRef]

81. Caballero, A.; Holgado, J.P.; Gonzalez-Delacruz, V.M.; Habas, S.E.; Herranz, T.; Salmeron, M. In situ spectroscopic detection of SMSI effect in a Ni/CeO_2 system: Hydrogen-induced burial and dig out of metallic nickel. *Chem. Commun.* **2010**, *46*, 1097–1099. [CrossRef]

82. Bernardi, F.; Grass, M.E.; Hong, Y.P.; Chang, R.; Jabeen, N.; Zhang, C.; Eichhorn, B.W.; Seo, B.; Alayoglu, S.; Hussain, Z.; et al. Control of the surface atomic population of $Rh_{0.5}Pd_{0.5}$ bimetallic nanoparticles supported on CeO_2. *Catal. Today* **2016**, *260*, 95–99. [CrossRef]

83. Figueiredo, W.T.; Della Mea, G.B.; Segala, M.; Baptista, D.L.; Escudero, C.; Pérez-Dieste, V.; Bernardi, F. Understanding the Strong Metal–Support Interaction (SMSI) Effect in $Cu_x Ni_{1-x}/CeO_2$ ($0 < x <1$) Nanoparticles for Enhanced Catalysis. *ACS Appl. Nano Mater.* **2019**, *2*, 2559–2573.

84. Carrasco, J.; Lõpez-Durán, D.; Liu, Z.; Duchoň, T.; Evans, J.; Senanayake, S.D.; Crumlin, E.J.; Matolín, V.; Rodríguez, J.A.; Ganduglia-Pirovano, M.V. In situ and theoretical studies for the dissociation of water on an active Ni/CeO_2 Catalyst: Importance of strong metal-support interactions for the cleavage of O-H bonds. *Angew. Chem. Int. Ed.* **2015**, *54*, 3917–3921. [CrossRef]

85. Sharma, S.; Hu, Z.; Zhang, P.; Mcfarland, E.W.; Metiu, H. CO_2 methanation on Ru-doped ceria. *J. Catal.* **2011**, *278*, 297–309. [CrossRef]

86. Bunluesin, T.; Gorte, R.J.; Graham, G.W. Studies of the water-gas-shift reaction on ceria-supported Pt, Pd, and Rh: Implications for oxygen-storage properties. *Appl. Catal. B Environ.* **1998**, *15*, 107–114. [CrossRef]

87. Bernal, S.; Calvino, J.J.; Cauqui, M.A.; Gatica, J.M.; Larese, C.; Pérez Omil, J.A.; Pintado, J.M. Some recent results on metal/support interaction effects in NM/CeO_2 (NM: Noble metal) catalysts. *Catal. Today* **1999**, *50*, 175–206. [CrossRef]

88. Hilaire, S.; Wang, X.; Luo, T.; Gorte, R.J.; Wagner, J. A comparative study of water-gas-shift reaction over ceria supported metallic catalysts. *Appl. Catal. A Gen.* **2001**, *215*, 271–278. [CrossRef]

89. Sudarsanam, P.; Mallesham, B.; Reddy, P.S.; Großmann, D.; Grünert, W.; Reddy, B.M. Nano-Au / CeO_2 catalysts for CO oxidation: Influence of dopants (Fe, La and Zr) on the physicochemical properties and catalytic activity. *Appl. Catal. B Environ.* **2014**, *144*, 900–908. [CrossRef]

90. Aguilar-guerrero, V.; Gates, B.C. Kinetics of CO oxidation catalyzed by highly dispersed CeO_2-supported gold. *J. Catal.* **2008**, *260*, 351–357. [CrossRef]

91. Fonseca, J.; Royer, S.; Bion, N.; Pirault-Roy, L.; Do Carmo Range, M.; Duprez, D.; Epron, F. Preferential CO oxidation over nanosized gold catalysts supported on ceria and amorphous ceria-alumina. *Appl. Catal. B Environ.* **2012**, *128*, 10–20. [CrossRef]

92. Liotta, L.F.; Pantaleo, G.; Puleo, F.; Venezia, A.M. Au/CeO_2 -SBA-15 catalysts for CO oxidation: Effect of ceria loading on physic-chemical properties and catalytic performances. *Catal. Today* **2012**, *187*, 10–19. [CrossRef]

93. Russo, N.; Fino, D.; Saracco, G.; Specchia, V. Supported gold catalysts for CO oxidation. *Catal. Today* **2006**, *117*, 214–219. [CrossRef]

94. Meyer, R.; Lemire, C.; Shaikhutdinov, S.K.; Freund, H. Surface Chemistry of Catalysis by Gold. *Gold Bull.* **2004**, *37*, 72–124. [CrossRef]

95. Kang, M.; Song, M.W.; Lee, C.H. Catalytic carbon monoxide oxidation over CoO_x/CeO_2 composite catalysts. *Appl. Catal. A Gen.* **2003**, *251*, 143–156. [CrossRef]

96. Qi, X.; Flytzani-Stephanopoulos, M. Activity and stability of $Cu–CeO_2$ catalysts in high-temperature water-gas shift for fuel-cell applications. *Ind. Eng. Chem. Res.* **2004**, *43*, 3055–3062. [CrossRef]

97. Lin, L.; Yao, S.; Liu, Z.; Zhang, F.; Li, N.; Vovchok, D.; Martínez-Arias, A.; Castaneda, R.; Lin, J.; Senanayake, S.D.; et al. In Situ Characterization of Cu/CeO_2 Nanocatalysts for CO_2 Hydrogenation: Morphological Effects of Nanostructured Ceria on the Catalytic Activity. *J. Phys. Chem. C* **2018**, *122*, 12934–12943. [CrossRef]

98. Li, Y.; Fu, Q.; Flytzani-stephanopoulos, M. Low-temperature water-gas shift reaction over Cu- and Ni-loaded cerium oxide catalysts. *Appl. Catal. B Environ.* **2000**, *27*, 179–191. [CrossRef]

99. Alayoglu, S.; An, K.; Melaet, G.; Chen, S.; Bernardi, F.; Wang, L.W.; Lindeman, A.E.; Musselwhite, N.; Guo, J.; Liu, Z.; et al. Pt-mediated reversible reduction and expansion of CeO_2 in Pt nanoparticle/mesoporous CeO_2 catalyst: In situ X-ray spectroscopy and diffraction studies under redox (H_2 and O_2) atmospheres. *J. Phys. Chem. C* **2013**, *117*, 26608–26616. [CrossRef]

100. Kato, S.; Ammann, M.; Huthwelker, T.; Paun, C.; Lampimäki, M.; Lee, M.T.; Rothensteiner, M.; Van Bokhoven, J.A. Quantitative depth profiling of Ce^{3+} in Pt/CeO_2 by in situ high-energy XPS in a hydrogen atmosphere. *Phys. Chem. Chem. Phys.* **2015**, *17*, 5078–5083. [CrossRef]

101. Sohn, H.; Celik, G.; Gunduz, S.; Dogu, D.; Zhang, S.; Shan, J.; Tao, F.F.; Ozkan, U.S. Oxygen Mobility in Pre-Reduced Nano- and Macro-Ceria with Co Loading: An AP-XPS, In-Situ DRIFTS and TPR Study. *Catal. Lett.* **2017**, *147*, 2863–2876. [CrossRef]

102. Li, P.; Chen, X.; Li, Y.; Schwank, J.W. A review on oxygen storage capacity of CeO_2 -based materials: Influence factors, measurement techniques, and applications in reactions related to catalytic automotive emissions control. *Catal. Today* **2019**, *327*, 90–115. [CrossRef]

103. Singh, P.; Hegde, M.S.; Gopalakrishnan, J. $Ce_{2/3}Cr_{1/3}O_{2+y}$: A new oxygen storage material based on the fluorite structure. *Chem. Mater.* **2008**, *20*, 7268–7273. [CrossRef]

104. Deng, C.; Li, M.; Qian, J.; Hu, Q.; Huang, M.; Lin, Q.; Ruan, Y.; Dong, L.; Li, B.; Fan, M. A Study of Different Doped Metal Cations on the Physicochemical Properties and Catalytic Activities of $Ce_{20}M_1O_x$ (M = Zr, Cr, Mn, Fe, Co, Sn) Composite Oxides for Nitric Oxide Reduction by Carbon Monoxide. *Chem. An. Asian J.* **2016**, *11*, 2144–2156. [CrossRef]

105. Jampaiah, D.; Venkataswamy, P.; Coyle, V.E.; Reddy, B.M.; Bhargava, S.K. Low-temperature CO oxidation over manganese, cobalt, and nickel doped CeO_2 nanorods. *RSC Adv.* **2016**, *6*, 80541–80548. [CrossRef]

106. Lee, K.J.; Kim, Y.; Lee, J.H.; Cho, S.J.; Kwak, J.H.; Moon, H.R. Facile Synthesis and Characterization of Nanostructured Transition Metal/Ceria Solid Solutions ($TM_xCe_{1-x}O_{2-\delta}$, TM = Mn, Ni, Co, or Fe) for CO Oxidation. *Chem. Mater.* **2017**, *29*, 2874–2882. [CrossRef]

107. Beckers, J.; Rothenberg, G. Redox properties of doped and supported copper-ceria catalysts. *Dalt. Trans.* **2008**, 6573–6578. [CrossRef] [PubMed]

108. Xiong, Y.; Li, L.; Zhang, L.; Cao, Y.; Yu, S.; Tang, C.; Dong, L. Migration of copper species in $Ce_xCu_{1-x}O_2$ catalyst driven by thermal treatment and the effect on CO oxidation. *Phys. Chem. Chem. Phys.* **2017**, *19*, 21840–21847. [CrossRef] [PubMed]

109. Colón, G.; Pijolat, M.; Valdivieso, F.; Vidal, H.; Kašpar, J.; Finocchio, E.; Daturi, M.; Bernal, M.; Pijolat, F.; Valdivieso, H.; et al. Surface and structural characterization of $Ce_xZr_{1-x}O_2$ CEZIRENCAT mixed oxides as potential three-way catalyst promoters. *J. Chem. Soc. Faraday Trans.* **1998**, *94*, 3717–3726. [CrossRef]

110. Finocchio, E.; Daturi, M.; Binet, C.; Lavalley, J.C.; Flly, F.; Perrichon, V.; Vidal, H.; Kaspar, J.; Graziani, M.; Blanchard, G. Oxygen storage capacity improvement using CeO_2-ZrO_2 mixed oxides in three way catalysts. In *Science and Technology in Catalysis 1998*; Hattori, H., Otsuka, K., Eds.; Studies in Surface Science and Catalysis; Elsevier: Amsterdam, The Netherlands, 1999; Volume 121, pp. 257–262.

111. Daturi, M.; Finocchio, E.; Binet, C.; Lavalley, J.C.; Fally, F.; Perrichon, V. Study of Bulk and Surface Reduction by Hydrogen of $Ce_xZr_{1-x}O_2$ Mixed Oxides Followed by FTIR Spectroscopy and Magnetic Balance. *J. Phys. Chem. B* **1999**, *103*, 4884–4891. [CrossRef]

112. Wang, Y.; Liang, S.; Cao, A.; Thompson, R.L.; Veser, G. Au-mixed lanthanum/cerium oxide catalysts for water gas shift. *Appl. Catal. B Environ.* **2010**, *99*, 89–95. [CrossRef]

113. Liang, S.; Broitman, E.; Wang, Y.; Cao, A.; Veser, G. Highly stable, mesoporous mixed lanthanum-cerium oxides with tailored structure and reducibility. *J. Mater. Sci.* **2011**, *46*, 2928–2937. [CrossRef]

114. Orge, C.A.; Órfão, J.J.M.; Pereira, M.F.R.; Duarte de Farias, A.M.; Fraga, M.A. Ceria and cerium-based mixed oxides as ozonation catalysts. *Chem. Eng. J.* **2012**, *200–202*, 499–505. [CrossRef]

115. Singh, P.; Hegde, M.S. $Ce_{1-x}Ru_xO_{2-\delta}$ (x = 0.05, 0.10): A new high oxygen storage material and Pt, Pd-free three-way catalyst. *Chem. Mater.* **2009**, *21*, 3337–3345. [CrossRef]

116. Gayen, A.; Priolkar, K.R.; Sarode, P.R.; Jayaram, V.; Hegde, M.S.; Subbanna, G.N.; Emura, S. $Ce_{1-x}Rh_xO_{2-\delta}$ solid solution formation in combustion-synthesized Rh/CeO_2 catalyst studied by XRD, TEM, XPS, and EXAFS. *Chem. Mater.* **2004**, *16*, 2317–2328. [CrossRef]

117. Kurnatowska, M.; Schuster, M.E.; Mista, W.; Kepinski, L. Self-regenerative property of nanocrystalline $Ce_{0.89}M_{0.11}O_{2-y}$ (M = Pd, Rh) mixed oxides. *ChemCatChem* **2014**, *6*, 3125–3131. [CrossRef]

118. Hiley, C.I.; Fisher, J.M.; Thompsett, D.; Kashtiban, R.J.; Sloan, J.; Walton, R.I. Incorporation of square-planar Pd^{2+} in fluorite CeO_2: Hydrothermal preparation, local structure, redox properties and stability. *J. Mater. Chem. A* **2015**, *3*, 13072–13079. [CrossRef]

119. Hegde, M.S.; Bera, P. Noble metal ion substituted CeO_2 catalysts: Electronic interaction between noble metal ions and CeO_2 lattice. *Catal. Today* **2015**, *253*, 40–50. [CrossRef]

120. Ikemoto, S.; Huang, X.; Muratsugu, S.; Nagase, S.; Koitaya, T.; Matsui, H.; Yokota, G.; Sudoh, T.; Hashimoto, A.; Tan, Y.; et al. Reversible low-temperature redox activity and selective oxidation catalysis derived from the concerted activation of multiple metal species on Cr and Rh-incorporated ceria catalysts. *Phys. Chem. Chem. Phys.* **2019**, *21*, 20868–20877. [CrossRef] [PubMed]

121. Della Mea, G.B.; Matte, L.P.; Thill, A.S.; Lobato, F.O.; Benvenutti, E.V.; Arenas, L.T.; Jürgensen, A.; Hergenröder, R.; Poletto, F.; Bernardi, F. Tuning the oxygen vacancy population of cerium oxide (CeO_{2-x}, 0 < x <0.5) nanoparticles. *Appl. Surf. Sci.* **2017**, *422*, 1102–1112.

122. Pereira-Hernández, X.I.; DeLaRiva, A.; Muravev, V.; Kunwar, D.; Xiong, H.; Sudduth, B.; Engelhard, M.; Kovarik, L.; Hensen, E.J.M.; Wang, Y.; et al. Tuning $Pt-CeO_2$ interactions by high-temperature vapor-phase synthesis for improved reducibility of lattice oxygen. *Nat. Commun.* **2019**, *10*, 1–10. [CrossRef]

123. Sayle, T.X.T.; Caddeo, F.; Zhang, X.; Sakthivel, T.; Das, S.; Seal, S.; Ptasinska, S.; Sayle, D.C. Structure-Activity Map of Ceria Nanoparticles, Nanocubes, and Mesoporous Architectures. *Chem. Mater.* **2016**, *28*, 7287–7295. [CrossRef]

124. Gopal, C.B.; García-Melchor, M.; Lee, S.C.; Shi, Y.; Shavorskiy, A.; Monti, M.; Guan, Z.; Sinclair, R.; Bluhm, H.; Vojvodic, A.; et al. Equilibrium oxygen storage capacity of ultrathin $CeO_{2-\delta}$ depends non-monotonically on large biaxial strain. *Nat. Commun.* **2017**, *8*, 1–12.

125. Bluhm, H.; Hävecker, M.; Knop-gericke, A.; Kiskinova, M.; Schlögl, R.; Salmeron, M. In Situ X-Ray Photoelectron Studies of Gas – Solid Interfaces at Near- Ambient Conditions. *MRS Bull.* **2007**, *32*, 1022–1030. [CrossRef]

126. Pozdnyakova, O.; Teschner, D.; Wootsch, A.; Kröhnert, J.; Steinhauer, B.; Sauer, H.; Toth, L.; Jentoft, F.C.; Knop-Gericke, A.; Paál, Z.; et al. Preferential CO oxidation in hydrogen (PROX) on ceria-supported catalysts, part I: Oxidation state and surface species on Pt/CeO_2 under reaction conditions. *J. Catal.* **2006**, *237*, 1–16. [CrossRef]

127. Pozdnyakova, O.; Teschner, D.; Wootsch, A.; Kröhnert, J.; Steinhauer, B.; Sauer, H.; Toth, L.; Jentoft, F.C.; Knop-Gericke, A.; Paál, Z.; et al. Preferential CO oxidation in hydrogen (PROX) on ceria-supported catalysts, part II: Oxidation states and surface species on Pd/CeO_2 under reaction conditions, suggested reaction mechanism. *J. Catal.* **2006**, *237*, 17–28. [CrossRef]

128. Teschner, D.; Wootsch, A.; Pozdnyakova-Tellinger, O.; Kröhnert, J.; Vass, E.M.; Hävecker, M.; Zafeiratos, S.; Schnörch, P.; Jentoft, P.C.; Knop-Gericke, A.; et al. Partial pressure dependent in situ spectroscopic study on the preferential CO oxidation in hydrogen (PROX) over Pt/ceria catalysts. *J. Catal.* **2007**, *249*, 318–327. [CrossRef]

129. Holgado, J.P.; Ternero, F.; Gonzalez-Delacruz, V.M.; Caballero, A. Promotional effect of the base metal on bimetallic $Au-Ni/CeO_2$ catalysts prepared from core-shell nanoparticles. *ACS Catal.* **2013**, *3*, 2169–2180. [CrossRef]

130. Monte, M.; Munuera, G.; Costa, D.; Conesa, J.C.; Martínez-Arias, A. Near-ambient XPS characterization of interfacial copper species in ceria-supported copper catalysts. *Phys. Chem. Chem. Phys.* **2015**, *17*, 29995–30004. [CrossRef]

131.　Lukashuk, L.; Föttinger, K.; Kolar, E.; Rameshan, C.; Teschner, D.; Hävecker, M.; Knop-Gericke, A.; Yigit, N.; Li, H.; McDermott, E.; et al. Operando XAS and NAP-XPS studies of preferential CO oxidation on Co_3O_4 and CeO_2-Co_3O_4 catalysts. *J. Catal.* **2016**, *344*, 1–15. [CrossRef]

132.　Artiglia, L.; Orlando, F.; Roy, K.; Kopelent, R.; Safonova, O.; Nachtegaal, M.; Huthwelker, T.; Van Bokhoven, J.A. Introducing Time Resolution to Detect Ce^{3+} Catalytically Active Sites at the Pt/CeO_2 Interface through Ambient Pressure X-ray Photoelectron Spectroscopy. *J. Phys. Chem. Lett.* **2017**, *8*, 102–108. [CrossRef]

133.　Wen, C.; Zhu, Y.; Ye, Y.; Zhang, S.; Cheng, F.; Liu, Y.; Wang, P.; Tao, F. Water-gas shift reaction on metal nanoclusters encapsulated in mesoporous ceria studied with ambient-pressure X-ray photoelectron spectroscopy. *ACS Nano* **2012**, *6*, 9305–9313. [CrossRef]

134.　Cámara, A.L.; Monte, M.; Martínez-Arias, A.; Conesa, J.C. XPS and DRIFTS operando studies of an inverse CeO_2/CuO WGS catalyst: Deactivating role of interfacial carbonates in redox activity. *Catal. Sci. Technol.* **2012**, *2*, 2436–2439. [CrossRef]

135.　Soler, L.; Casanovas, A.; Escudero, C.; Pérez-Dieste, V.; Aneggi, E.; Trovarelli, A.; Llorca, J. Ambient Pressure Photoemission Spectroscopy Reveals the Mechanism of Carbon Soot Oxidation in Ceria-Based Catalysts. *ChemCatChem* **2016**, *8*, 2748–2751. [CrossRef]

136.　Graciani, J.; Mudiyanselage, K.; Xu, F.; Baber, A.E.; Evans, J.; Senanayake, S.D.; Stacchiola, D.J.; Liu, P.; Hrbek, J.; Fernández-Sanz, J.; et al. Highly active copper-ceria and copper-ceria-titania catalysts for methanol synthesis from CO2. *Science* **2014**, *345*, 2–6. [CrossRef]

137.　Senanayake, S.D.; Ramírez, P.J.; Waluyo, I.; Kundu, S.; Mudiyanselage, K.; Liu, Z.; Liu, Z.; Axnanda, S.; Stacchiola, D.J.; Evans, J.; et al. Hydrogenation of CO_2 to Methanol on $CeO_x/Cu(111)$ and $ZnO/Cu(111)$ Catalysts: Role of the Metal-Oxide Interface and Importance of Ce^{3+} Sites. *J. Phys. Chem. C* **2016**, *120*, 1778–1784. [CrossRef]

138.　Winter, L.R.; Chen, R.; Chen, X.; Chang, K.; Liu, Z.; Senanayake, S.D.; Ebrahim, A.M.; Chen, J.G. Elucidating the roles of metallic Ni and oxygen vacancies in CO_2 hydrogenation over Ni/CeO_2 using isotope exchange and in situ measurements. *Appl. Catal. B Environ.* **2019**, *245*, 360–366. [CrossRef]

139.　Zhu, Y.; Zhang, S.; Shan, J.J.; Nguyen, L.; Zhan, S.; Gu, X.; Tao, F. In situ surface chemistries and catalytic performances of ceria doped with palladium, platinum, and rhodium in methane partial oxidation for the production of syngas. *ACS Catal.* **2013**, *3*, 2627–2639. [CrossRef]

140.　Dou, J.; Tang, Y.; Nie, L.; Andolina, C.M.; Zhang, X.; House, S.; Li, Y.; Yang, J.; Tao, F. (Feng) Complete Oxidation of Methane on Co_3O_4/CeO_2 Nanocomposite: A Synergic Effect. *Catal. Today* **2018**, *311*, 48–55. [CrossRef]

141.　Zhang, X.; House, S.D.; Tang, Y.; Nguyen, L.; Li, Y.; Opalade, A.A.; Yang, J.C.; Sun, Z.; Tao, F.F. Complete Oxidation of Methane on NiO Nanoclusters Supported on CeO_2 Nanorods through Synergistic Effect. *ACS Sustain. Chem. Eng.* **2018**, *6*, 6467–6477. [CrossRef]

142.　Gonzalez-DelaCruz, V.M.; Holgado, J.P.; Pereñíguez, R.; Caballero, A. Morphology changes induced by strong metal-support interaction on a Ni-ceria catalytic system. *J. Catal.* **2008**, *257*, 307–314. [CrossRef]

143.　Liu, Z.; Grinter, D.C.; Lustemberg, P.G.; Nguyen-Phan, T.D.; Zhou, Y.; Luo, S.; Waluyo, I.; Crumlin, E.J.; Stacchiola, D.J.; Zhou, J.; et al. Dry Reforming of Methane on a Highly-Active $Ni-CeO_2$ Catalyst: Effects of Metal-Support Interactions on C-H Bond Breaking. *Angew. Chem. Int. Ed.* **2016**, *55*, 7455–7459. [CrossRef]

144.　Lustemberg, P.G.; Ramírez, P.J.; Liu, Z.; Gutiérrez, R.A.; Grinter, D.G.; Carrasco, J.; Senanayake, S.D.; Rodriguez, J.A.; Ganduglia-Pirovano, M.V. Room-Temperature Activation of Methane and Dry Re-forming with CO_2 on $Ni-CeO_2(111)$ Surfaces: Effect of Ce^{3+} Sites and Metal-Support Interactions on C-H Bond Cleavage. *ACS Catal.* **2016**, *6*, 8184–8191. [CrossRef]

145.　Yan, B.; Yang, X.; Yao, S.; Wan, J.; Myint, M.N.Z.; Gomez, E.; Xie, Z.; Kattel, S.; Xu, W.; Chen, J.G. Dry Reforming of Ethane and Butane with CO_2 over $PtNi/CeO_2$ Bimetallic Catalysts. *ACS Catal.* **2016**, *6*, 7283–7292. [CrossRef]

146.　Liu, Z.; Lustemberg, P.; Gutiérrez, R.A.; Carey, J.J.; Palomino, R.M.; Vorokhta, M.; Grinter, D.C.; Ramírez, P.J.; Matolín, V.; Nolan, M.; et al. In Situ Investigation of Methane Dry Reforming on Metal/Ceria(111) Surfaces: Metal-Support Interactions and C−H Bond Activation at Low Temperature. *Angew. Chem. Int. Ed.* **2017**, *56*, 13041–13046. [CrossRef]

147.　Zhang, F.; Liu, Z.; Zhang, S.; Akter, N.; Palomino, R.M.; Vovchok, D.; Orozco, I.; Salazar, D.; Rodriguez, J.A.; Llorca, J.; et al. In Situ Elucidation of the Active State of Co-CeO_x Catalysts in the Dry Reforming of Methane:

The Important Role of the Reducible Oxide Support and Interactions with Cobalt. *ACS Catal.* **2018**, *8*, 3550–3560. [CrossRef]

148. Xie, Z.; Yan, B.; Kattel, S.; Lee, J.H.; Yao, S.; Wu, Q.; Rui, N.; Gomez, E.; Liu, Z.; Xu, W.; et al. Dry reforming of methane over CeO_2-supported Pt-Co catalysts with enhanced activity. *Appl. Catal. B Environ.* **2018**, *236*, 280–293. [CrossRef]

149. Liu, Z.; Zhang, F.; Rui, N.; Li, X.; Lin, L.; Betancourt, L.E.; Su, D.; Xu, W.; Cen, J.; Attenkofer, K.; et al. Highly Active Ceria-Supported Ru Catalyst for the Dry Reforming of Methane: In Situ Identification of $Ru^{\delta+}$-Ce^{3+} Interactions for Enhanced Conversion. *ACS Catal.* **2019**, *9*, 3349–3359. [CrossRef]

150. Óvári, L.; Krick Calderon, S.; Lykhach, Y.; Libuda, J.; Erdohelyi, A.; Papp, C.; Kiss, J.; Steinrück, H.P. Near ambient pressure XPS investigation of the interaction of ethanol with $Co/CeO_2(1\ 1\ 1)$. *J. Catal.* **2013**, *307*, 132–139. [CrossRef]

151. Turczyniak, S.; Teschner, D.; Machocki, A.; Zafeiratos, S. Effect of the surface state on the catalytic performance of a Co/CeO_2 ethanol steam-reforming catalyst. *J. Catal.* **2016**, *340*, 321–330. [CrossRef]

152. Turczyniak, S.; Luo, W.; Papaefthimiou, V.; Ramgir, N.S.; Haevecker, M.; MacHocki, A.; Zafeiratos, S. A Comparative Ambient Pressure X-ray Photoelectron and Absorption Spectroscopy Study of Various Cobalt-Based Catalysts in Reactive Atmospheres. *Top. Catal.* **2016**, *59*, 532–542. [CrossRef]

153. Sohn, H.; Soykal, I.I.; Zhang, S.; Shan, J.; Tao, F.; Miller, J.T.; Ozkan, U.S. Effect of cobalt on reduction characteristics of ceria under ethanol steam reforming conditions: AP-XPS and XANES studies. *J. Phys. Chem. C* **2016**, *120*, 14631–14642. [CrossRef]

154. Liu, Z.; Duchoň, T.; Wang, H.; Grinter, D.C.; Waluyo, I.; Zhou, J.; Liu, Q.; Jeong, B.; Crumlin, E.J.; Matolín, V.; et al. Ambient pressure XPS and IRRAS investigation of ethanol steam reforming on $Ni-CeO_2(111)$ catalysts: An in situ study of C-C and O-H bond scission. *Phys. Chem. Chem. Phys.* **2016**, *18*, 16621–16628. [CrossRef]

155. Liu, Z.; Yao, S.; Johnston-Peck, A.; Xu, W.; Rodriguez, J.A.; Senanayake, S.D. Methanol steam reforming over $Ni-CeO_2$ model and powder catalysts: Pathways to high stability and selectivity for H_2/CO_2 production. *Catal. Today* **2018**, *311*, 74–80. [CrossRef]

156. Mullins, D.R. Variations in the surface chemistry of methanol with $CeO_2(100)$ at low and elevated pressures. *Surf. Interface Anal.* **2018**, *50*, 913–920. [CrossRef]

157. Wu, Z.; Cheng, Y.; Tao, F.; Daemen, L.; Foo, G.S.; Nguyen, L.; Zhang, X.; Beste, A.; Ramirez-Cuesta, A.J. Direct Neutron Spectroscopy Observation of Cerium Hydride Species on a Cerium Oxide Catalyst. *J. Am. Chem. Soc.* **2017**, *139*, 9721–9727. [CrossRef] [PubMed]

158. Mueanngern, Y.; Yang, X.; Tang, Y.; Tao, F.; Baker, L.R. Catalysis at Multiple Length Scales: Crotonaldehyde Hydrogenation at Nanoscale and Mesoscale Interfaces in Platinum-Cerium Oxide Catalysts. *J. Phys. Chem. C* **2017**, *121*, 13765–13776. [CrossRef]

159. Armor, J.N. The multiple roles for catalysis in the production of H_2. *Appl. Catal. A Gen.* **1999**, *176*, 159–176. [CrossRef]

160. Dudfield, C.D.; Chen, R.; Adcock, P.L. A carbon monoxide PROX reactor for PEM fuel cell automotive application. *Int. J. Hydrog. Energy* **2001**, *26*, 763–775. [CrossRef]

161. Kahlich, M.J.; Gasteiger, H.A.; Behm, R.J. Kinetics of the selective low-temperature oxidation of CO in H_2-rich gas over Au/α-Fe_2O_3. *J. Catal.* **1999**, *182*, 430–440. [CrossRef]

162. Schubert, M.M.; Kahlich, M.J.; Gasteiger, H.A.; Behm, R.J. Correlation between CO surface coverage and selectivity/kinetics for the preferential CO oxidation over Pt/γ-Al_2O_3 and Au/α-Fe_2O_3: An in-situ DRIFTS study. *J. Power Sources* **1999**, *84*, 175–182. [CrossRef]

163. Bethke, G.K.; Kung, H.H. Selective CO oxidation in a hydrogen-rich stream over Au/γ-Al_2O_3 catalysts. *Appl. Catal. A Gen.* **2000**, *194–195*, 43–53. [CrossRef]

164. Avgouropoulos, G.; Ioannides, T.; Papadopoulou, C.; Batista, J.; Hocevar, S.; Matralis, H.K. A comparative study of Pt/γ-Al_2O_3, Au/α-Fe_2O_3 and $CuO-CeO_2$ catalysts for the selective oxidation of carbon monoxide in excess hydrogen. *Catal. Today* **2002**, *75*, 157–167. [CrossRef]

165. Oh, S.H.; Sinkevitch, R.M. Carbon Monoxide Removal from Hydrogen-Rich Fuel Cell Feedstreams by Selective Catalytic Oxidation. *J. Catal.* **1993**, *142*, 254–262. [CrossRef]

166. Kahlich, M.J.; Gasteiger, H.A.; Behm, R.J. Kinetics of the Selective CO Oxidation in H_2-Rich Gas on Pt/Al_2O_3. *J. Catal.* **1997**, *171*, 93–105. [CrossRef]

167. Özkara, Ş.; Aksoylu, A.E. Selective low temperature carbon monoxide oxidation in H$_2$-rich gas streams over activated carbon supported catalysts. *Appl. Catal. A Gen.* **2003**, *251*, 75–83. [CrossRef]

168. Han, Y.-F.; Kahlich, M.J.; Kinne, M.; Behm, R.J. Kinetic study of selective CO oxidation in H$_2$-rich gas on a Ru/γ-Al$_2$O$_3$ catalyst. *Phys. Chem. Chem. Phys.* **2002**, *4*, 389–397. [CrossRef]

169. Jacobs, G.; Williams, L.; Graham, U.; Sparks, D.; Davis, B.H. Low-Temperature Water-Gas Shift: In-Situ DRIFTS−Reaction Study of a Pt/CeO$_2$ Catalyst for Fuel Cell Reformer Applications. *J. Phys. Chem. B* **2003**, *107*, 10398–10404. [CrossRef]

170. Johansson, S.; Österlund, L.; Kasemo, B. CO Oxidation Bistability Diagrams for Pt/CeO$_x$ and Pt/SiO$_2$ Model Catalysts Prepared by Electron-Beam Lithography. *J. Catal.* **2001**, *201*, 275–285. [CrossRef]

171. Bunluesin, T.; Cordatos, H.; Gorte, R.J. Study of CO Oxidation Kinetics on Rh/Ceria. *J. Catal.* **1995**, *157*, 222–226. [CrossRef]

172. Bekyarova, E.; Fornasiero, P.; Kašpar, J.; Graziani, M. CO oxidation on Pd/CeO$_2$–ZrO$_2$ catalysts. *Catal. Today* **1998**, *45*, 179–183. [CrossRef]

173. Kaspar, J.; Fornasiero, P.; Graziani, M. Use of CeO$_2$ -based oxides in the three-way catalysis. *Catal. Today* **1999**, *50*, 285–298. [CrossRef]

174. Kopelent, R.; Van Bokhoven, J.A.; Szlachetko, J.; Edebeli, J.; Paun, C.; Nachtegaal, M.; Safonova, O. V Catalytically Active and Spectator Ce^{3+} in Ceria-Supported Metal Catalysts. *Angew. Chem. Int. Ed.* **2015**, *54*, 8728–8731. [CrossRef]

175. Penkala, B.; Aubert, D.; Kaper, H.; Tardivat, C.; Conder, K.; Paulus, W. The role of lattice oxygen in CO oxidation over Ce^{18}O$_2$-based catalysts revealed under operando conditions. *Catal. Sci. Technol.* **2015**, *5*, 4839–4848. [CrossRef]

176. Wang, X.; Rodriguez, J.A.; Hanson, J.C.; Gamarra, D.; Martínez-Arias, A.; Fernández-García, M. In Situ Studies of the Active Sites for the Water Gas Shift Reaction over Cu-CeO$_2$ Catalysts: Complex Interaction between Metallic Copper and Oxygen Vacancies of Ceria. *J. Phys. Chem. B* **2006**, *110*, 428–434. [CrossRef]

177. Gamarra, D.; Belver, C.; Fernández-García, M.; Martínez-Arias, A. Selective CO Oxidation in Excess H$_2$ over Copper−Ceria Catalysts: Identification of Active Entities/Species. *J. Am. Chem. Soc.* **2007**, *129*, 12064–12065. [CrossRef] [PubMed]

178. Jia, A.-P.; Jiang, S.-Y.; Lu, J.-Q.; Luo, M.-F. Study of Catalytic Activity at the CuO−CeO$_2$ Interface for CO Oxidation. *J. Phys. Chem. C* **2010**, *114*, 21605–21610. [CrossRef]

179. Gamarra, D.; Cámara, A.L.; Monte, M.; Rasmussen, S.B.; Chinchilla, L.E.; Hungría, A.B.; Munuera, G.; Gyorffy, N.; Schay, Z.; Corberán, V.C.; et al. Preferential oxidation of CO in excess H$_2$ over CuO/CeO$_2$ catalysts: Characterization and performance as a function of the exposed face present in the CeO$_2$ support. *Appl. Catal. B Environ.* **2013**, *130–131*, 224–238. [CrossRef]

180. Arango-Díaz, A.; Moretti, E.; Talon, A.; Storaro, L.; Lenarda, M.; Núñez, P.; Marrero-Jerez, J.; Jiménez-Jiménez, J.; Jiménez-López, A.; Rodríguez-Castellón, E. Preferential CO oxidation (CO-PROX) catalyzed by CuO supported on nanocrystalline CeO$_2$ prepared by a freeze-drying method. *Appl. Catal. A Gen.* **2014**, *477*, 54–63. [CrossRef]

181. Teng, Y.; Sakurai, H.; Ueda, A.; Kobayashi, T. Oxidative removal of CO contained in hydrogen by using metal oxide catalysts. *Int. J. Hydrog. Energy* **1999**, *24*, 355–358. [CrossRef]

182. Zhao, Z.; Yung, M.M.; Ozkan, U.S. Effect of support on the preferential oxidation of CO over cobalt catalysts. *Catal. Commun.* **2008**, *9*, 1465–1471. [CrossRef]

183. Woods, M.P.; Gawade, P.; Tan, B.; Ozkan, U.S. Preferential oxidation of carbon monoxide on Co/CeO$_2$ nanoparticles. *Appl. Catal. B Environ.* **2010**, *97*, 28–35. [CrossRef]

184. Gawade, P.; Bayram, B.; Alexander, A.-M.C.; Ozkan, U.S. Preferential oxidation of CO (PROX) over CoO$_x$/CeO$_2$ in hydrogen-rich streams: Effect of cobalt loading. *Appl. Catal. B Environ.* **2012**, *128*, 21–30. [CrossRef]

185. Gorte, R.J.; Zhao, S. Studies of the water-gas-shift reaction with ceria-supported precious metals. *Catal. Today* **2005**, *104*, 18–24. [CrossRef]

186. Fu, Q.; Weber, A.; Flytzani-Stephanopoulos, M. Nanostructured Au-CeO$_2$ catalysts for low-temperature water-gas shift. *Catal. Lett.* **2001**, *77*, 87–95. [CrossRef]

187. Rodriguez, J.A.; Graciani, J.; Evans, J.; Park, J.B.; Yang, F.; Stacchiola, D.; Senanayake, S.D.; Ma, S.; Perez, M.; Liu, P.; et al. Water-gas shift reaction on a highly active inverse CeO$_x$ /Cu(111) catalyst: Unique role of ceria nanoparticles. *Angew. Chem. Int. Ed.* **2009**, *48*, 8047–8050. [CrossRef] [PubMed]

188. Barrio, L.; Estrella, M.; Zhou, G.; Wen, W.; Hanson, J.C.; Hungría, A.B.; Hornés, A.; Fernández-García, M.; Martínez-Arias, A.; Rodriguez, J.A. Unraveling the Active Site in Copper-Ceria Systems for the Water-Gas Shift Reaction: In Situ Characterization of an Inverse Powder CeO_{2-x}/CuO-Cu Catalyst. *J. Phys. Chem. C* **2010**, *114*, 3580–3587. [CrossRef]

189. Senanayake, S.D.; Stacchiola, D.; Evans, J.; Estrella, M.; Barrio, L.; Pérez, M.; Hrbek, J.; Rodriguez, J.A. Probing the reaction intermediates for the water-gas shift over inverse CeO_x /Au(111) catalysts. *J. Catal.* **2010**, *271*, 392–400. [CrossRef]

190. Stanmore, B.R.; Brilhac, J.F.; Gilot, P. The oxidation of soot: A review of experiments, mechanisms and models. *Carbon* **2001**, *39*, 2247–2268. [CrossRef]

191. Van Setten, B.A.; Makkee, M.; Moulijn, J.A. Science and technology of catalytic diesel particulate filters. *Catal. Rev.* **2001**, *43*, 489–564. [CrossRef]

192. Bueno-López, A. Diesel soot combustion ceria catalysts. *Appl. Catal. B Environ.* **2014**, *146*, 1–11. [CrossRef]

193. Fino, D.; Specchia, V. Open issues in oxidative catalysis for diesel particulate abatement. *Powder Technol.* **2008**, *180*, 64–73. [CrossRef]

194. Darcy, P.; Da Costa, P.; Mellottée, H.; Trichard, J.-M.; Djéga-Mariadassou, G. Kinetics of catalyzed and non-catalyzed oxidation of soot from a diesel engine. *Catal. Today* **2007**, *119*, 252–256. [CrossRef]

195. Kim, G. Ceria-Promoted Three-Way Catalysts for Auto Exhaust Emission Control. *Ind. Eng. Chem. Prod. Res. Dev.* **1982**, *21*, 267–274. [CrossRef]

196. Yao, H.C.; Yao, Y.Y. Ceria in Automotive Exhaust Catalysts: I. Oxygen storage. *J. Catal.* **1984**, *86*, 254–265. [CrossRef]

197. Trovarelli, A.; De Leitenburg, C.; Boaro, M.; Dolcetti, G. The utilization of ceria in industrial catalysis. *Catal. Today* **1999**, *50*, 353–367. [CrossRef]

198. Aneggi, E.; De Leitenburg, C.; Trovarelli, A. Ceria-Based Formulations for Catalysis for Diesel Soot Combustion. In *Catalysis by Ceria and Related Materials*; Trovarelli, A., Fornasiero, P., Eds.; World Scientific: Singapore, 2013; pp. 565–621.

199. Harada, K.; Oishi, T.; Hamamoto, S.; Ishihara, T. Lattice Oxygen Activity in Pr- and La-Doped CeO_2 for Low-Temperature Soot Oxidation. *J. Phys. Chem. C* **2014**, *118*, 559–568. [CrossRef]

200. Pushkarev, V.V.; Kovalchuk, V.I.; Itri, J.L. Probing Defect Sites on the CeO_2 Surface with Dioxygen. *J. Phys. Chem. B* **2004**, *108*, 5341–5348. [CrossRef]

201. Saab, E.; Abi-Aad, E.; Bokova, M.N.; Zhilinskaya, E.A.; Aboukaı, A. EPR characterisation of carbon black in loose and tight contact with Al_2O_3 and CeO_2 catalysts. *Carbon* **2007**, *45*, 561–567. [CrossRef]

202. Preda, G.; Migani, A.; Neyman, K.M.; Bromley, S.T.; Illas, F.; Pacchioni, G.; Milano, I. Formation of Superoxide Anions on Ceria Nanoparticles by Interaction of Molecular Oxygen with Ce^{3+} Sites. *J. Phys. Chem. C* **2011**, *115*, 5817–5822. [CrossRef]

203. Machida, M.; Murata, Y.; Kishikawa, K.; Zhang, D.; Ikeue, K. On the Reasons for High Activity of CeO_2 Catalyst for Soot Oxidation. *Chem. Mater.* **2008**, *20*, 4489–4494. [CrossRef]

204. Gross, M.S.; Ulla, M.A.; Querini, C.A. Diesel particulate matter combustion with CeO_2 as catalyst. Part I: System characterization and reaction mechanism. *J. Mol. Catal. A Chem.* **2012**, *352*, 86–94. [CrossRef]

205. Holgado, J.P.; Munuera, G.; Espinos, J.P.; González-Elipe, A.R. XPS study of oxidation processes of CeO_x defective layers. *Appl. Surf. Sci.* **2000**, *158*, 164–171. [CrossRef]

206. Behrens, M.; Studt, F.; Kasatkin, I.; Kühl, S.; Hävecker, M.; Abild-Pedersen, F.; Zander, S.; Girgsdies, F.; Kurr, P.; Kniep, B.-L.; et al. The Active Site of Methanol Synthesis over $Cu/ZnO/Al_2O_3$ Industrial Catalysts. *Science* **2012**, *336*, 893–897. [CrossRef]

207. Yang, Y.; Evans, J.; Rodriguez, J.A.; White, M.G.; Liu, P. Fundamental studies of methanol synthesis from CO_2 hydrogenation on Cu(111), Cu clusters, and Cu/ZnO(000). *Phys. Chem. Chem. Phys.* **2010**, *12*, 9909–9917. [CrossRef]

208. Rasmussen, P.B.; Kazuta, M.; Chorkendorff, I. Synthesis of methanol from a mixture of H_2 and CO_2 on Cu(100). *Surf. Sci.* **1994**, *318*, 267–280. [CrossRef]

209. Yoshihara, J.; Campbell, C.T. Methanol Synthesis and Reverse Water-Gas Shift Kinetics over Cu(110) Model Catalysts: Structural Sensitivity. *J. Catal.* **1996**, *161*, 776–782. [CrossRef]

210. Yang, Y.; White, M.G.; Liu, P. Theoretical Study of Methanol Synthesis from CO_2 Hydrogenation on Metal-Doped Cu(111) Surfaces. *J. Phys. Chem. C* **2012**, *116*, 248–256. [CrossRef]

211. Kondratenko, E.V.; Mul, G.; Baltrusaitis, J.; Larrazábal, G.O.; Pérez-Ramírez, J. Status and perspectives of CO_2 conversion into fuels and chemicals by catalytic, photocatalytic and electrocatalytic processes. *Energy Environ. Sci.* **2013**, *6*, 3112–3135. [CrossRef]

212. Quadrelli, E.A.; Centi, G.; Duplan, J.-L.; Perathoner, S. Carbon Dioxide Recycling: Emerging Large-Scale Technologies with Industrial Potential. *ChemSusChem* **2011**, *4*, 1194–1215. [CrossRef] [PubMed]

213. Preti, D.; Resta, C.; Squarcialupi, S.; Fachinetti, G. Carbon Dioxide Hydrogenation to Formic Acid by Using a Heterogeneous Gold Catalyst. *Angew. Chem. Int. Ed.* **2011**, *50*, 12551–12554. [CrossRef]

214. Ansari, M.B.; Min, B.-H.; Mo, Y.-H.; Park, S.-E. CO_2 activation and promotional effect in the oxidation of cyclic olefins over mesoporous carbon nitrides. *Green Chem.* **2011**, *13*, 1416–1421. [CrossRef]

215. Vidal, A.B.; Feria, L.; Evans, J.; Takahashi, Y.; Liu, P.; Nakamura, K.; Illas, F.; Rodriguez, J.A. CO_2 Activation and Methanol Synthesis on Novel Au/TiC and Cu/TiC Catalysts. *J. Phys. Chem. Lett.* **2012**, *3*, 2275–2280. [CrossRef]

216. Miguel, C.V.; Soria, M.A.; Mendes, A.; Madeira, L.M. Direct CO_2 hydrogenation to methane or methanol from post-combustion exhaust streams—A thermodynamic study. *J. Nat. Gas. Sci. Eng.* **2015**, *22*, 1–8. [CrossRef]

217. Torrente-Murciano, L.; Mattia, D.; Jones, M.D.; Plucinski, P.K. Formation of hydrocarbons via CO_2 hydrogenation—A thermodynamic study. *J. CO2 Util.* **2014**, *6*, 34–39. [CrossRef]

218. Medford, A.J.; Lausche, A.C.; Abild-Pedersen, F.; Temel, B.; Schjødt, N.C.; Nørskov, J.K.; Studt, F. Activity and Selectivity Trends in Synthesis Gas Conversion to Higher Alcohols. *Top. Catal.* **2014**, *57*, 135–142. [CrossRef]

219. Studt, F.; Behrens, M.; Kunkes, E.L.; Thomas, N.; Zander, S.; Tarasov, A.; Schumann, J.; Frei, E.; Varley, J.B.; Abild-Pedersen, F.; et al. The Mechanism of CO and CO_2 Hydrogenation to Methanol over Cu-Based Catalysts. *ChemCatChem* **2015**, *7*, 1105–1111. [CrossRef]

220. Lunkenbein, T.; Schumann, J.; Behrens, M.; Schlögl, R.; Willinger, M.G. Formation of a ZnO Overlayer in Industrial Cu/ZnO/Al$_2$O$_3$ Catalysts Induced by Strong Metal–Support Interactions. *Angew. Chem. Int. Ed.* **2015**, *54*, 4544–4548. [CrossRef] [PubMed]

221. Slaa, J.C.; Van Ommen, J.G.; Ross, J.R.H. The synthesis of higher alcohols using modified Cu/ZnO/Al$_2$O$_3$ catalysts. *Catal. Today* **1992**, *15*, 129–148. [CrossRef]

222. Nakamura, J.; Nakamura, I.; Uchijima, T.; Kanai, Y.; Watanabe, T.; Saito, M.; Fujitani, T. A Surface Science Investigation of Methanol Synthesis over a Zn-Deposited Polycrystalline Cu Surface. *J. Catal.* **1996**, *160*, 65–75. [CrossRef]

223. Schumann, J.; Eichelbaum, M.; Lunkenbein, T.; Thomas, N.; Álvarez Galván, M.C.; Schlögl, R.; Behrens, M. Promoting Strong Metal Support Interaction: Doping ZnO for Enhanced Activity of Cu/ZnO:M (M = Al, Ga, Mg) Catalysts. *ACS Catal.* **2015**, *5*, 3260–3270. [CrossRef]

224. Kandemir, T.; Kasatkin, I.; Girgsdies, F.; Zander, S.; Kühl, S.; Tovar, M.; Schlögl, R.; Behrens, M. Microstructural and Defect Analysis of Metal Nanoparticles in Functional Catalysts by Diffraction and Electron Microscopy: The Cu/ZnO Catalyst for Methanol Synthesis. *Top. Catal.* **2014**, *57*, 188–206. [CrossRef]

225. Rostrup-Nielsen, J.R. New aspects of syngas production and use. *Catal. Today* **2000**, *63*, 159–164. [CrossRef]

226. Reyes, S.C.; Sinfelt, J.H.; Feeley, J.S. Evolution of Processes for Synthesis Gas Production: Recent Developments in an Old Technology. *Ind. Eng. Chem. Res.* **2003**, *42*, 1588–1597. [CrossRef]

227. Liander, H. The utilisation of natural gases for the ammonia process. *Trans. Faraday Soc.* **1929**, *25*, 462. [CrossRef]

228. Goetsch, D.A.; Schmidt, L.D. Microsecond Catalytic Partial Oxidation of Alkanes. *Science* **1996**, *271*, 1560–1562. [CrossRef]

229. Tsang, S.C.; Claridge, J.B.; Green, M.L. Recent advances in the conversion of methane to synthesis gas. *Catal. Today* **1995**, *23*, 3–15. [CrossRef]

230. York, A.P.E.; Xiao, T.; Green, M.L.H. Brief overview of the partial oxidation of methane to synthesis gas. *Top. Catal.* **2003**, *22*, 345–358. [CrossRef]

231. Wilson, J.N.; Pedigo, R.A.; Zaera, F. Kinetics and Mechanism of Catalytic Partial Oxidation Reactions of Alkanes on Rhodium Surfaces. *J. Am. Chem. Soc.* **2008**, *130*, 15796–15797. [CrossRef]

232. Christian Enger, B.; Lødeng, R.; Holmen, A. A review of catalytic partial oxidation of methane to synthesis gas with emphasis on reaction mechanisms over transition metal catalysts. *Appl. Catal. A Gen.* **2008**, *346*, 1–27. [CrossRef]

233. Basile, F.; Benito, P.; Fornasari, G.; Monti, M.; Scavetta, E.; Tonelli, D.; Vaccari, A. Novel Rh-based structured catalysts for the catalytic partial oxidation of methane. *Catal. Today* **2010**, *157*, 183–190. [CrossRef]

234. Ashcroft, A.T.; Cheetham, A.K.; Foord, J.S.; Green, M.L.H.; Grey, C.P.; Murrell, A.J.; Vernon, P.D.F. Selective oxidation of methane to synthesis gas using transition metal catalysts. *Nature* **1990**, *344*, 319–321. [CrossRef]

235. Hargreaves, J.S.J.; Hutchings, G.J.; Joyner, R.W. Control of product selectivity in the partial oxidation of methane. *Nature* **1990**, *348*, 428–429. [CrossRef]

236. Hickman, D.A.; Schmidt, L.D. Production of Syngas by Direct Catalytic Oxidation of Methane. *Science* **1993**, *259*, 343–346. [CrossRef]

237. Pino, L.; Recupero, V.; Beninati, S.; Shukla, A.K.; Hegde, M.S.; Bera, P. Catalytic partial-oxidation of methane on a ceria-supported platinum catalyst for application in fuel cell electric vehicles. *Appl. Catal. A Gen.* **2002**, *225*, 63–75. [CrossRef]

238. Tang, W.; Hu, Z.; Wang, M.; Stucky, G.D.; Metiu, H.; McFarland, E.W. Methane complete and partial oxidation catalyzed by Pt-doped CeO_2. *J. Catal.* **2010**, *273*, 125–137. [CrossRef]

239. Gélin, P.; Primet, M. Complete oxidation of methane at low temperature over noble metal based catalysts: A review. *Appl. Catal. B Environ.* **2002**, *39*, 1–37. [CrossRef]

240. Honkanen, M.; Kärkkäinen, M.; Viitanen, V.; Jiang, H.; Kallinen, K.; Huuhtanen, M.; Vippola, M.; Lahtinen, J.; Keiski, R.; Lepistö, T. Structural Characteristics of Natural-Gas-Vehicle-Aged Oxidation Catalyst. *Top. Catal.* **2013**, *56*, 576–585. [CrossRef]

241. Choudhary, T.V.; Banerjee, S.; Choudhary, V.R. Catalysts for combustion of methane and lower alkanes. *Appl. Catal. A Gen.* **2002**, *234*, 1–23. [CrossRef]

242. Chen, J.; Arandiyan, H.; Gao, X.; Li, J. Recent Advances in Catalysts for Methane Combustion. *Catal. Surv. Asia* **2015**, *19*, 140–171. [CrossRef]

243. Farrauto, R.J. Low-Temperature Oxidation of Methane. *Science* **2012**, *337*, 659–660. [CrossRef]

244. Sekizawa, K.; Widjaja, H.; Maeda, S.; Ozawa, Y.; Eguchi, K. Low temperature oxidation of methane over Pd catalyst supported on metal oxides. *Catal. Today* **2000**, *59*, 69–74. [CrossRef]

245. Datye, A.K.; Bravo, J.; Nelson, T.R.; Atanasova, P.; Lyubovsky, M.; Pfefferle, L. Catalyst microstructure and methane oxidation reactivity during the Pd↔PdO transformation on alumina supports. *Appl. Catal. A Gen.* **2000**, *198*, 179–196. [CrossRef]

246. Chin, Y.-H.; Buda, C.; Neurock, M.; Iglesia, E. Consequences of Metal-Oxide Interconversion for C-H Bond Activation during CH_4 Reactions on Pd Catalysts. *J. Am. Chem. Soc.* **2013**, *135*, 15425–15442. [CrossRef]

247. Ramírez-López, R.; Elizalde-Martinez, I.; Balderas-Tapia, L. Complete catalytic oxidation of methane over Pd/CeO_2–Al_2O_3: The influence of different ceria loading. *Catal. Today* **2010**, *150*, 358–362. [CrossRef]

248. Tippayawong, N.; Thanompongchart, P. Biogas quality upgrade by simultaneous removal of CO_2 and H_2S in a packed column reactor. *Energy* **2010**, *35*, 4531–4535. [CrossRef]

249. Lavoie, J.M. Review on dry reforming of methane, a potentially more environmentally-friendly approach to the increasing natural gas exploitation. *Front. Chem.* **2014**, *2*, 1–17. [CrossRef]

250. Ghorbanzadeh, A.M.; Norouzi, S.; Mohammadi, T. High energy efficiency in syngas and hydrocarbon production from dissociation of CH_4-CO_2 mixture in a non-equilibrium pulsed plasma. *J. Phys. D. Appl. Phys.* **2005**, *38*, 3804–3811. [CrossRef]

251. Dry, M.E.; Steynberg, A.P. Chapter 5—Commercial FT Process Applications. In *Fischer-Tropsch Technology*; Steynberg, A., Dry, M., Eds.; Studies in Surface Science and Catalysis; Elsevier: Amsterdam, The Netherlands, 2004; pp. 406–481.

252. Wang, S.; Lu, G.Q.; Millar, G.J. Carbon dioxide reforming of methane to produce synthesis gas over metal-supported catalysts: State of the art. *Energy Fuels* **1996**, *10*, 896–904. [CrossRef]

253. Bradford, M.C.J.; Vannice, M.A. CO_2 reforming of CH_4. *Catal. Rev. Sci. Eng.* **1999**, *41*, 1–42. [CrossRef]

254. Rodhe, H. A Comparison of the Contribution of Various Gases to the Greenhouse Effect. *Science* **1990**, *248*, 1217–1219. [CrossRef]

255. Huang, A.; Xia, G.; Wang, J.; Suib, S.L.; Hayashi, Y.; Matsumoto, H. CO_2 Reforming of CH_4 by Atmospheric Pressure ac Discharge Plasmas. *J. Catal.* **2000**, *189*, 349–359. [CrossRef]

256. Wei, J.; Iglesia, E. Mechanism and Site Requirements for Activation and Chemical Conversion of Methane on Supported Pt Clusters and Turnover Rate Comparisons among Noble Metals. *J. Phys. Chem. B* **2004**, *108*, 4094–4103. [CrossRef]

257. Rostrupnielsen, J.R.; Hansen, J.H.B. CO_2-Reforming of Methane over Transition Metals. *J. Catal.* **1993**, *144*, 38–49. [CrossRef]

258. Hou, Z.; Chen, P.; Fang, H.; Zheng, X.; Yashima, T. Production of synthesis gas via methane reforming with CO_2 on noble metals and small amount of noble-(Rh-) promoted Ni catalysts. *Int. J. Hydrog. Energy* **2006**, *31*, 555–561. [CrossRef]

259. Pakhare, D.; Spivey, J. A review of dry (CO_2) reforming of methane over noble metal catalysts. *Chem. Soc. Rev.* **2014**, *43*, 7813–7837. [CrossRef] [PubMed]

260. Bradford, M.C.J.; Vannice, M.A. Catalytic reforming of methane with carbon dioxide over nickel catalysts I. Catalyst characterization and activity. *Appl. Catal. A Gen.* **1996**, *142*, 73–96. [CrossRef]

261. Budiman, A.W.; Song, S.-H.; Chang, T.-S.; Shin, C.-H.; Choi, M.-J. Dry Reforming of Methane Over Cobalt Catalysts: A Literature Review of Catalyst Development. *Catal. Surv. Asia* **2012**, *16*, 183–197. [CrossRef]

262. Kim, D.K.; Stöwe, K.; Müller, F.; Maier, W.F. Mechanistic study of the unusual catalytic properties of a new NiCe mixed oxide for the CO_2 reforming of methane. *J. Catal.* **2007**, *247*, 101–111. [CrossRef]

263. Wei, J.; Iglesia, E. Reaction Pathways and Site Requirements for the Activation and Chemical Conversion of Methane on Ru−Based Catalysts. *J. Phys. Chem. B* **2004**, *108*, 7253–7262. [CrossRef]

264. Mimura, N.; Takahara, I.; Inaba, M.; Okamoto, M.; Murata, K. High-performance Cr/H-ZSM-5 catalysts for oxidative dehydrogenation of ethane to ethylene with CO_2 as an oxidant. *Catal. Commun.* **2002**, *3*, 257–262. [CrossRef]

265. Porosoff, M.D.; Myint, M.N.Z.; Kattel, S.; Xie, Z.; Gomez, E.; Liu, P.; Chen, J.G. Identifying Different Types of Catalysts for CO_2 Reduction by Ethane through Dry Reforming and Oxidative Dehydrogenation. *Angew. Chem. Int. Ed.* **2015**, *54*, 15501–15505. [CrossRef]

266. Huber, G.W.; Iborra, S.; Corma, A. Synthesis of Transportation Fuels from Biomass: Chemistry, Catalysts, and Engineering. *Chem. Rev.* **2006**, *106*, 4044–4098. [CrossRef]

267. Mattos, L.V.; Jacobs, G.; Davis, B.H.; Noronha, F.B. Production of Hydrogen from Ethanol: Review of Reaction Mechanism and Catalyst Deactivation. *Chem. Rev.* **2012**, *112*, 4094–4123. [CrossRef]

268. Banach, B.; Machocki, A.; Rybak, P.; Denis, A.; Grzegorczyk, W.; Gac, W. Selective production of hydrogen by steam reforming of bio-ethanol. *Catal. Today* **2011**, *176*, 28–35. [CrossRef]

269. Breen, J.P.; Burch, R.; Coleman, H.M. Metal-catalysed steam reforming of ethanol in the production of hydrogen for fuel cell applications. *Appl. Catal. B Environ.* **2002**, *39*, 65–74. [CrossRef]

270. Liguras, D.K.; Kondarides, D.I.; Verykios, X.E. Production of hydrogen for fuel cells by steam reforming of ethanol over supported noble metal catalysts. *Appl. Catal. B Environ.* **2003**, *43*, 345–354. [CrossRef]

271. Frusteri, F.; Freni, S.; Spadaro, L.; Chiodo, V.; Bonura, G.; Donato, S.; Cavallaro, S. H_2 production for MC fuel cell by steam reforming of ethanol over MgO supported Pd, Rh, Ni and Co catalysts. *Catal. Commun.* **2004**, *5*, 611–615. [CrossRef]

272. Ni, M.; Leung, D.Y.C.; Leung, M.K.H. A review on reforming bio-ethanol for hydrogen production. *Int. J. Hydrog. Energy* **2007**, *32*, 3238–3247. [CrossRef]

273. Scott, M.; Goeffroy, M.; Chiu, W.; Blackford, M.A.; Idriss, H. Hydrogen Production from Ethanol over Rh-Pd/CeO_2 Catalysts. *Top. Catal.* **2008**, *51*, 13–21. [CrossRef]

274. Contreras, J.L.; Salmones, J.; Colín-Luna, J.A.; Nuño, L.; Quintana, B.; Córdova, I.; Zeifert, B.; Tapia, C.; Fuentes, G.A. Catalysts for H_2 production using the ethanol steam reforming (a review). *Int. J. Hydrog. Energy* **2014**, *39*, 18835–18853. [CrossRef]

275. Mariño, F.J.; Cerrella, E.G.; Duhalde, S.; Jobbagy, M.; Laborde, M.A. Hydrogen from steam reforming of ethanol. characterization and performance of copper-nickel supported catalysts. *Int. J. Hydrog. Energy* **1998**, *23*, 1095–1101. [CrossRef]

276. Llorca, J.; Homs, N.; Sales, J.; De la Piscina, P.R. Efficient Production of Hydrogen over Supported Cobalt Catalysts from Ethanol Steam Reforming. *J. Catal.* **2002**, *209*, 306–317. [CrossRef]

277. Zhang, B.; Tang, X.; Li, Y.; Cai, W.; Xu, Y.; Shen, W. Steam reforming of bio-ethanol for the production of hydrogen over ceria-supported Co, Ir and Ni catalysts. *Catal. Commun.* **2006**, *7*, 367–372. [CrossRef]

278. Denis, A.; Grzegorczyk, W.; Gac, W.; Machocki, A. Steam reforming of ethanol over Ni/support catalysts for generation of hydrogen for fuel cell applications. *Catal. Today* **2008**, *137*, 453–459. [CrossRef]

279. Bayram, B.; Soykal, I.I.; Von Deak, D.; Miller, J.T.; Ozkan, U.S. Ethanol steam reforming over Co-based catalysts: Investigation of cobalt coordination environment under reaction conditions. *J. Catal.* **2011**, *284*, 77–89. [CrossRef]

280. Dan, M.; Mihet, M.; Tasnadi-Asztalos, Z.; Imre-Lucaci, A.; Katona, G.; Lazar, M.D. Hydrogen production by ethanol steam reforming on nickel catalysts: Effect of support modification by CeO_2 and La_2O_3. *Fuel* **2015**, *147*, 260–268. [CrossRef]

281. Laosiripojana, N.; Assabumrungrat, S. Catalytic steam reforming of ethanol over high surface area CeO_2: The role of CeO_2 as an internal pre-reforming catalyst. *Appl. Catal. B Environ.* **2006**, *66*, 29–39. [CrossRef]

282. Lin, S.S.-Y.; Kim, D.H.; Ha, S.Y. Metallic phases of cobalt-based catalysts in ethanol steam reforming: The effect of cerium oxide. *Appl. Catal. A Gen.* **2009**, *355*, 69–77. [CrossRef]

283. Virginie, M.; Araque, M.; Roger, A.-C.; Vargas, J.C.; Kiennemann, A. Comparative study of H_2 production by ethanol steam reforming on $Ce_2Zr_{1.5}Co_{0.5}O_{8-\delta}$ and $Ce_2Zr_{1.5}Co_{0.47}Rh_{0.07}O_{8-\delta}$: Evidence of the Rh role on the deactivation process. *Catal. Today* **2008**, *138*, 21–27. [CrossRef]

284. Llorca, J.; Ramírez de la Piscina, P.; Dalmon, J.-A.; Homs, N. Transformation of Co_3O_4 during Ethanol Steam-Re-forming. Activation Process for Hydrogen Production. *Chem. Mater.* **2004**, *16*, 3573–3578. [CrossRef]

285. Raskó, J.; Dömök, M.; Baán, K.; Erdőhelyi, A. FTIR and mass spectrometric study of the interaction of ethanol and ethanol–water with oxide-supported platinum catalysts. *Appl. Catal. A Gen.* **2006**, *299*, 202–211. [CrossRef]

286. Palo, D.R.; Dagle, R.A.; Holladay, J.D. Methanol Steam Reforming for Hydrogen Production. *Chem. Rev.* **2007**, *107*, 3992–4021. [CrossRef]

287. Peppley, B.A.; Amphlett, J.C.; Kearns, L.M.; Mann, R.F. Methanol–steam reforming on $Cu/ZnO/Al_2O_3$. Part 1: The reaction network. *Appl. Catal. A Gen.* **1999**, *179*, 21–29. [CrossRef]

288. Lee, J.K.; Ko, J.B.; Kim, D.H. Methanol steam reforming over $Cu/ZnO/Al_2O_3$ catalyst: Kinetics and effectiveness factor. *Appl. Catal. A Gen.* **2004**, *278*, 25–35. [CrossRef]

289. Shishido, T.; Yamamoto, Y.; Morioka, H.; Takaki, K.; Takehira, K. Active Cu/ZnO and $Cu/ZnO/Al_2O_3$ catalysts prepared by homogeneous precipitation method in steam reforming of methanol. *Appl. Catal. A Gen.* **2004**, *263*, 249–253. [CrossRef]

290. Laosiripojana, N.; Assabumrungrat, S. Catalytic steam reforming of methane, methanol, and ethanol over Ni/YSZ: The possible use of these fuels in internal reforming SOFC. *J. Power Sources* **2007**, *163*, 943–951. [CrossRef]

291. Lu, J.; Li, X.; He, S.; Han, C.; Wan, G.; Lei, Y.; Chen, R.; Liu, P.; Chen, K.; Zhang, L.; et al. Hydrogen production via methanol steam reforming over Ni-based catalysts: Influences of Lanthanum (La) addition and supports. *Int. J. Hydrog. Energy* **2017**, *42*, 3647–3657. [CrossRef]

292. Tatibouët, J.M. Methanol oxidation as a catalytic surface probe. *Appl. Catal. A Gen.* **1997**, *148*, 213–252. [CrossRef]

293. Vilé, G.; Bridier, B.; Wichert, J.; Pérez-Ramírez, J. Ceria in Hydrogenation Catalysis: High Selectivity in the Conversion of Alkynes to Olefins. *Angew. Chem. Int. Ed.* **2012**, *51*, 8620–8623. [CrossRef] [PubMed]

294. Vilé, G.; Colussi, S.; Krumeich, F.; Trovarelli, A.; Pérez-Ramírez, J. Opposite Face Sensitivity of CeO_2 in Hydrogenation and Oxidation Catalysis. *Angew. Chem. Int. Ed.* **2014**, *53*, 12069–12072. [CrossRef]

295. Sohlberg, K.; Pantelides, S.T.; Pennycook, S.J. Interactions of Hydrogen with CeO_2. *J. Am. Chem. Soc.* **2001**, *123*, 6609–6611. [CrossRef]

296. Watkins, M.B.; Foster, A.S.; Shluger, A.L. Hydrogen Cycle on CeO_2 (111) Surfaces: Density Functional Theory Calculations. *J. Phys. Chem. C* **2007**, *111*, 15337–15341. [CrossRef]

297. Brisse, A.; Schefold, J.; Zahid, M. High temperature water electrolysis in solid oxide cells. *Int. J. Hydrog. Energy* **2008**, *33*, 5375–5382. [CrossRef]

298. Laguna-Bercero, M.A. Recent advances in high temperature electrolysis using solid oxide fuel cells: A review. *J. Power Sources* **2012**, *203*, 4–16. [CrossRef]

299. El Gabaly, F.; Grass, M.; McDaniel, A.H.; Farrow, R.L.; Linne, M.A.; Hussain, Z.; Bluhm, H.; Liu, Z.; McCarty, K.F. Measuring individual overpotentials in an operating solid-oxide electrochemical cell. *Phys. Chem. Chem. Phys.* **2010**, *12*, 12138–12145. [CrossRef] [PubMed]

300. DeCaluwe, S.C.; Grass, M.E.; Zhang, C.; Gabaly, F.E.; Bluhm, H.; Liu, Z.; Jackson, G.S.; McDaniel, A.H.; McCarty, K.F.; Farrow, R.L.; et al. In situ characterization of ceria oxidation states in high-temperature electrochemical cells with ambient pressure XPS. *J. Phys. Chem. C* **2010**, *114*, 19853–19861. [CrossRef]

301. Crumlin, E.J.; Bluhm, H.; Liu, Z. In situ investigation of electrochemical devices using ambient pressure photoelectron spectroscopy. *J. Electron. Spectros. Relat. Phenom.* **2013**, *190*, 84–92. [CrossRef]

302. Stoerzinger, K.A.; Hong, W.T.; Crumlin, E.J.; Bluhm, H.; Shao-Horn, Y. Insights into Electrochemical Reactions from Ambient Pressure Photoelectron Spectroscopy. *Acc. Chem. Res.* **2015**, *48*, 2976–2983. [CrossRef] [PubMed]

303. Yu, Y.; Mao, B.; Geller, A.; Chang, R.; Gaskell, K.; Eichhorn, B.W. CO$_2$ activation and carbonate intermediates: An operando AP-XPS study of CO$_2$ electrolysis reactions on solid oxide electrochemical cells. *Phys. Chem. Chem. Phys.* **2014**, *16*, 11633–11639. [CrossRef]

304. Jacobson, A.J. Materials for solid oxide fuel cells. *Chem. Mater.* **2010**, *22*, 660–674. [CrossRef]

305. Orera, A.; Slater, P.R. New chemical systems for solid oxide fuel cells. *Chem. Mater.* **2010**, *22*, 675–690. [CrossRef]

306. Rafique, M.; Nawaz, H.; Rafique, M.S.; Tahir, M.B.; Nabi, G.; Khalid, N.R. Material and method selection for efficient solid oxide fuel cell anode: Recent advancements and reviews. *Int. J. Energy Res.* **2019**, *43*, 2423–2446. [CrossRef]

307. Haile, S.M. Fuel cell materials and components. *Acta Mater.* **2003**, *51*, 5981–6000. [CrossRef]

308. Kharton, V.V.; Figueiredo, F.M.; Navarro, L.; Naumovich, E.N.; Kovalevsky, A.V.; Yaremchenko, A.A.; Viskup, A.P.; Carneiro, A.; Marques, F.M.B.; Frade, J.R. Ceria-based materials for solid oxide fuel cells. *J. Mater. Sci.* **2001**, *36*, 1105–1117. [CrossRef]

309. Zhang, C.; Grass, M.E.; McDaniel, A.H.; Decaluwe, S.C.; El Gabaly, F.; Liu, Z.; McCarty, K.F.; Farrow, R.L.; Linne, M.A.; Hussain, Z.; et al. Measuring fundamental properties in operating solid oxide electrochemical cells by using in situ X-ray photoelectron spectroscopy. *Nat. Mater.* **2010**, *9*, 944–949. [CrossRef] [PubMed]

310. Zhang, C.; Grass, M.E.; Yu, Y.; Gaskell, K.J.; Decaluwe, S.C.; Chang, R.; Jackson, G.S.; Hussain, Z.; Bluhm, H.; Eichhorn, B.W.; et al. Multielement activity mapping and potential mapping in solid oxide electrochemical cells through the use of operando XPS. *ACS Catal.* **2012**, *2*, 2297–2304. [CrossRef]

311. Chueh, W.C.; Mcdaniel, A.H.; Grass, M.E.; Hao, Y.; Jabeen, N.; Liu, Z.; Haile, S.M.; Mccarty, K.F.; Bluhm, H.; El Gabaly, F. Highly Enhanced Concentration and Stability of Reactive Ce^{3+} on Doped CeO$_2$ Surface Revealed In Operando. *Chem. Mater.* **2012**, *24*, 1876–1882. [CrossRef]

312. Zhang, C.; Yu, Y.; Grass, M.E.; Dejoie, C.; Ding, W.; Gaskell, K.; Jabeen, N.; Hong, Y.P.; Shavorskiy, A.; Bluhm, H.; et al. Mechanistic studies of water electrolysis and hydrogen electro-oxidation on high temperature ceria-based solid oxide electrochemical cells. *J. Am. Chem. Soc.* **2013**, *135*, 11572–11579. [CrossRef]

313. Gopal, C.B.; El Gabaly, F.; McDaniel, A.H.; Chueh, W.C. Origin and Tunability of Unusually Large Surface Capacitance in Doped Cerium Oxide Studied by Ambient-Pressure X-Ray Photoelectron Spectroscopy. *Adv. Mater.* **2016**, *28*, 4692–4697. [CrossRef]

314. Papaefthimiou, V.; Niakolas, D.K.; Paloukis, F.; Dintzer, T.; Zafeiratos, S. Is Steam an Oxidant or a Reductant for Nickel/Doped-Ceria Cermets? *ChemPhysChem* **2017**, *18*, 164–170. [CrossRef]

315. Papaefthimiou, V.; Niakolas, D.K.; Paloukis, F.; Teschner, D.; Knop-Gericke, A.; Haevecker, M.; Zafeiratos, S. Operando observation of nickel/ceria electrode surfaces during intermediate temperature steam electrolysis. *J. Catal.* **2017**, *352*, 305–313. [CrossRef]

316. Nurk, G.; Kooser, K.; Urpelainen, S.; Käämbre, T.; Joost, U.; Kodu, M.; Kivi, I.; Kanarbik, R.; Kukk, E.; Lust, E. Near ambient pressure X-ray photoelectron-and impedance spectroscopy study of NiO-Ce$_{0.9}$Gd$_{0.1}$O$_{2-\Delta}$ anode reduction using a novel dual-chamber spectroelectrochemical cell. *J. Power Sources* **2018**, *378*, 589–596. [CrossRef]

317. Wang, L.; Jackson, G.S. Evaluating the behavior of CO/CO$_2$ in Ni/GDC solid oxide fuel cell anodes. *ECS Trans.* **2015**, *68*, 1193–1205. [CrossRef]

318. Papaefthimiou, V.; Shishkin, M.; Niakolas, D.K.; Athanasiou, M.; Law, Y.T.; Arrigo, R.; Teschner, D.; Hävecker, M.; Knop-Gericke, A.; Schlögl, R.; et al. On the active surface state of nickel-ceria solid oxide fuel cell anodes during methane electrooxidation. *Adv. Energy Mater.* **2013**, *3*, 762–769. [CrossRef]

319. Graves, C.; Ebbesen, S.D.; Mogensen, M.; Lackner, K.S. Sustainable hydrocarbon fuels by recycling CO$_2$ and H$_2$O with renewable or nuclear energy. *Renew. Sustain. Energy Rev.* **2011**, *15*, 1–23. [CrossRef]

320. Sridhar, K.R.; Vaniman, B.T. Oxygen production on Mars using solid oxide electrolysis. *Solid State Ion.* **1997**, *93*, 321–328. [CrossRef]